IGNITION OF HYDROCARBON FUELS BY A REPETITIVELY PULSED NANOSECOND PULSE DURATION PLASMA

DISSERTATION

Presented in Partial Fulfillment of the Requirements for

the Degree Doctor of Philosophy in the

Graduate School of The Ohio State University

By

Ainan Bao, M.S.

* * * * *

The Ohio State University

2008

Dissertation Committee:

Dr. Igor V. Adamovich, Adviser

Dr. Ahmet Selamet

Dr. J. William Rich

Dr. Walter R. Lempert

Approved by:

_____

Adviser

Graduate Program in Mechanical Engineering

ABSTRACT

The dissertation presents experimental and kinetic modeling studies of ignition of hydrocarbon-air flows by a high voltage, repetitively pulsed, nanosecond pulse duration plasma. This type of plasma offers two critical advantages. First, a high reduced electric field during the pulse results in efficient electronic excitation and molecular dissociation. Second, extremely low duty cycle of the repetitively pulsed nanosecond discharge greatly improves the plasma stability and helps sustain a diffuse and uniform nonequilibrium plasma.

Gaseous fuel ignition experiments using a Chemical Physics Technologies (CPT) pulser (16-18 kV peak voltage, 20-30 nsec pulse duration, up to 50 kHz pulse repetition rate) generating a plasma in premixed ethylene-air and methane-air flows demonstrated flow ignition occurring at low air plasma temperatures, 200-300^0 C. The experiments showed that adding fuel to the air flow increased the flow temperature in the plasma, up to 500-600^0 C. At these conditions, the reacted fuel fraction was up to 80%, and significant amounts of combustion products were detected. The experiments also showed significant fuel oxidation, with a resultant temperature rise, at conditions when there was no ignition detected. Replacing air with nitrogen at the same flow and plasma conditions resulted in much less plasma temperature rise. This demonstrates that the temperature

increase is due to plasma chemical fuel oxidation reactions, rather than due to excited species quenching. This suggests that low-temperature plasma chemical reactions can oxidize significant amounts of hydrocarbons and increase the temperature of the air-fuel mixture, prior to ignition. Ignition occurs when the flow temperature becomes close to autoignition temperature, due to an additional energy release in plasma chemical reactions. The present results also showed that plasma assisted ignition occurred at a low discharge power, ~1% of heat of combustion.

Experiments in hydrocarbon-air plasmas generated by an alternative, Fast Ionization Dynistor (FID) pulse generator (50 kV peak voltage, 5 nsec pulse duration, up to 100 kHz pulse repetition rate) did not result in ignition. It is concluded that a lower pulser energy coupled to the flow by the FID pulser resulted in less flow heating and presumably in lower radical concentrations generated in the plasma, thereby precluding ignition.

Ignition experiments in liquid methanol- and ethanol-air mixtures by the CPT pulser showed that preheating of the air flow up to 50-60^0 C is critical for producing ignition. Ignition was achieved, and significant plasma temperature rise and fuel oxidation were detected in preheated methanol-air and ethanol-air flows.

A kinetic model was developed to simulate plasma assisted ignition of hydrocarbon-air mixtures by a repetitively pulsed, nanosecond pulse duration, low-temperature plasma. The model was validated by comparing with O atom concentration measurements in single-pulse discharges in air, methane-air, and ethylene-air, showing good agreement. Kinetic modeling of a repetitively pulsed discharge at the present experimental conditions did not predict significant fuel oxidation or ignition at the

measured discharge power. The model predicts that ignition would occur only if the discharge power is 2.5 times higher than measured in the experiments. The difference between two hydrocarbon oxidation mechanisms predictions suggests that neither of them might be applicable at the low-temperature conditions (starting at room temperature) of the present experiments. This demonstrates the need for development and validation of a low-temperature hydrocarbon oxidation in non-equilibrium plasmas.

ACKNOWLEDGMENTS

First and foremost, I would like to thank my adviser, Dr. Igor V. Adamovich, for his generous support over the last four years and for his guidance and advising of my research work.

I express my sincere gratitude to Dr. J. William Rich and Dr. Walter R. Lempert for their numerous suggestions through this project.

I would like to thank my colleagues, V. Naveen Chintala, Munetake Nishihara, Saurabh Keshav, Adam Hicks, John Bruzzese, Yurii Utkin, and Guofeng Lou for their support and assistance with the experiments. I also thank all the students in Non-equilibrium Thermodynamics lab.

I would like to acknowledge the sponsorship of the U.S. Air Force Office of Scientific Research, and NASA – Glenn Research Center.

Finally, I thank my parents for their love and unconditional support over the years.

VITA

September 26, 1979 …….Born – Qinhuangdao, China.

June, 2001……..B.S. Engineering Thermophysics, Tsinghua University, China.

June, 2003……M.S. Engineering Thermophysics, Tsinghua University, China.

December, 2003–present…….……Graduate Research Associate, The Ohio State University.

PUBLICATIONS

1. A. Bao, Y. G. Utkin, S. Keshav, G. Lou, and I.V. Adamovich, "Ignition of Ethylene-Air and Methane-Air Flows by Low-Temperature Repetitively Pulsed Nanosecond Discharge Plasma", IEEE Transactions on Plasma Science, Vol. 35, No. 6, pp. 1628-1638, 2007
2. G. Lou, A. Bao, M. Nishihara, S. Keshav, Y. G. Utkin, J. W. Rich, W. R. Lempert, and I. V. Adamovich, "Ignition of Premixed Hydrocarbon-Air Flows by Repetitively Pulsed, Nanosecond Pulse Duration Plasma", Proceedings of the Combustion Institute, Vol.31, No.2, pp.3327-3334, 2007
3. N. Chintala, A. Bao, G. Lou, and I. V. Adamovich, "Measurements of Combustion Efficiency in Nonequilibrium RF Plasma Ignited Flows", Combustion and Flame, Vol.144, No.4, pp.744-756, 2006

FIELDS OF STUDY

Major Field: Mechanical Engineering

TABLE OF CONTENTS

LIST OF TABLES

LIST OF FIGURES

CHAPTER 1

INTRODUCTION

1. 1 Significance of the problem

Ignition and flame stabilization in combustible mixtures are among the most challenging problems in fundamental and applied combustion research [1]. Reduction of ignition delay time, flameholding and flame stability improvement, flame blow-off prevention, possibility of high-altitude relight, reduction of nitric oxide and hydrocarbon emissions from non-stoichiometric flames and extension of fuel flammability limits are some of the key technical issues in this field. In particular, control of ignition and combustion in aircraft jet engines would result in better performance and control of a variety of parameters, such as flight speed, altitude, and thrust [2]. Capability of a quick engine relight in case of a flameout at high altitudes and low combustor pressures is extremely desirable. Another critical issue is combustion stabilization at fuel lean conditions, which would help reduce NO_x emissions from the engine. An ignition method applicable for low combustor pressures, high flow velocities, and low equivalence ratios may help resolve these issues.

In supersonic combustors, depending on the flow Mach number, flow residence time in the combustor may be comparable with the chemical reaction time. This is an

especially important issue for hydrocarbon fuels because of their long ignition delay time. For example, ignition delay time in a stoichiometric ethylene-air flow at P=1 atm varies from 30 msec to 20 μsec in a temperature range from 1000 to 1500 K (see Fig. 1.1 [3]). This is comparable with the M=2-3 (u~1000 m/s) flow residence time in a combustor L~1m long, τ_{res}~L/u=1 msec. Several different solutions have been suggested to overcome this difficulty, such as passive cavity flame holders [4], energy addition to the flow [5], and adding self-igniting species, such as silane (SiH_4), to the air-fuel mixture [6]. Cavity flame holders provide a subsonic region for flame stabilization as well as for enhanced air-fuel mixing. However, they result in greater stagnation pressure loss in the combustor. Also, sometimes a flame stabilized by the cavity does not couple out to the supersonic flow, which results in incomplete combustion [4]. Energy addition to the flow also requires an additional combustion chamber [5].

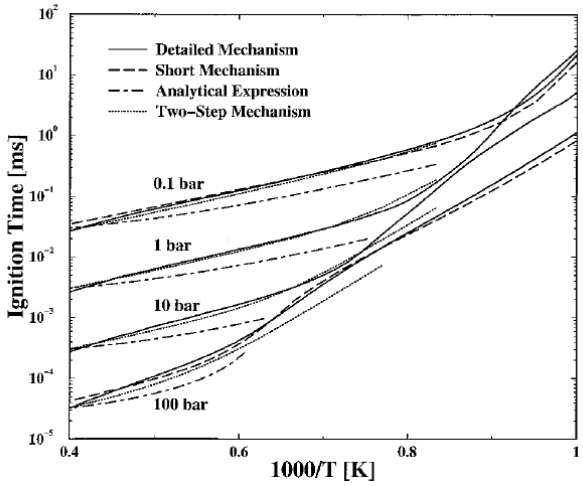

Figure 1.1: Calculated ignition delay time in a stoichiometric ethylene-air flow [3].

The use of a plasma may offer some advantages for ignition and flame stabilization. Apart from simply heating the air-fuel flow, nonequilibrium plasmas can be used to generate chemically active species, such as electronically excited molecules and

free radicals. The question whether active species generation is in fact the dominant effect in plasma assisted ignition is still being debated. Recent experimental results, reviewed in Section 1.3, suggest that nonequilibrium plasmas may produce large-volume ignition, reduce ignition delay time, improve flame stability, and expand flammability limits of combustible mixtures.

1.2 Ignition methods

Common approaches to ignition of combustible mixtures include the use of heated surfaces or filaments, pilot flames, electric discharges (spark or arc discharges and plasma torches), and high-power lasers.

The main disadvantage of the heated surface/filament method is long ignition delay time, controlled by a relatively slow rate of surface heating and slow heat transfer from a heated surface to the flow, and a short lifetime of the heated element. Ignition by a pilot flame requires maintaining the pilot at all times, and is vulnerable to pilot blow-off. Spark discharge is widely accepted as a straightforward and sufficiently reliable ignition method, especially in the automobile industry. However, spark ignition becomes less effective in high-speed flows and in low-pressure flows [7]. Laser ignition methods [8], which require the use of high–power, high-cost lasers and need optical access to the combustible mixture flow, are impractical. A common problem of all these traditional ignition methods is small ignition volume, which may result in misfire and incomplete combustion. This issue becomes especially critical in high-speed flows due to low lateral flame propagation speed, u~1 m/s [1], compared to the axial flow velocity.

In recent years, studies of ignition of combustible flows using large volume, low-temperature nonequilibrium plasmas have attracted considerable attention [9]. Various types of nonequilibrium plasmas have been used for combustion initiation and flame stabilization, such as (a) pulsed corona discharge, (b) microwave discharge, (c) RF discharge, (d) "gliding arc" discharge, (e) single pulse, nanosecond pulse duration Fast Ionization Wave (FIW) discharge, and (f) uniform, volume-filling, repetitively pulsed nanosecond discharge. The main idea of this approach is to use nonequilibrium, large-volume, low-temperature plasmas for either ignition or flame stabilization, using chemically active radical species generated in the plasma in dissociation and electronic excitation processes by electron impact. These ignition methods are reviewed in greater detail in the next section.

1.3 Brief overview of nonequilibrium plasma assisted combustion results

Ignition of non-flowing preheated hydrogen-air and hydrocarbon-air mixtures [10-12] by a single-pulse fast ionization wave (FIW) discharge was first studied by a group at the Moscow Institute of Physics and Technology (MIPT). A schematic of this experiment is shown in Fig. 1.2. A combustible mixture was preheated behind a reflected shock in a shock tube/discharge section, after which a propagating ionization wave pulse was sent along the discharge section. The results demonstrated that a high-voltage nanosecond discharge pulse substantially reduced ignition delay time, by up to an order of magnitude in C_xH_y-O_2-N_2-Ar and C_xH_y-O_2 -Ar mixtures, compared to autoignition delay time (e.g. see Fig. 1.3 [12]). Using a high voltage discharge pulse, these mixtures were ignited at significantly lower temperatures compared to autoignition temperatures

(as low as 900 K, see Fig. 1.3). Estimated discharge pulse energy coupled to the mixture showed that additional heating of the mixture by the pulse is relatively modest, only about 15 K, and cannot explain the observed ignition delay time reduction. However, in these experiments ignition by a FIW pulse could not be achieved below shock preheating temperatures of $T \leq 900$-1000 K. In particular, ignition delay time below $T \leq 1000$ K exceeded $\tau_{delay} \sim 1$ msec (see Fig. 1.3), which was comparable to the shock tube test time, i.e. the time before the rarefaction wave arrived into the shock tube test section. For this reason, feasibility of hydrocarbon fuel ignition by the FIW pulse at low preheating temperatures could not be tested.

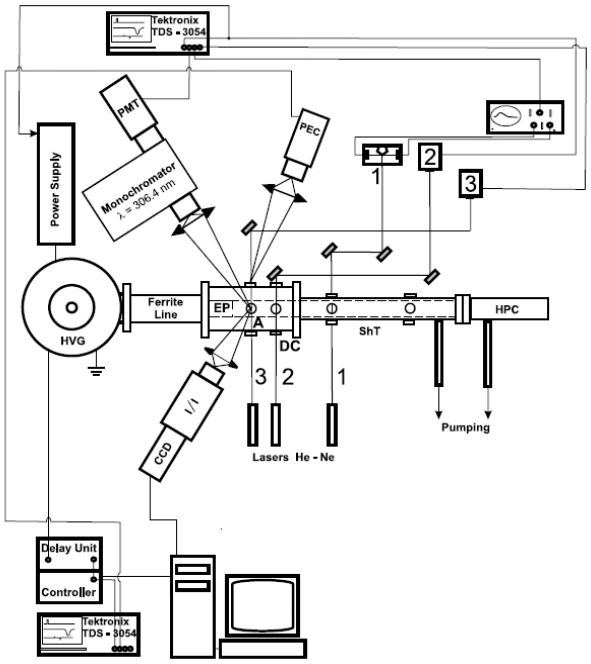

Figure 1.2: Schematic of the FIW experimental setup at MIPT [11]. A–optical access windows, DC–discharge cell, EP–end plate, HPC–high pressure cell, HVG–high voltage pulse generator, ShT–shock tube, PG–microsecond pulse generator, CCD–CCD camera, IR–intensifier, PD–photodiodes, PEC–photoelectric cell, PMT–photomultiplier.

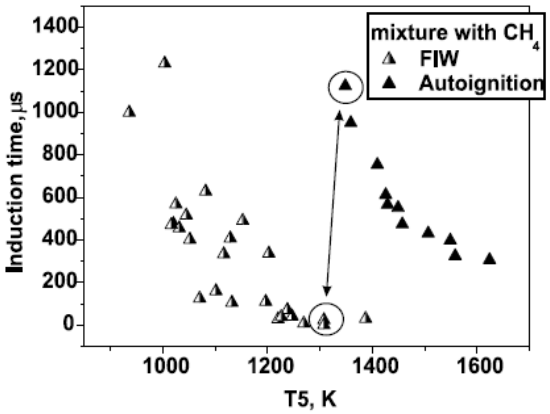

Figure 1.3: Ignition delay time vs. temperature in a CH_4-O_2-Ar mixture in the FIW experiments [12].

In a separate experiment at MIPT, a repetitively pulsed nanosecond discharge, at a pulse repetition rate of ν=1.2 kHz was used to stabilize a premixed atmospheric pressure propane-air flame, as shown schematically in Fig. 1.4 [13, 14]. The results showed that the plasma stabilized the flame and increased the flame blow-off velocity, in a wide range of equivalence ratios (see Fig. 1.5 [14]). As can be seen from Fig. 1.5, the effect of the plasma on the flame blow-off velocity is strongest at an equivalence ratio of Φ=0.65-0.75. At these conditions, the discharge power was less than 1% of the energy released during combustion. OH emission measurements showed that the plasma increased OH radical concentration both upstream of the flame and in the flame. This suggests that it is the OH generation by the plasma, rather than additional heating of the flow, that improved flame stability and increased the blow-off velocity.

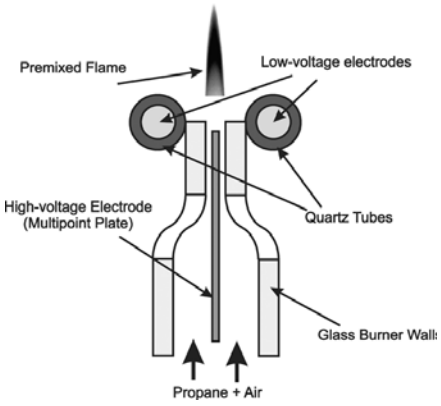

Figure 1.4: Schematic of the flame stabilization experiment by a repetitively pulsed nanosecond discharge [13].

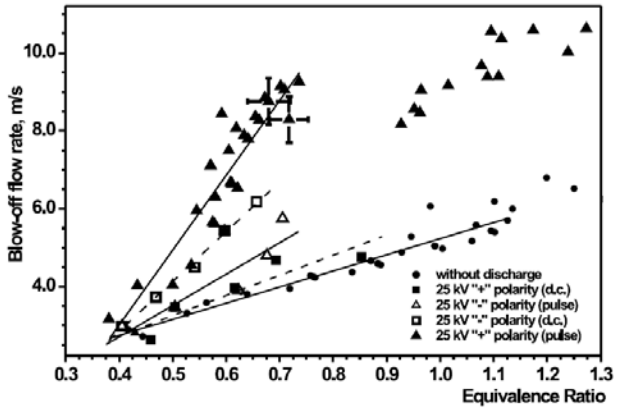

Figure 1.5: Flame blow-off velocities vs. equivalence ratio in the flame stabilization experiments [14].

Finally, a low-temperature hydrocarbon fuel oxidation experiment at MIPT showed that a repetitively pulsed FIW plasma can slowly oxidize hydrocarbon species without producing ignition [15, 16]. In this experiment, a uniform repetitively pulsed discharge (ν=40 Hz) was generated in non-flowing hydrocarbon-air mixtures at pressures ranging from P=1 to 12 torr. At these conditions, the fuel oxidation time, defined as the time over which the emission signal of CO ($B^1\Sigma \rightarrow A^1\Pi$) bands in the discharge differed from the steady-state value by 5%, was from a few ten to a few hundred seconds (see Fig.

1.6 [15]). This demonstrates that nearly complete hydrocarbon oxidation by the repetitively pulsed FIW discharge requires ~ 1,000- 10,000 pulses.

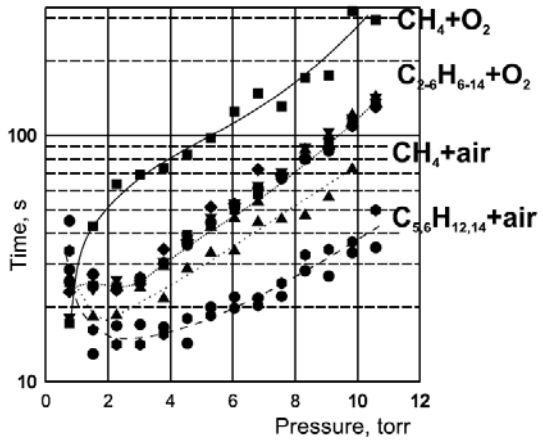

Figure 1.6: Hydrocarbon oxidation time in a repetitively pulsed nanosecond discharge at ν=40 kHz [15].

At Ecole Centrale, Paris, Laux et al [17, 18] used a nanosecond duration, repetitively pulsed plasma (peak voltage 10 kV, pulse duration 10 ns, pulse repetition rate 30 kHz) to stabilize a flame and improve combustion efficiency in a turbulent, lean, premixed propane-air flame at atmospheric pressure [17]. The results showed that the plasma significantly increases heat release and combustion efficiency, so that the flame can be stabilized under very lean conditions, where it would not exist without the plasma (see Fig. 1.7). In other words, in these experiments lean flammability limit has been significantly extended toward the lean mixtures. In a different experiment by Laux et al [18], a repetitively pulsed discharge in a point-to-plane geometry was used to ignite combustible mixtures in a non-flowing cell. They measured minimum discharge energy needed to achieve ignition (see Fig. 1.8). Unfortunately, no comparison was made between ignition efficiency of the nanosecond pulsed discharge and a spark discharge produced by a regular spark plug.

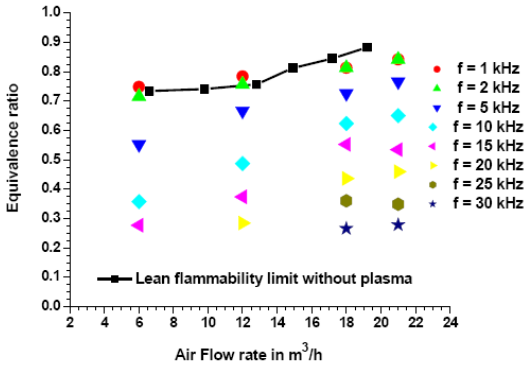

Figure 1.7: Critical equivalence ratio (lean flammability limit) as a function of the discharge pulse repetition rate [17].

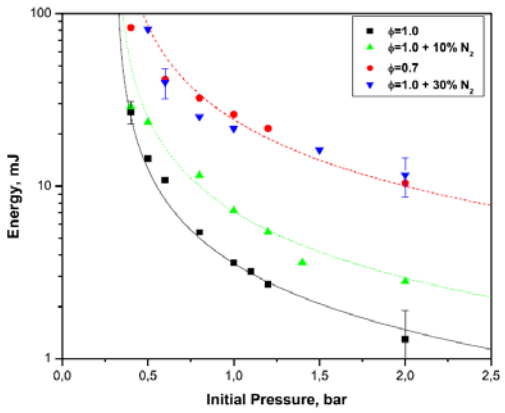

Figure 1.8: Minimum energy deposition into the plasma required to achieve ignition of various propane-air-nitrogen mixtures [18].

At Stanford University, Cappelli et al [19, 20] compared three different types of nonequilibrium plasmas used for flame stabilization in a lifted jet diffusion methane-air flame, a single electrode corona discharge (SECD), an asymmetric dielectric barrier discharge (DBD), and an ultra-short repetitively pulsed discharge (USRD, pulse duration of ~10 ns). Their results showed that the SECD discharge can stabilize the flame at a 20% higher co-flow speed than without the plasma, the DBD discharge increases the blow-off velocity by up to 50%, and the USRD discharge increases the blow-off velocity by nearly a factor of ten, as shown in Fig. 1.9.

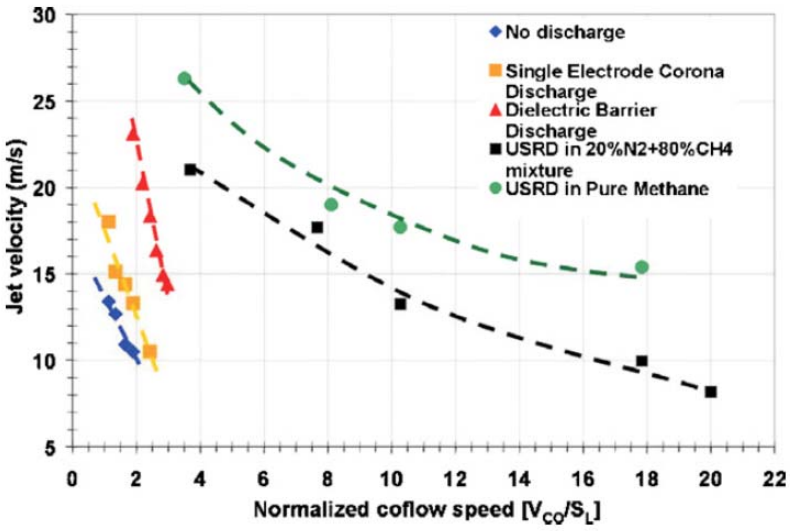

Figure 1.9: Effect of different types of discharge on the maximum co-flow speed (blow-off velocity) [19].

In experiments at the OSU Nonequilibrium Thermodynamics Laboratory [21, 22], a low-temperature transverse radiofrequency (RF) discharge plasma has been used to ignite methane-air, ethylene-air, and CO-air mixtures at low temperatures. The results showed that large-volume ignition by a uniform RF plasma could be achieved at significantly higher flow velocities (up to u=25 m/s) and lower pressures (P=60-130 torr), in a wide range of equivalence ratios, where conventional ignition methods, such as spark discharge or DC arc discharge, are ineffective. The experiments also demonstrated flame stabilization by the RF plasma, without using any physical obstacle flameholders. Temperature measurement results by infrared emission spectroscopy, using CO as a thermometric element, showed that the flow temperature in the air plasma before the fuel was added (T=250-300^0 C in ethylene-air flows and T=350-400^0 C in methane-air flows at P=60-120 torr, see Fig. 1.10) was considerably lower than autoignition temperature for ethylene-air mixtures at the same pressure (T_{auto}=600-700^0 C [23]). Fourier Transform

Infrared (FTIR) absorption spectra of combustion products showed that significant fractions of the fuel are burned in RF plasma-generated flames (up to 100% of ethylene-air and 70% of methane-air, see Fig. 1.11). The results also showed that significant amounts of fuel were oxidized in lean fuel-air mixtures, when there was no flame detected in the test section (see Fig. 1.11). Visible emission spectroscopy measurements in hydrocarbon-air flows in the RF discharge detected presence of radical species such as CN, CH, C_2, and OH, as well as O and H atoms. Finally, the results showed the plasma power budget to be a few per cent of the heat of combustion.

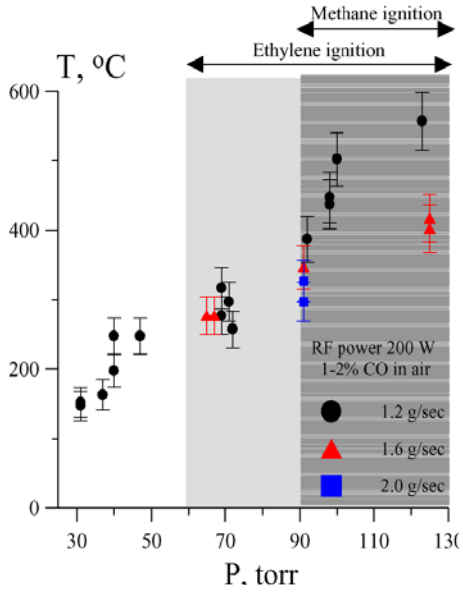

Figure 1.10: Flow temperatures in transverse RF discharge in air at different pressures and mass flow rates. RF power 200 W [21].

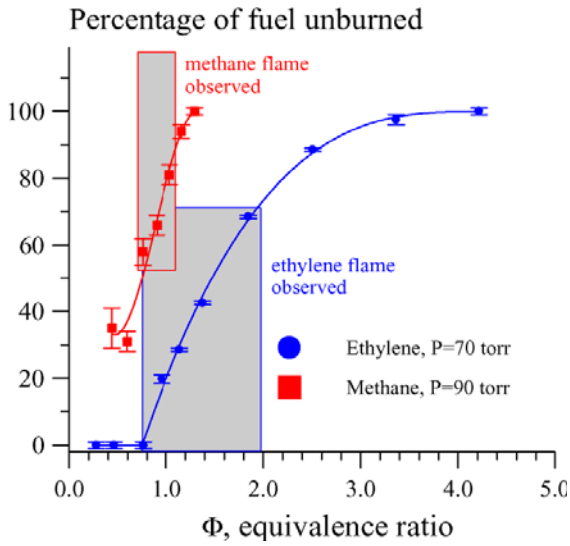

Figure 1.11: Percentage of fuel left unreacted in the flow in transverse RF discharge. Shaded areas indicate conditions at which a flame is detected in the test section [22].

At Princeton University, Ju et al [24, 25] used a non-equilibrium Magnetic Gliding Arc (MGC) discharge plasma for combustion enhancement in nitrogen diluted hydrocarbon-air and hydrogen-air counter-flow flames. The results showed that with the plasma sustained in the air flow, the extinction strain rate in methane-air flows significantly increases, up to 220 percent. This effect was achieved at a low discharge power, ≈78 W. The results suggested that the observed effect was predominantly thermal. However, the authors also hypothesized that excited species formed in the plasma may also contribute to the detected combustion enhancement.

Leonov et al [26,27] at the Institute of High Temperatures of the Russian Academy of Science (IVTAN) used a DC discharge sustained between separately ballasted pin electrodes in a cavity in a supersonic air flow to ignite hydrogen and ethylene injected into the flow in the cavity. The schematic of the experiment is shown in Fig. 1.12. The flow Mach number was M=2, the initial static pressure was varied from

0.2 to 0.8 bar, and the fuel injectors were installed on the bottom wall of the cavity (see Fig. 1.12). A filamentary DC discharge, with the input power of 1-10 kW, was used. The results show that ignition of hydrogen and ethylene occurs when the discharge power exceeds 1 kW. When the discharge power exceeded 3 kW and the equivalence ratio was greater than 1, the flame extended above the cavity (see Fig. 1.13), These experiments were conducted at fuel flow rates of up to 4 g/sec.

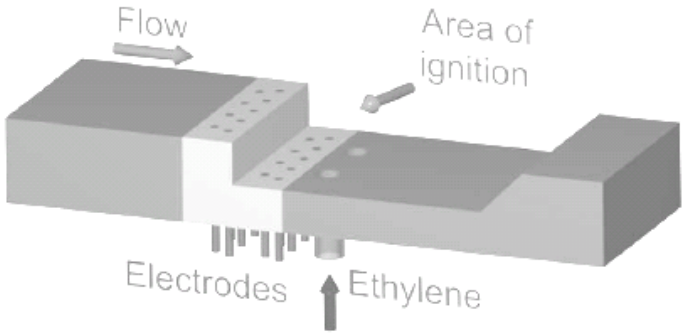

Figure 1.12: Schematic of the plasma-assisted combustion experiment in a supersonic flow [26].

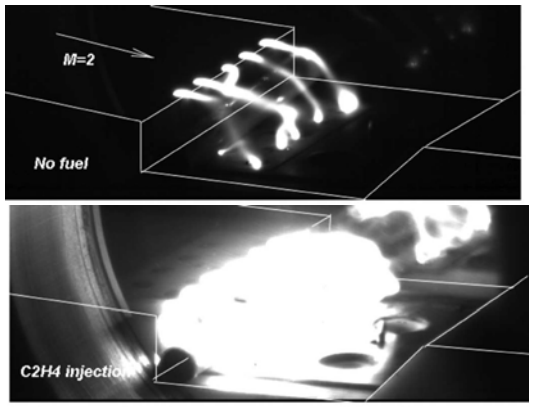

Figure 1.13: Photograph of the discharge in air (top) and of the discharge/flame region in ethylene-air (bottom) [27].

At the present moment, a significant amount of experimental results on nonequilibrium plasma assisted ignition and combustion has been accumulated. However, kinetics of plasma assisted ignition and combustion at low temperatures still remain not fully understood. This shows the necessity of a detailed experimental and kinetic modeling study of the use of nonequilibrium plasma for low-temperature ignition.

1.4 Objectives

For nonequilibrium plasma assisted ignition and combustion at low temperatures, the most critical issue is isolating possible non-thermal plasma effects on ignition kinetics (such as efficient radical generation by the plasma) from a "trivial" effect of localized flow heating in "hot spots" formed in the plasma, e.g. due to ionization instability development. Ionization instabilities are known to become much harder to control at high flow pressures and plasma volumes. At high pressures diffuse, volume-filling nonequilibrium plasmas typically collapse into constricted, high-temperature arc filaments [28]. For this reason, the ability to generate and sustain a uniform plasma at high pressures is extremely important for studies of plasma assisted ignition.

This dissertation presents experimental and kinetic modeling studies of plasma assisted ignition and combustion by using a high-voltage, short pulse duration, high pulse repetition rate discharge. This discharge offers two critical advantages compared with other types of nonequilibrium plasmas [29,30]:

1) It greatly improves plasma stability. In this type of discharge, the ionizing pulse duration (a few tens of nanoseconds) is much shorter than characteristic time for ionization instability development and glow-to-arc transition, ~10^{-3}-10^{-4} sec [28].

This makes possible stable operation of this discharge at much higher pressures and power loadings, compared to other types of nonequilibrium plasmas.

2) The reduced electric field, E/N, during the high voltage pulses results in efficient ionization, electronic excitation, and dissociation of molecular species by electron impact, the rates of which have strong exponential dependence on E/N [28]. This may result in generation of large amounts of active radical species at a relatively low plasma power budget compared to the heat of combustion.

The main objectives of the present work are

1) Experimentally study ignition of gaseous hydrocarbon fuels by a repetitively pulsed nanosecond discharge. Measure flow temperature in the discharge and product species concentrations at different mass flow rates and equivalence ratios. Determine whether ignition is thermal.

2) Experimentally study ignition of liquid fuels in the same type of discharge.

3) Develop a kinetic model of hydrocarbon fuel oxidation and ignition by a repetitively pulsed discharge. Validate the model and use it to elucidate a kinetic mechanism of fuel oxidation and ignition by a low-temperature plasma.

The structure of the present dissertation is as follows: Chapter 2 describes the experimental apparatus and diagnostics used. Chapter 3 discusses the results of the experiments. Chapter 4 describes a kinetic model of hydrocarbon oxidation and ignition in hydrocarbon-air plasmas of high-voltage nanosecond duration pulsed discharges. Chapter 5 presents the results of model validation and kinetic modeling calculations. Finally, Chapter 6 summarizes the results of the present work and presents conclusions.

CHAPTER 2

EXPERIMENTAL SETUP

2.1 Schematic of a high-speed plasma combustion facility

The schematic of the plasma assisted combustion facility is shown in Fig. 2.1. A premixed flow of air and hydrocarbon fuel (methane, ethylene, methanol, or ethanol) at different equivalence ratios and different mass flow rates enters a combustion test section from a gas supply system. In the present experiments, static pressure in the test section ranges from 70 torr to 100 torr, and is controlled by the vent valve of the vacuum system shown in Fig 2.1. The mass flow rate through the test section is varied from 0.8 g/s to 3 g/s. At these conditions, the flow velocity ranges from 10 to 50 m/s, and the equivalence ratio varies from 0.5 to 2.0. The test section pressure and the mass flow rate can be varied independently. This makes the experimental facility suitable for combustion studies both in high-speed, low-pressure and in low-speed, intermediate pressure flows.

Downstream of the test section, the flow is diluted with atmospheric air through the vent valve to adjust the pressure in the vacuum system and in the test section, and to prevent further combustion in the vacuum system and in the dump tank (see Fig. 2.1). The 1200 ft^3 spherical dump tank is pumped out using an Allis-Chalmers 1300 cfm rotary vane vacuum pump.

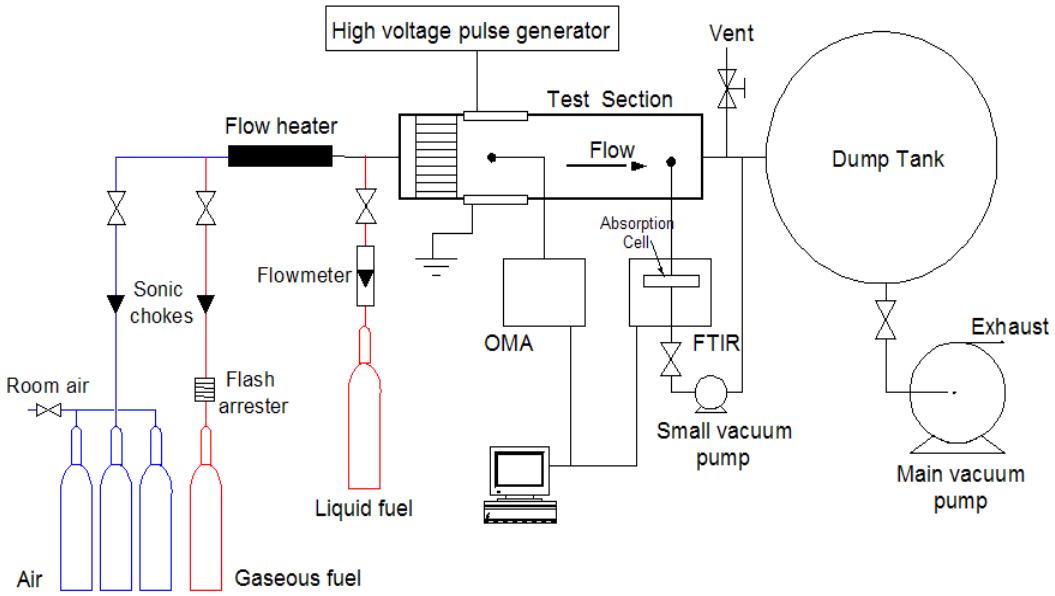

Figure 2.1: Schematic of the high-speed plasma combustion facility.

The facility operates using cylinder air and gaseous or liquid fuel. The diameters of the air and the gaseous fuel delivery lines are 1" and ¼", respectively. The air and the gaseous fuel mass flow rates are determined by measuring flow pressures upstream of the sonic choke plates (inserts with pinholes of known area) placed in the air and fuel delivery lines. When the flow through a pinhole is choked, which occurs when the pressure ratio across the choke plate exceeds $f(\gamma) = (1+(\gamma-1)/2)^{-\gamma/(\gamma-1)}$, $f(\gamma) = 0.528$ for air (γ=1.4) , the mass flow rate is [31]

$$\dot{m} = \frac{P_0 A^*}{\sqrt{T_0}} \sqrt{\frac{\gamma}{R}\left(\frac{2}{\gamma+1}\right)^{(\gamma+1)/(\gamma-1)}} \quad . \tag{2.1}$$

In Eq. (2.1), P_0 and T_0 are flow pressure and temperature upstream of the choke plate where the flow is near stagnation, A is the pinhole cross sectional area, γ is the specific heat ratio, and R is the gas constant at room temperature (γ=1.32 for methane and

γ=1.24 for ethylene [32]). The air and the gaseous fuel flows are mixed approximately 10 ft upstream of the test section. Additional air-fuel flow mixing is produced in an 18-inch-long in-line flow mixer located immediately upstream of the test section. Spring-loaded shutoff valve and a flash arrester installed in the 1/4" diameter gaseous fuel supply line enable quick flow shutoff and prevent flame propagation into the fuel cylinder.

As shown in Fig. 2.1, the flow through the test section can be preheated up to T=200^0 C using a 6 kW in-line flow heater (Big Chief Inc.). When the heater is in operation, the flow temperature in the test section (in the absence of the plasma) is measured by a thermocouple inserted into the flow through a port in the test section cover.

Downstream of the heater and approximately 30 cm upstream of the test section, liquid fuel (methanol or ethanol) can be injected into the air delivery line from an M1 fine atomizing spray nozzle (Danfoss Hago Inc.). The M1 nozzle is rated to produce 17 μm to 40 μm diameter fuel droplets into a full cone spray angle of 80^0 within the fuel flow rate range of 0.66 cm^3/sec to 2.35 cm^3/sec ($\dot{m}_{fuel}$=0.52-1.85 g/sec for ethanol and methanol). However, at the present conditions the mass flow rate of fuel was typically considerably lower, $\dot{m}_{fuel}$=0.1-0.2 g/sec, which adversely affected the droplet size and fuel spray pattern. The fuel is delivered from a 300 mL volume stainless steel bubbler pressurized by compressed air up to P=80 psi, as shown in Fig. 2.1. The flow rate of the fuel is monitored by an Omega FL-3751ST flow meter, calibrated by measuring the volume of liquid fuel delivered over an extended period of time (several minutes). Liquid fuel can be preheated by a tape heater wrapped around the 1/4" diameter copper liquid fuel

delivery line and powered by a variable voltage DC power supply. The fuel temperature is measured by a thermocouple placed between the copper tube and the tape heater.

Preheating of liquid fuel and air is necessary to accelerate the rate of fuel vaporization and to prevent excessive cooling of the air-fuel mixture during vaporization. For example, the equilibrium temperature of a stoichiometric air-ethanol vapor mixture (6.5% C_2H_5OH by volume) obtained by mixing of non-preheated (room temperature) air and liquid ethanol at adiabatic conditions is T=-60^0 C. Note that the temperature of the air-fuel vapor mixture needs to the sufficiently high to make sure that the fuel saturated vapor pressure is greater than the fuel partial pressure, to avoid fuel condensation in the test section. For example, methanol saturated vapor pressure at T=25^0 C is 59 torr, while methanol vapor partial pressure in a stoichiometric air-methanol mixture (12.2% CH_3OH by volume) at P=90 torr is 11 torr. This shows the necessity of fuel and air preheating. Typically, liquid fuel is preheated up to T=60^0 C, which is slightly below boiling point of ethanol (78.4^0 C) and methanol (64.7^0 C) at atmospheric pressure. Air flow is typically preheated up to T=60^0 C. No flow preheating has been used in the gaseous fuel ignition experiments.

2.2 Discharge/Combustion test section

The schematic of 5 cm x 1 cm rectangular cross section, 31 cm long test section, made of steel, is shown in Fig. 2.2. Figure 2.3 shows the test section drawing. The flow enters the test section through a 1/2″ long ceramic honeycomb flow straightener (300 holes per square inch), which also serves as an additional flashback arrester, and passes between two electrode blocks. Two 5 cm x 4 cm rectangular electrode blocks are

manufactured of macor ceramic and are flush mounted in the top and bottom test section walls. The copper electrode plates are placed into recesses machined in the electrode blocks, as shown in Fig. 2.2. The electrodes are rounded at the edges to prevent high electric field concentration and "hot spot" formation in the plasma near the edges. The electrodes are separated from the flow by 1/16″ thick macor ceramic plates. To prevent corona discharge formation in air pockets between the macor block, the copper electrodes, and the macor plates, this space is filled by a self-hardening dielectric compound (silicon rubber). The 2 mm diameter copper electrode leads are soldered to the electrode plates and insulated from the grounded test section by 10 mm outer diameter cylindrical sleeves made of macor ceramic. The space between the leads and the sleeves is also filled by the silicon rubber. Two macor ceramic inserts are also placed in the side walls of the test section, to prevent the discharge between the high voltage electrode and the grounded test section. Four stepped cylinder BK-7 glass windows are used to provide optical access to the discharge region through 10 mm diameter circular holes machined in the test section and in the side wall inserts. The main objective of this design was to confine the discharge plasma to the area between the ceramic plates on top and bottom and between the ceramic side wall inserts, without extending to the steel walls of the test section. Striking a discharge between the high voltage electrode and a test section wall would result in arc filament and hot spot formation in the plasma. Two additional rectangular windows, also made of BK-7 glass, are located approximately 1 cm downstream of the discharge region. Thermocouple port and static pressure / flow sampling port are located at the end of the test section, as shown in Fig. 2.2. In the present experiments, the flow downstream of the discharge section was sampled using the

static pressure / sample port shown in Fig. 2.2 by one of two approaches, (i) through the wall pressure tap, and (ii) through a 1/16” diameter steel tube extending halfway between the top and bottom walls. This was done to make sure that the flow is not sampled from the near-wall region.

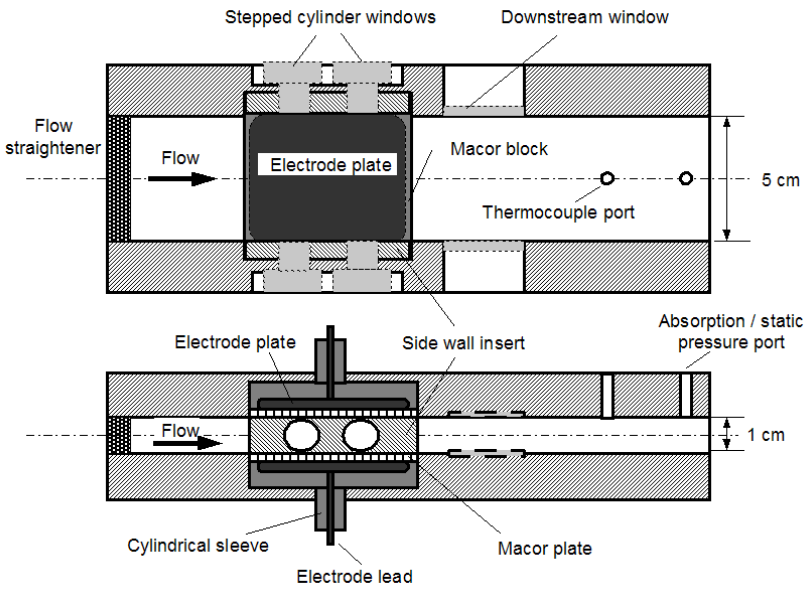

Figure 2.2: Schematic of the plasma assisted combustion test section (not to scale).

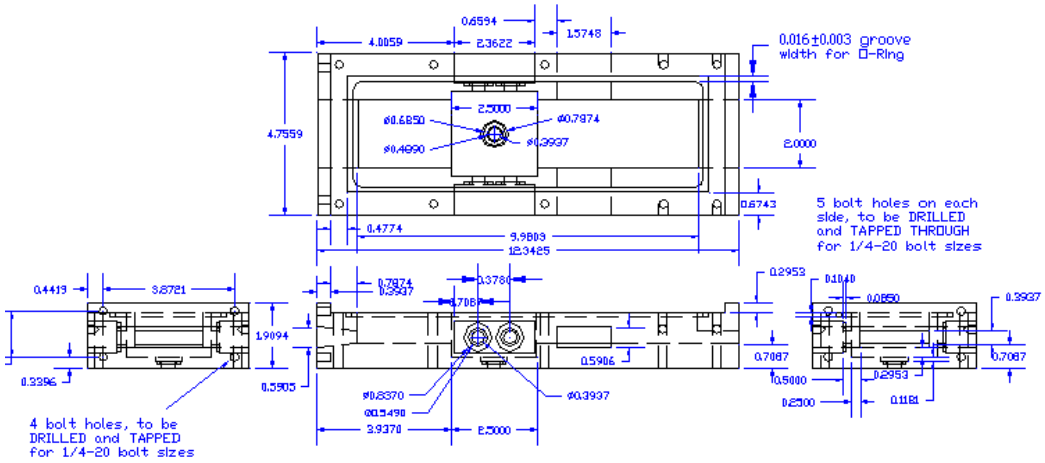

Figure 2.3: Drawing of the plasma assisted combustion test section (dimensions are in inches)

2.3 High voltage pulsed power supplies

The electrodes shown in Fig. 2.2 are connected to a high-voltage pulsed plasma generator. In the present experiments, two pulsed plasma generators have been used. One is the Chemical Physics Technologies (CPT) custom design high-voltage (up to 20-25 kV peak), short pulse duration (~20-30 nsec), high repetition rate (up to 50 kHz) pulsed plasma generator. The CPT pulser generates negative polarity pulses between a negative high voltage electrode and a grounded electrode. The CPT pulser has been designed in such a way that the impedance of the load was considered to be a part of the pulser electrical circuit. For this reason, the leads between the pulse generator and the load need to be as short as possible. In the present setup, the leads are ~15 cm long. Longer leads would result in changing the load impedance and distortion of the output pulse, and pulse energy reflection back into the plasma generator.

The other pulser is the Fast Ionization Dynistor (FID) Technology pulsed plasma generator, FID FPG 60-100MC4, which has four output channels, two positive and two negative. The output pulse amplitude on each channel is 8 kV. During the FID pulser operation, the signals from the four channels are transmitted to the load via four coaxial cables (75 Ω, 3 m long each). The two positive polarity cables are connected in series (i.e. the central wire of one cable is connected to the shielding of the other cable, as shown in Fig. 2.4). The two negative polarity cables are connected in the same way. Since in each cable the potential difference between the shielding and the central wire is 8 kV, the total amplitude of the output pulse for this type of connection (i.e. the potential difference between the central wire and the ground) is 16 kV (positive or negative). A stack of ferrite rings over the two double-voltage cables (see Fig. 2.4) prevents the

double-voltage pulse propagation back to the pulse generator. Therefore, the total voltage between the two double-voltage output cables is 32 kV. Note that if breakdown between the load electrodes does not occur, both the positive and the negative high voltage pulses are reflected back to the pulse generator. In this case, the voltage at the end of each cable connected to the load doubles again [33]. For this reason, the maximum voltage on the load electrodes is 64 kV. If breakdown does occur, the voltage between the electrodes will be lower, between 32 kV and 64 kV. In this type of connection, none of the load electrodes are grounded.

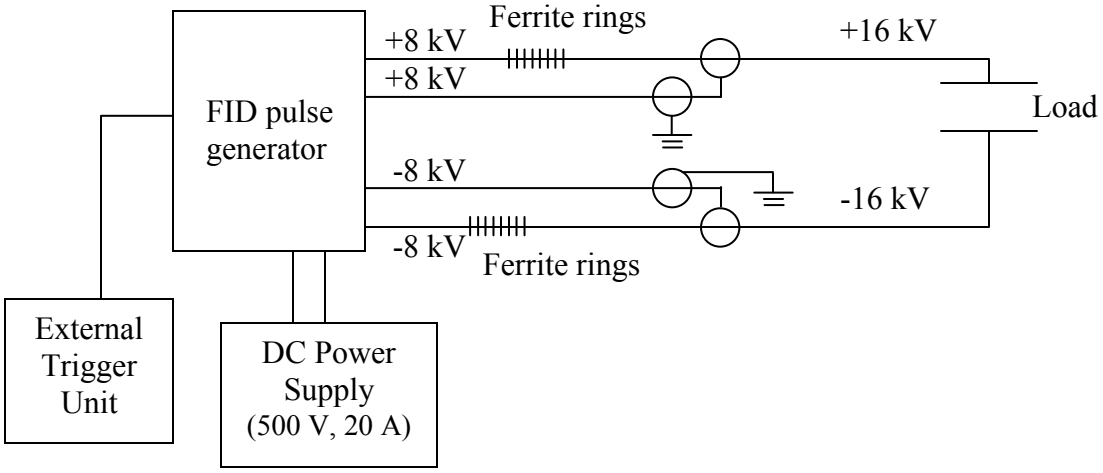

Figure 2.4: Schematic of the FID pulse generator output cable connection.

Pulse repetition rate of the FID pulser (from single pulse to 100 kHz) is controlled by an external trigger unit, which generates low-voltage TTL pulses (15 V peak, 200 nsec duration). The high-voltage output pulse duration is 5 nsec. The FID pulser can operate in both continuous and pulse burst modes (also controlled by the external trigger). The input

signal to the FID pulser is supplied by a low-voltage, high current DC power supply (500 V, 20 A, Magna-Power Electronics, as shown in Fig. 2.4.

During the CPT pulser operation, pulse voltage and current in the external circuit are measured using a Tektronix P6015A high voltage probe and a low-capacitance resistive current probe, as shown in Fig. 2.5 [34]. The Tektronix high voltage probe has also been used to measure pulse voltage during the FID pulser operation (for positive and negative pulses separately). In this case, the current probe could not be used, since this would require grounding one of the load electrodes (see Fig. 2.5). Note that the use of the Tektronix high voltage probe to measure the FID generator pulse shape is somewhat questionable, since the bandwidth of the probe is only 75 MHz (time resolution of ~ 10 nsec). However, comparison of the high voltage probe measurements with other experimental techniques providing better time resolution demonstrated that the high-voltage probe does not significantly distort 5 nsec duration pulses (see Chapter 3). Therefore, in the present work, the Tektronix high voltage probe has also been used to measure the FID voltage pulse shape.

The current and voltage waveforms have been analyzed by a Tektronix oscilloscope (TDS 3032B). For the CPT pulser, the pulse energy coupled to the load has been measured by integrating the voltage and the current waveforms, $Q = \int_{-\infty}^{+\infty} U(t)I(t)dt$ (see Chapter 3). To prevent overheating of the electrode blocks, the run time of the pulse generators was limited to two seconds.

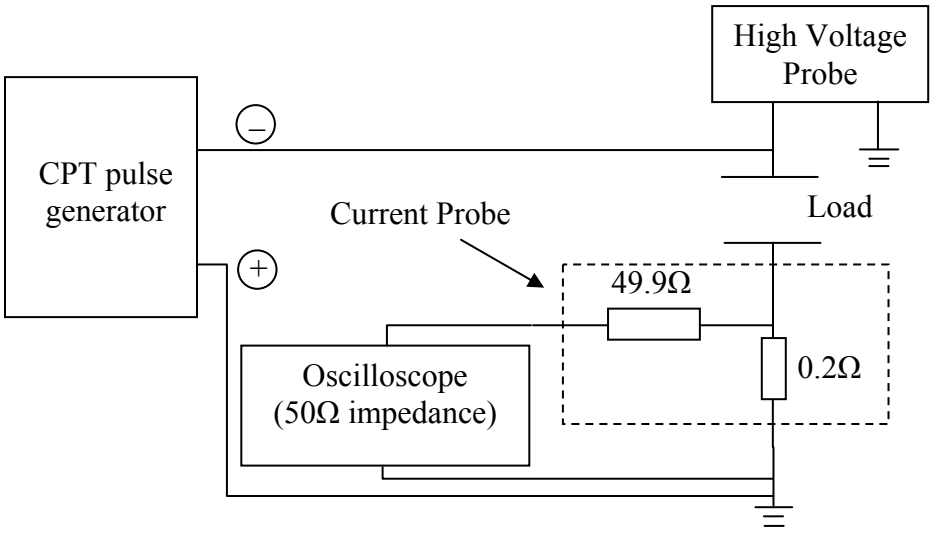

Figure 2.5: Schematic of voltage and current measurements

2.4 Visible emission spectroscopy setup

For the time-averaged visible emission spectroscopy measurements, we used an Optical Multichannel Analyzer (OMA) with a CCD array camera and a Spectra Physics 0.5 m monochromator with a 1200 g/mm grating. The SpectraPro-500i monochromator includes a triple grating turret, an imaging optical system, built-in RS232 and IEEE488 interfaces, and a micrometer controlled entrance slit. In the present measurements, we have used a 1200 grooves/mm grating, blazed at 500 nm. Two different cameras, both made by Princeton Instruments, have been used in the present experiments. Both cameras use thermoelectric cooling of the CCD detector. The first camera is an intensified PI-Max 512 camera (ICCD), with a 512x512 pixel CCD array. The other camera is a PIXIS 256E camera with a 1024x256 pixel CCD array. The latter camera has higher signal to noise and a higher spectral resolution, 0.05 nm vs. 0.25 nm for the first camera (FWHM of a 404.656 nm line of Hg at the entrance slit width of 0.02 mm).

Two plane-convex 300 mm focal length, 2" diameter lenses, made of BK-7 glass, are used to focus the emission signal from the test section onto the monochromator slit. In particular, one of the lenses is positioned at a distance of 300 mm from the center of the test section, in alignment with the center line of the downstream circular window, shown in Fig. 2.2. After the first lens, the emission light is reflected by three plane gold coated mirrors and focused onto the monochromator slit by the second lens.

Visible emission spectra of the plasma (partially rotationally resolved 0→2 band of the $N_2(C^3\Pi_u \rightarrow B^3\Pi_g)$ band system, at 375 nm) have been used to infer the flow rotational temperature. For this, synthetic spectrum has been used, with accurate nitrogen molecular constants, rotational line intensities, and the experimentally measured slit function of the spectrometer. Detailed description of the nitrogen second positive system synthetic spectrum code is given in Appendix A. The slit function of the spectrometer was determined from a Hg-Ar lamp atomic emission line shape, measured for two Hg lines, 365.015 nm and 404.656 nm. Typically, the monochromator slit width was 0.02 to 0.1 mm.

Time-resolved visible emission from the flow in the test section has been measured using an Acton Research Vacuum UV spectrometer (Model VM 504) equipped with a photo-multiplier tube (PMT), with spectral resolution of up to 0.1 nm. Time-resolved emission signals from the repetitively pulsed plasma was taken through the downstream circular stepped window (see Fig. 2.2), while emission signal of the flame was taken through the rectangular window downstream of the discharge region, as shown in Fig. 2.2.

2.5 FTIR absorption spectroscopy setup

Fourier Transform Infrared (FTIR) absorption spectra of combustible mixtures and of combustion products, with and without plasma, are taken with a Biorad 175C dynamic alignment FTIR spectrometer with a liquid nitrogen cooled InSb detector. For this, the flow was sampled through the static pressure / flow sampling port at the downstream end of the test section (see Fig. 2.2) into a 17.5 cm long cylindrical glass absorption cell with two CaF_2 windows placed into an absorption compartment of the FT spectrometer. Before sampling the flow, the absorption cell and the supply lines were evacuated using a small vacuum pump. The flow in the test section was sampled by manually opening a spring loaded valve in the line connecting the test section and the absorption cell, for approximately 0.5 sec. The absorption spectra were measured at a resolution of 0.5 cm^{-1} using an internal source (globar) of the FT spectrometer. Note that although the flow temperature in the presence of the plasma and the flame in the test section may be quite high, the flow sample in the absorption cell quickly cools off. Therefore the absorption spectra with and without plasma are compared at the same (room) temperature. This was verified by thermocouple temperature measurements in the absorption cell.

CHAPTER 3

EXPERIMENTAL RESULTS

3.1 Ignition of gaseous hydrocarbon fuels by a repetitively pulsed discharge (CPT pulse generator)

3.1.1 High voltage pulse characterization

Figure 3.1(a) shows typical single pulse voltage and current signals produced by the CPT pulse generator connected to the two test section electrodes shown in Fig 2.1, in quiescent air at P= 1atm. Figure 3.1(b) shows the time-dependent product of voltage and current at these conditions, i.e. instantaneous power. When the power is positive, the power is transmitted from the pulse generator to the load, and when the power is negative, it is reflected back to the pulse generator. For the raw current and voltage data shown in Fig. 3.1(a), the time integral of the instantaneous power (i.e. the pulser energy coupled to the load) is 3.9 mJ. However, at these conditions (P=1atm, single pulse), no breakdown occurs in the test section and no corona discharges are formed where the pulse generator leads are connected to the electrodes. Therefore, the actual pulse energy should be zero. We believe that the non-zero pulse energy obtained from the raw data of Fig. 3.1(a) is due to the phase shift between the current and the voltage signals, e.g. due

to the length difference in the cables connecting the high voltage probe and the current probe with the oscilloscope. To account for this phase shift, the current waveform was shifted relative to the voltage waveform until the calculated pulse energy became zero. This occurred for the phase shift of 1.4 nsec. Figure 3.2(a) and (b) show the current and voltage waveforms, as well as the instantaneous power signal with this phase shift incorporated.

Figure 3.3(a) shows current and voltage waveforms measured at the actual experimental conditions (air, P=70 torr, $\dot{m}$ =0.8 g/sec), with the same phase shift as measured in quiescent air at P=1 atm, 1.4 nsec. As can be seen, pulse peak voltage and current are approximately 18 kV and 50 A, respectively, with the voltage pulse width at half maximum of approximately 30 nsec. At the baseline conditions, i.e. at the test section pressure and temperature of P=70 torr and T=300 K, the estimated peak reduced electric field in the plasma generated by the pulse is $E/N \sim 70 \cdot 10^{-16}$ V·cm^2. Note that this upper bound estimate does not take into account the voltage fall across the plasma sheaths and the ceramic plates covering the electrodes. Figure 3.3(b) shows instantaneous power at these conditions. Integration of the power waveforms gives the net pulse energy coupled to the discharge of 2.2 mJ, with the forward power of 7.2 mJ and the reflected power of 5.0 mJ. Figure 3.4 shows current and voltage waveforms in air (a) and in a stoichiometric ethylene-air mixture (b) at P=70 torr and $\dot{m}$ =1.2 g/sec. It can be seen that the waveforms in air and fuel/air flow look very similar. Pulse energies measured at these conditions are also very close, 2.03 mJ and 2.00 mJ.

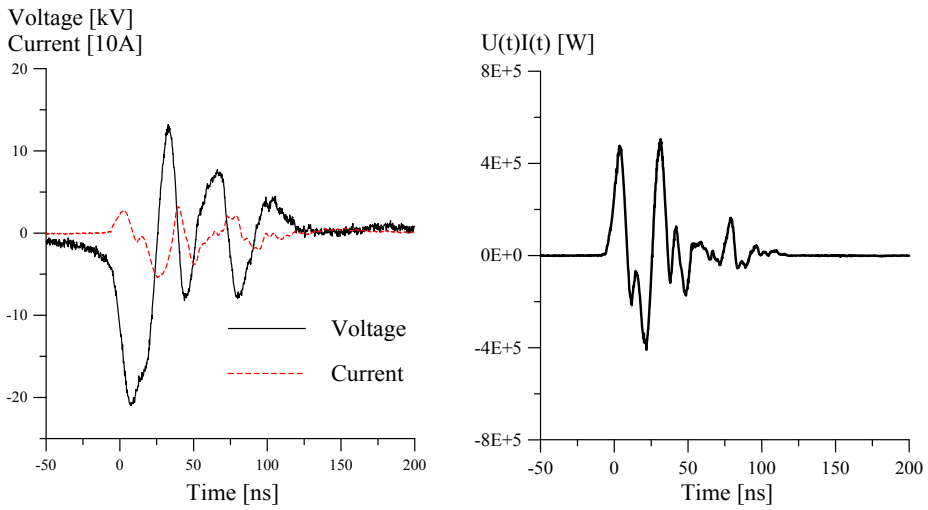

(a) (b)

Figure 3.1: Raw single pulse voltage and current waveforms (left) and instantaneous power (right) without phase shift. Quiescent air, P=760 torr.

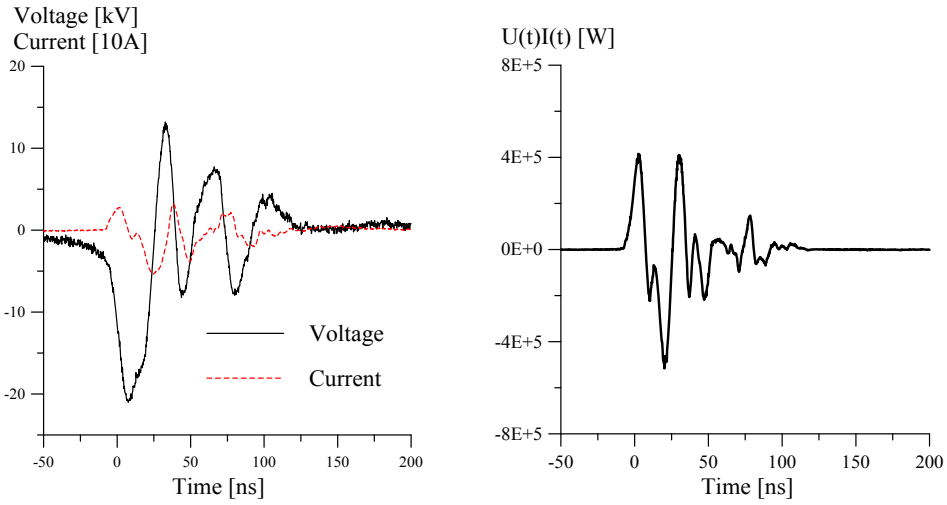

(a) (b)

Figure 3.2: Single pulse voltage and current waveforms (left) and instantaneous power (right) with a 1.4 nsec phase shift incorporated. Quiescent air, P=760 torr.

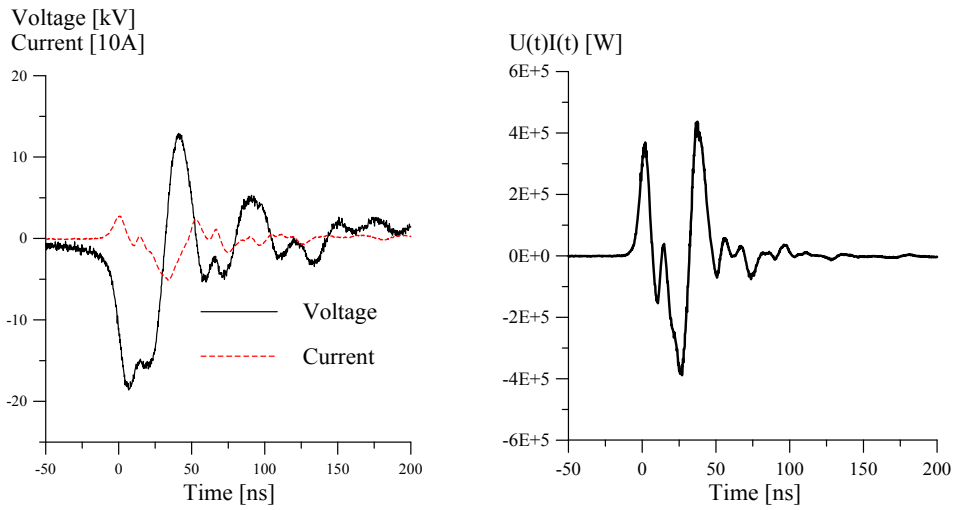

(a) (b)

Figure 3.3: Single pulse voltage and current waveforms (left) and instantaneous power (right) with a 1.4 nsec phase shift incorporated. Air, P=70 torr, ν=50 kHz, $\dot{m}$ =0.8 g/sec (u=14.7 m/sec).

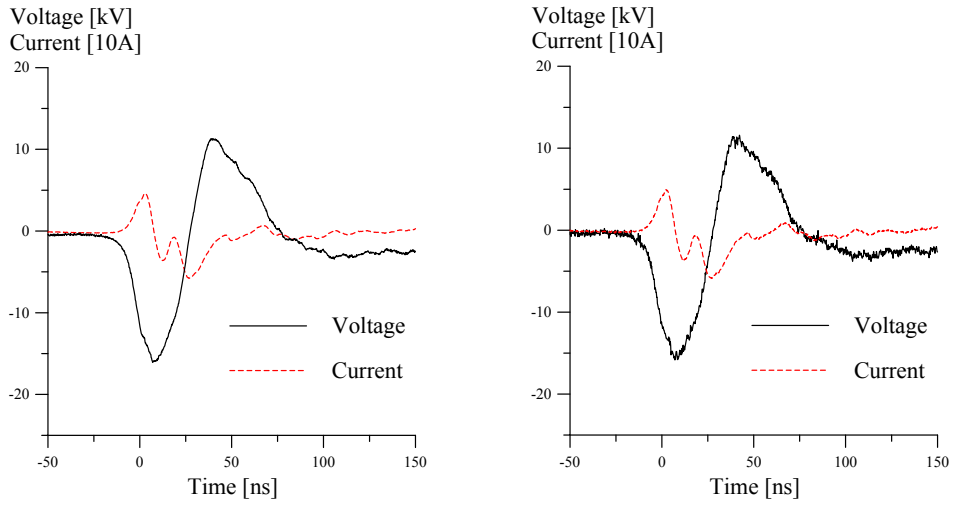

(a) (b)

Figure 3.4: Single pulse voltage and current waveforms in air (left) and in a stoichiometric ethylene-air mixture (right) P=70 torr, ν=50 kHz, $\dot{m}$ =1.2 g/sec, u=22.0 m/sec.

Table 3.1 summarizes the results of pulse energy measurements in air and in air/fuel mixtures at different mass flow rates. It can be seen that pulse energies in air and in a stoichiometric ethylene-air mixture are reproducible and are in the range of 2.0-2.3 mJ. At these conditions, the average load matching coefficient, defined as the difference between the forward and the reflected pulse energies divided by the forward pulse energy was approximately 25%, at the average forward pulse energy is of 7 to 8 mJ, as shown in Table 3.1. Again, the forward and the reflected pulse energies were estimated as the positive and the negative contributions to the integrand in the time integral of the instantaneous power, $\int U(t)I(t)dt$, respectively, where $U(t)$ and $I(t)$ are the voltage and current waveforms such as shown in Figs. 3.2-3.4.

A train of high voltage pulses generated at the pulse repetition rate of ν=50 kHz, at the same flow conditions as in Fig.3.3, is shown in Fig. 3.5. It can be seen that at this pulse repetition rate, the voltage duty cycle is extremely low, ~30 nsec / 20 μsec ~ 1/1000. High reduced electric field during the pulses makes possible efficient ionization, dissociation, and electronic excitation of molecular species by electron impact, the rates of which have strong exponential dependence on E/N [28]. On the other hand, short pulse duration and low duty cycle greatly improve the plasma stability. Basically, the pulse duration, ~30 nsec, is much shorter than characteristic time for the ionization instability development, ~10^{-3}-10^{-4} sec [28]. For the pulse energy of 2.0-2.3 mJ and the pulse repetition rate of 50 kHz, the time-averaged discharge power is 100-115 W.

	Pressure (torr)	Flow rate (g/sec)	Forward energy (mJ)	Reflected energy (mJ)	Coupled energy (mJ)
Air	760	0	6.84	6.84	0
Air	70	0.8	7.22	5.00	2.22
Air	70	0.8	7.77	5.52	2.25
Air	70	1.2	7.94	5.91	2.03
Air/C_2H_4, Φ=1	70	0.8	7.96	5.66	2.30
Air/C_2H_4, Φ=1	70	1	8.07	6.06	2.01
Air/C_2H_4, Φ=1	70	1.2	8.12	6.12	2.00
Air/C_2H_4, Φ=1	70	1.4	7.95	5.83	2.12
Air/C_2H_4, Φ=1	70	1.6	7.82	5.77	2.05

Table 3.1: Summary of single pulse energy measurements.

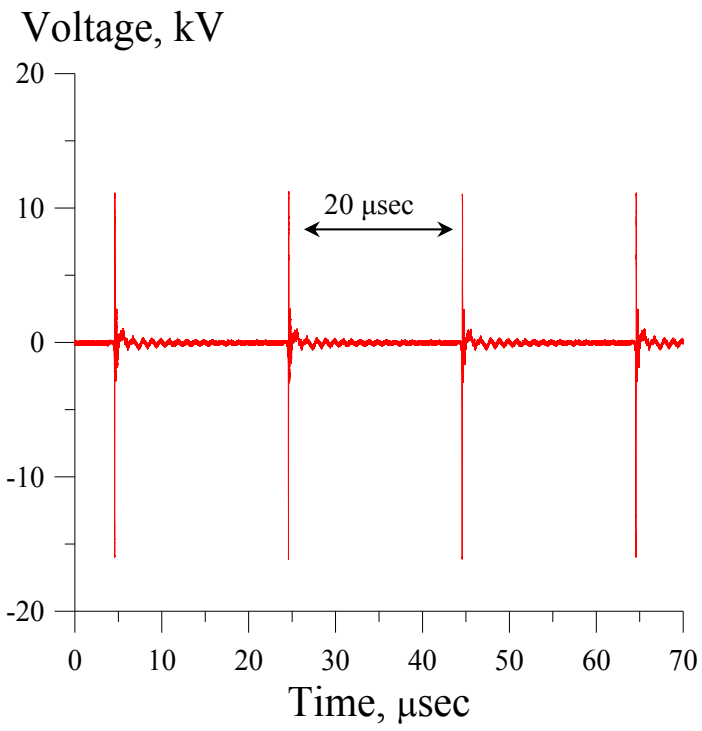

Figure 3.5: High voltage pulse sequence at ν=50 kHz. Air, P=70 torr, $\dot{m}$ =0.8 g/sec (u=14.7 m/sec).

3.1.2 Time-averaged emission spectroscopy measurements

Figure 3.6 shows a typical photograph of a flame originating in the plasma and extending downstream through the test section, at the conditions when ignition was achieved, in a stoichiometric ethylene-air flow at a pressure of P=70 torr and a pulse repetition rate of ν=50 kHz. After ignition, the flame in the test section remains steady as long as the discharge is on. Turning the discharge off results in flame extinction, since the test section does not have a flameholder. Emission spectra of the plasma and of the flame region downstream of the plasma have been obtained in air and in a stoichiometric ethylene-air mixture at a mass flow rate of $\dot{m}$ = 1 g/sec (u=18.4 m/sec) and test section pressure of P=70 torr, at the conditions when ignition was achieved. Figures 3.5-3.10 summarize these results.

Figures 3.7 and 3.8 show C_2 ($A^3\Pi_g \rightarrow X'^3\Pi_u$) emission spectra ($C_2$ Swan band system, $\Delta v=v'-v''=0$ sequence) in a stoichiometric ethylene-air flow, from the discharge region and the flame region, respectively. C_2 Swan bands appear both in the plasma and in the flame and have similar intensities. Figures 3.9 and 3.10 show CH ($A^2\Delta \rightarrow X^2\Pi$) emission spectra (CH 4300 Å band system) from the discharge region and the flame region, respectively. The CH emission signal in the discharge is considerably weaker compared to the nitrogen second positive system emission, N_2 ($C^3\Pi_u \rightarrow B^3\Pi_g$) (see Fig. 3.8). On the other hand, CH emission from the flame, where the $N_2(C^3\Pi_u)$ state is quenched, is easier to distinguish. In the present work, CH 4300 Å band system emission has been used as a flame indicator, as well as for the flame temperature measurements. Figures 3.11 and 3.12 show CN ($B^2\Sigma \rightarrow X^2\Sigma$) emission spectra (CN violet band system) from the discharge region and the flame region, respectively. Again, CN spectra are

easier to identify in the flame region, where the N_2 second positive band emission intensity is greatly reduced.

These results show that radical species such as C_2, CH, and CN are generated both in the plasma and the flame regions, most likely due to electron impact processes and plasma chemical reactions. Note that these emission spectroscopy data cannot be used for radical species concentrations measurements which would require absorption spectroscopy or laser induced fluorescence measurements.

N_2 emission:
Plasma temperature

CH emission:
flame temperature

Figure 3.6: Photographs of the repetitively pulsed discharge plasma (visible through the circular windows in the test section, left) and of the flame extending downstream of the discharge section (right). Ethylene-air flow, Φ=1, P=70 torr, $\dot{m}$ =0.8 g/sec (u=14.7 m/sec), ν=40 kHz. The flow is left to right. Arrows show the windows used for the plasma and the flame temperature measurements.

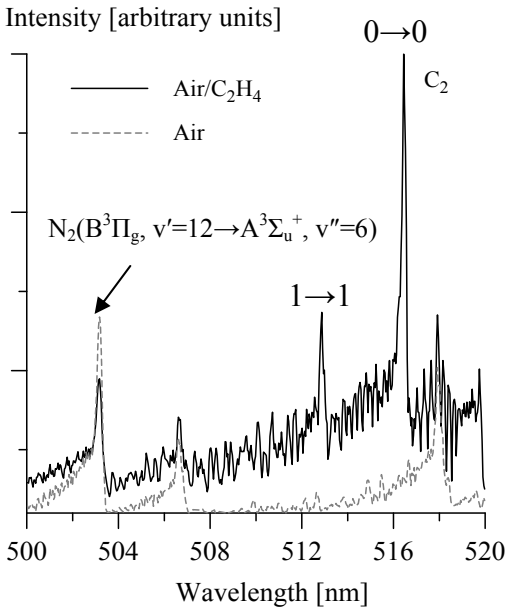

Figure 3.7: C_2 emission spectra (Swan bands) from the discharge region. Air and C_2H_4/air, Φ=1, P=70 torr, ν=50 kHz, $\dot{m}$ =1 g/sec (u=18.4 m/sec).

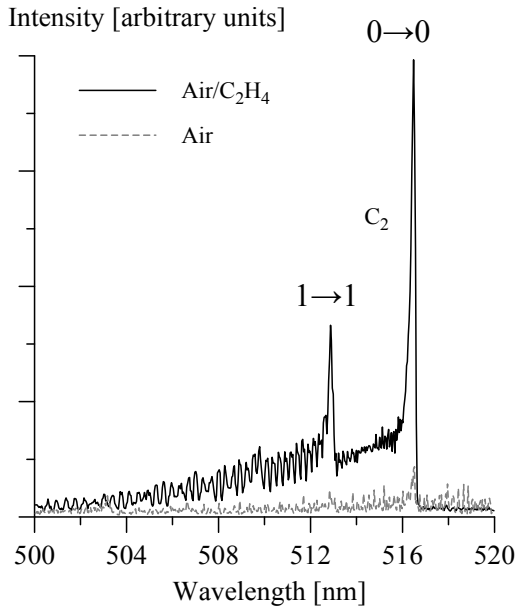

Figure 3.8: C_2 emission spectra (Swan bands) from the flame region. Air and C_2H_4/air, Φ=1, P=70 torr, ν=50 kHz, $\dot{m}$ =1 g/sec (u=18.4 m/sec).

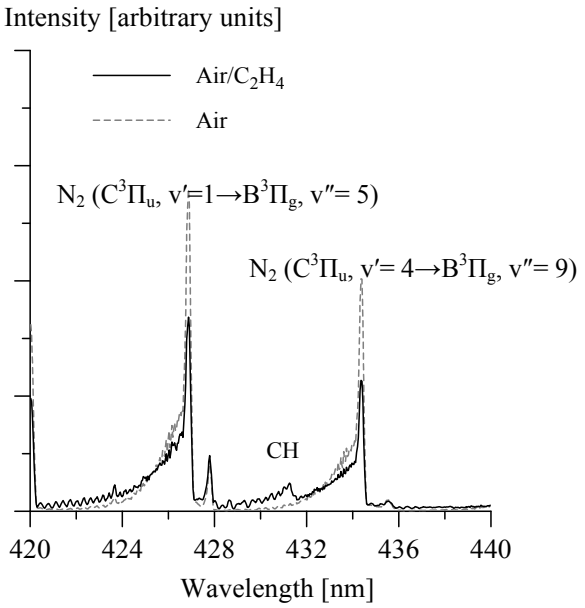

Figure 3.9: CH emission spectra from the discharge region. Air and C_2H_4/air, Φ=1, P=70 torr, ν=50 kHz, $\dot{m}$ =1 g/sec (u=18.4 m/sec).

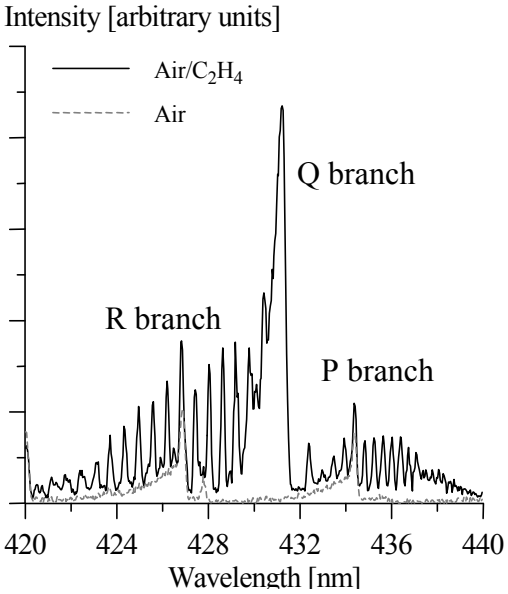

Figure 3.10: CH emission spectra from the flame region. Air and C_2H_4/air, Φ=1, P=70 torr, ν=50 kHz, $\dot{m}$ =1 g/sec (u=18.4 m/sec).

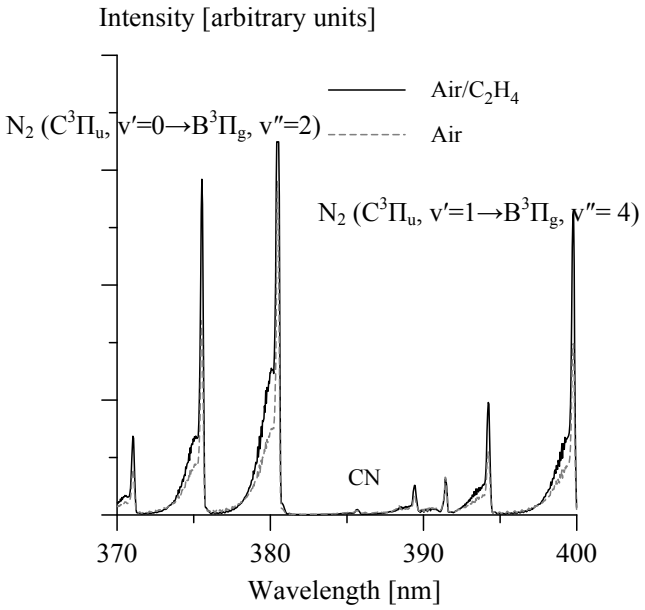

Figure 3.11: CN emission spectra from the discharge region. Air and C_2H_4/air, Φ=1, P=70 torr, ν=50 kHz, $\dot{m}$ =1 g/sec (u=18.4 m/sec).

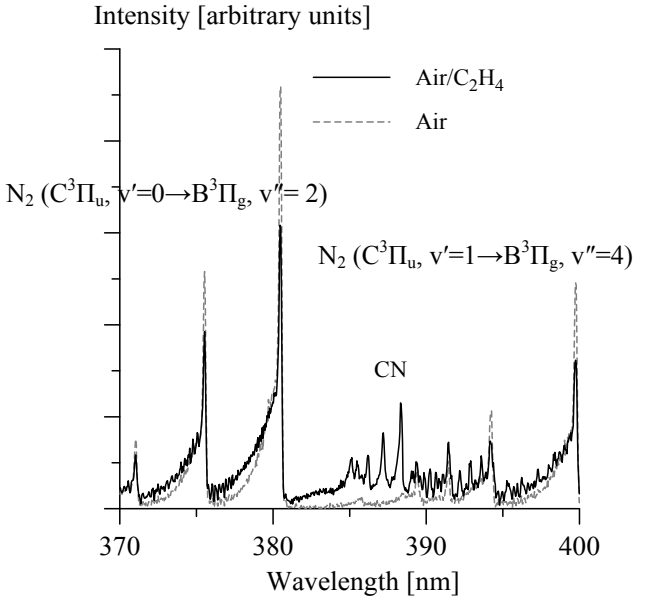

Figure 3.12: CN emission spectra from the flame region. Air and C_2H_4/air, Φ=1, P=70 torr, ν=50 kHz, $\dot{m}$ =1 g/sec (u=18.4 m/sec).

3.1.3 Time-resolved emission spectroscopy measurements

Figure 3.13 shows time-resolved visible emission signal from the air plasma (N_2 second positive band emission, $C^3\Pi_u$, $v'=1 \rightarrow B^3\Pi_g$, $v''=3$ at 375.5 nm) at two different discharge pulse repetition rates, ν=20 kHz and 50 kHz. It can be seen that nitrogen emission is modulated at the pulse repetition rate, reaching maximum during the high-voltage pulses and partially decaying between the pulses. On the other hand, CH emission (CH 4300 Å band system, $A^2\Delta$, $v'=0 \rightarrow X^2\Pi$, $v''=0$ at 431.4 nm) from a stoichiometric ethylene-air mixture in the flame region downstream of the plasma, measured at the same flow conditions and at ν=40 kHz, is relatively steady and does not exhibit such modulation (see Fig. 3.14(a)). This suggests that at these conditions combustion downstream of the plasma is self-sustained. Decreasing the pulse repetition rate to ν=30 kHz both reduces CH emission intensity and makes it much less steady in time, exhibiting sudden increases and suggesting unstable combustion regime sustained by individual high-voltage pulses (see Fig. 3.14(a)). Finally, at ν=20 kHz, CH emission nearly disappears and combustion appears to be not sustained. Since the flow residence time in the discharge section at u=14.7 m/sec is approximately 3.4 msec, these results suggest that self-sustained combustion downstream of the discharge is achieved after the combustible mixture is excited by about 140 high voltage pulses. Time-resolved emission measurements at ν=30 kHz and at different flow velocities, shown in Fig. 3.14(b), are consistent with these results. As can be seen from the Fig. 3.14(b), increasing the flow velocity from the baseline value of u=14.7 m/sec to 44 m/sec, i.e. reducing the number of pulses exciting the combustible mixture from ~180 to ~60 pulses considerably reduces

CH emission intensity and makes it less steady in time, again suggesting unstable combustion regime.

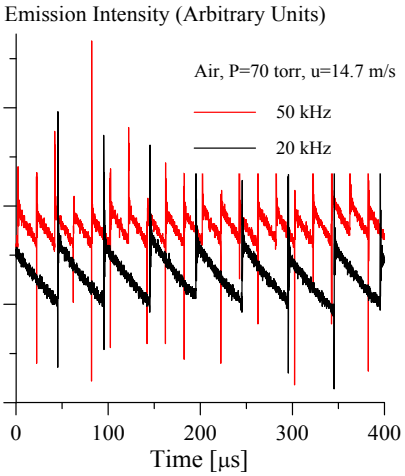

Figure 3.13: Time-dependent N_2 positive system emission signal (375.5 nm) in the pulsed discharge plasma at two different pulse repetition rates, 50 kHz and 20 kHz. Air, P=70 torr, u=14.7 m/sec.

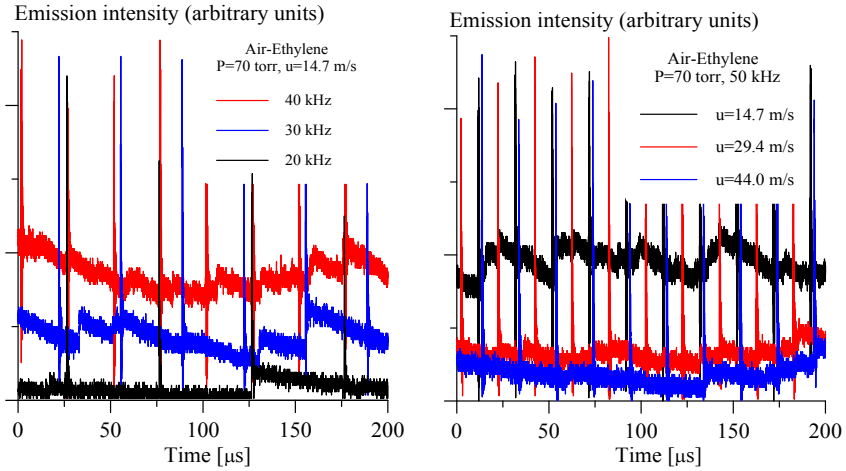

(a) (b)

Figure 3.14: Time-dependent CH emission signal (431.4 nm) in the flame region downstream of the discharge at different pulse repetition rates (left), and different flow velocities (right). Air-ethylene mixture, Φ=1.0, P=70 torr.

3.1.4 Flow temperature measurements

In the present work, visible emission spectra of the plasma (partially rotationally resolved 0→2 and 1→3 bands of the N_2 ($C^3\Pi_u \rightarrow B^3\Pi_g$) band system) have been used to infer the rotational temperature in the plasma. For this, synthetic spectrum has been used, with accurate nitrogen molecular constants [35,36], rotational line intensities [37], and the experimentally measured slit function of the spectrometer. Detailed description of this approach is given in Appendix A. This method of temperature inference has to be used with caution, since the rotational relaxation time at the baseline conditions, test section pressure and temperature of P=0.1 atm, T=300 K is τ_{rot}=12 nsec [38], which is comparable with the radiative lifetime of the N_2 ($C^3\Pi_u$, v=0) state, 38 nsec [39]. For this reason, this temperature inference method needs to be calibrated. In the present experiment, calibration has been done by (i) comparing the plasma temperature measured at a high flow rate and a low pulse repetition rate with room temperature, and (ii) comparing temperatures inferred from N_2 ($C^3\Pi_u \rightarrow B^3\Pi_g$) emission spectra (0→2 and 1→3 bands) in air preheated by an in-line flow heater up to T=20-180^0 C at P=70 torr and $\dot{m}$ =1.0 g/sec, again at a low pulse repetition rate, with thermocouple temperature measurements in the absence of the plasma.

Figure 3.15 shows experimental emission spectra in air at P=70 torr, high mass flow rate of $\dot{m}$ =3.2 g/sec, and low pulse repetition rate of ν=5 kHz (i.e. at the time-averaged repetitively pulsed discharge power of $\dot{Q}$=2.2 mJ · 5 kHz ≈11 W). At these conditions, the flow temperature rise should be very small, $\Delta T = \dot{Q}/(\dot{m} \cdot c_p) \approx 4^0$ K, so the flow should be at near room temperature. Indeed, best agreement between the experimental and the synthetic spectra at these conditions was obtained at T=320±50 ^{0}K.

The experimental emission spectrum, shown in Fig. 3.15, was taken by using the PI-MAX ICCD camera with a 512x512 pixel CCD array, with the spectral resolution of about 0.25 nm.

In temperature measurements in preheated flows, both pulse repetition rate and the time-averaged discharge power were also low, ν=5 kHz and 2.2 mJ · 5 kHz ≈ 11 W, respectively. At these conditions, the estimated flow temperature rise in the plasma at the flow rate of $\dot{m}$ =1.0 g/sec was also small, ~10^0 C. Figure 3.16 compares plasma temperatures inferred from the nitrogen emission spectra with the thermocouple measurements (in the absence of the plasma). It can be seen that the agreement between the two temperatures is very good, within the uncertainty of the temperature inference, ±25 K. This demonstrates applicability and accuracy of this temperature measurement method at the present conditions. Note that the plasma temperature has been measured in the discharge region (as shown in Fig. 3.6), not in the flame region downstream, since N_2 ($C^3\Pi_u \rightarrow B^3\Pi_g$) emission in the flame becomes very weak. Therefore the temperature inferred from the nitrogen second positive band emission spectra is the temperature in the plasma.

Figure 3.17 shows the experimental and the synthetic emission spectra in an air flow at P=70 torr, mass flow rate of $\dot{m}$ =1 g/sec, and pulse repetition rate of ν=40 kHz. The experimental spectrum in Fig. 3.17 is taken using a PIXIS camera with a 1024x256 CCD array, at the spectral resolution of 0.05 nm. At these conditions, the inferred rotational temperature is T=210±30^0 C. Figure 3.18 shows the experimental and the synthetic emission spectra in a stoichiometric ethylene-air mixture, at the same flow and plasma conditions (P=70 torr, $\dot{m}$ =1 g/sec, ν=40 kHz), when ignition was achieved and

flame was generated downstream of the plasma. At these conditions, the inferred rotational temperature in the plasma is significantly higher, T=630±50^0 C. Figure 3.19 compares the two experimental emission spectra shown in Figs. 3.17 and 3.18 (in air and in the ethylene-air mixture). The comparison demonstrates a significant difference between the two spectra, in particular stronger emission from higher rotational levels in the air-ethylene mixture.

The R-branch of the partially rotationally resolved CH($A^2\Delta \rightarrow X^2\Pi$) emission spectra, (0→0) and (2→2) bands, has been used to infer the flame temperature [40, 41]. This method has been previously used to infer hydrocarbon/air flame temperature. In Ref. [41], analysis of high-resolution CH emission spectra showed no evidence of self-absorption, which may considerably affect the temperature value inferred from partially rotationally resolved spectra. Spectroscopic constants of CH molecule, rotational level energies, and rotational line intensities were taken from [42,43]. Details of this approach are discussed in Appendix B. The CH emission spectra were taken from the flame region, as shown in Fig. 3.6. Figure 3.20 compares the experimental CH spectrum in a stoichiometric ethylene-air mixture at P=70 torr, $\dot{m}$=1 g/sec (u=18.4 m/sec), and ν=50 kHz with the synthetic spectrum calculated at the rotational temperature of T=1830^0 C. The flame temperature inferred from comparing the experimental and the synthetic spectra is T=1830±100^0 C.

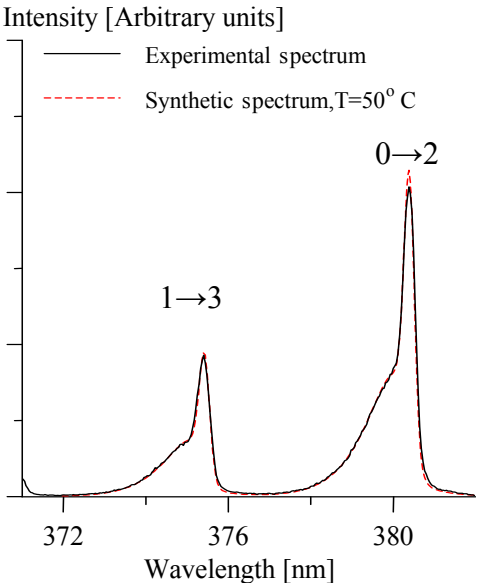

Figure 3.15: Experimental and synthetic N_2 emission spectra (second positive band system, 0→2 and 1→3 bands) in the discharge region. Air, P=70 torr, $\dot{m}$ =3.2 g/sec, ν=5 kHz. Best fit rotational temperature is T=50±50 ºC.

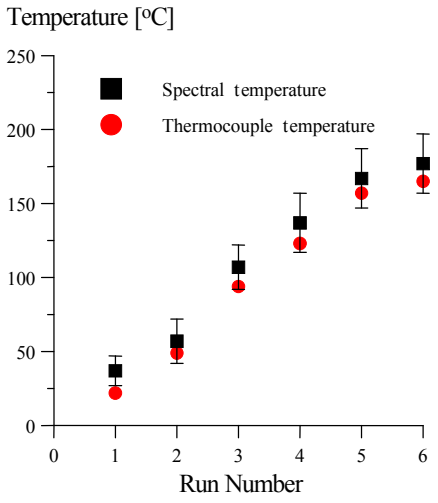

Figure 3.16: Comparison of preheated flow temperatures inferred from the N_2 second positive spectra with thermocouple measurements. Air, P=70 torr, $\dot{m}$ =1.0 g/sec, ν=5 kHz, discharge power 11 W.

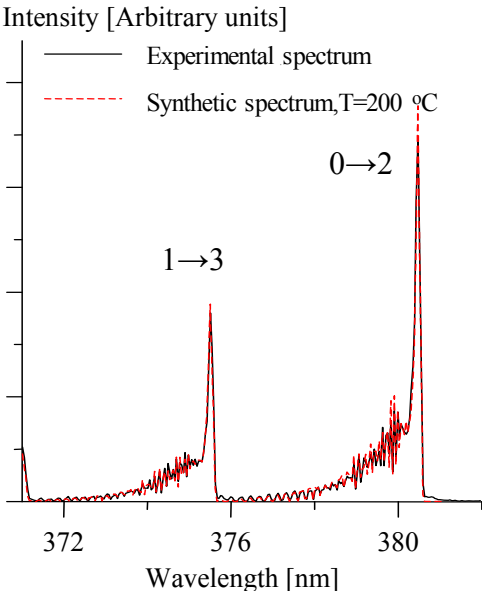

Figure 3.17: Experimental and synthetic N_2 emission spectra (second positive band system, 0→2 and 1→3 bands) in the discharge region. Air, P=70 torr, $\dot{m}$ =1 g/sec (u=18.4 m/sec), ν=50 kHz. Best fit rotational temperature is T=200±30 ºC.

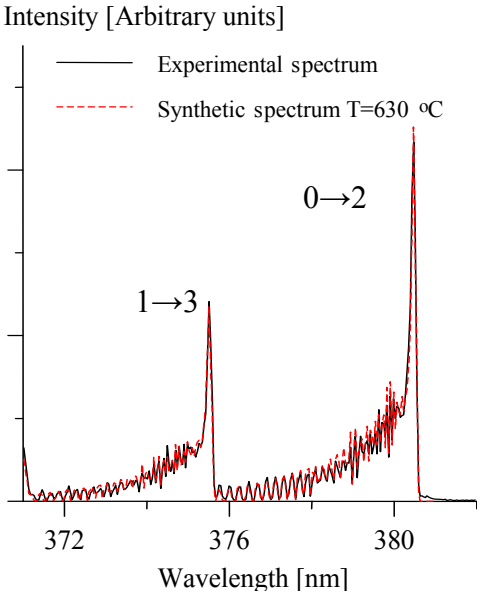

Figure 3.18: Experimental and synthetic N_2 emission spectra (second positive band system, 0→2 and 1→3 bands) in the discharge region. Ethylene-air, Φ=1, P=70 torr, $\dot{m}$ =1 g/sec (u=18.4 m/sec), ν=50 kHz, with flame observed in the test section. Best fit rotational temperature is T=630±50 ºC.

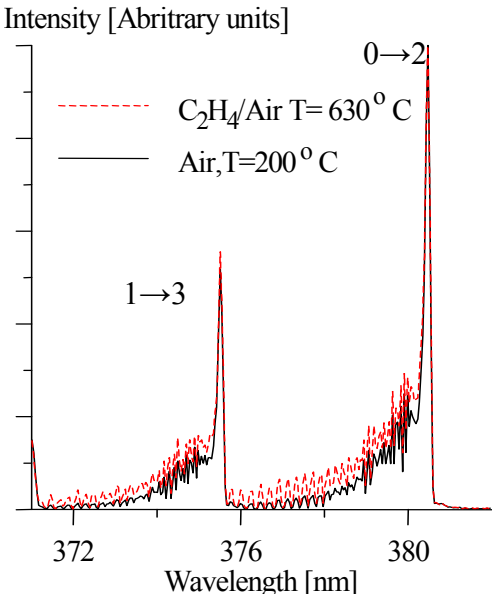

Figure 3.19: Comparison of the experimental N_2 emission spectra (second positive band system, 0→2 and 1→3 bands) in the discharge region. Air and stoichiometric ethylene-air mixture, P=70 torr, $\dot{m}$ =1 g/sec (u=18.4 m/sec), ν=50 kHz.

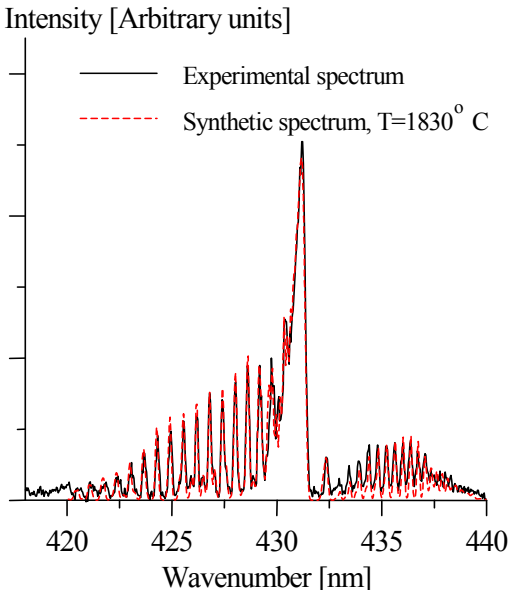

Figure 3.20: Experimental and synthetic CH emission spectra (4300 Å band system, $CH(A^2\Delta \rightarrow X^2\Pi)$) in the flame region. Ethylene-air, Φ=1, P=70 torr, $\dot{m}$ =1 g/sec (u=18.4 m/sec), ν=50 kHz, with flame observed in the test section. Best fit rotational temperature is T=1830±100 ºC.

3.1.5 FTIR absorption spectroscopy measurements

In the present work, we used Fourier Transform (FT) absorption spectroscopy to measure the burned fuel percentage, as well as to identify fuel oxidation/combustion products. Figure 3.21 shows typical FT absorption spectra of an ethylene-air mixture at P=70 torr, mass flow rate $\dot{m} = 1$ g/sec, equivalence ratio Φ=1, and pulse repetition rate ν=50 kHz, with and without the plasma. Figure 3.21 also shows a magnified part of these spectra between 2900 cm^{-1} and 3300 cm^{-1}. At these conditions, ignition was achieved and a stable flame was detected downstream of the plasma (see Fig. 3.6). It can be seen that with the plasma, the amount of fuel left in the flow is greatly reduced, while amounts of main combustion products (CO, CO_2, and H_2O) significantly increase. The percentage of fuel left unreacted in the flow, f, is determined by comparing the intensities of individual absorption lines, with and without the plasma sustained in the test section.

$$f = \frac{n_{fuel}^{plasma}}{n_{fuel}} = \frac{\ln(I_{tr}^{plasma} / I_0)}{\ln(I_{tr} / I_0)} \tag{3.1}$$

Here I_0 is the baseline incident globar signal intensity, I_{tr}^{plasma} and I_{tr} are the transmitted signal intensities with and without the plasma, and n_{fuel}^{plasma} and n_{fuel} are the number densities of the fuel species in the flow with and without the plasma.

From Figure 3.21, which plots the relative absorption signal, $I_{abs} / I_0 = 1 - I_{tr} / I_0$, it can be seen that the use of the repetitively pulsed plasma results in a significant reduction of the fuel concentration and an increase in concentrations of combustion products, CO, CO_2, and H_2O in the flow. It can also be seen that oxidation of fuel does not result in its conversion to other hydrocarbons, such as acetylene, which has an absorption band between 3230 and 3350 cm^{-1} [32]. Such fuel conversion has been

previously observed in fuel-rich methane-air and ethylene-air flows ignited by a transverse RF discharge plasma [21], shown in Fig 3.22. Similar results (i.e. fuel oxidation into CO, CO_2 and H_2O) have been detected in CH_4-air flows. As an example, Fig. 3.23 shows FT absorption spectra in a stoichiometric methane-air flow at P=90 torr, $\dot{m} = 1$ g/sec, and ν=50 kHz.

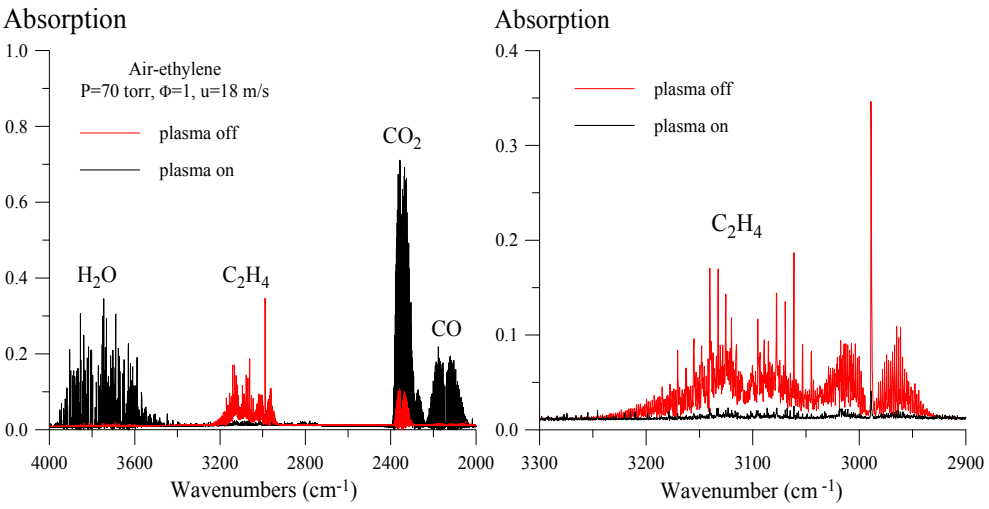

Figure 3.21: Typical FT absorption spectra of the flow sampled downstream of the discharge section, with and without repetitively pulsed plasma. Ethylene-air, Φ=1, P=70 torr, $\dot{m}$ =1.0 g/sec (u=18.4 m/sec), ν=50 kHz.

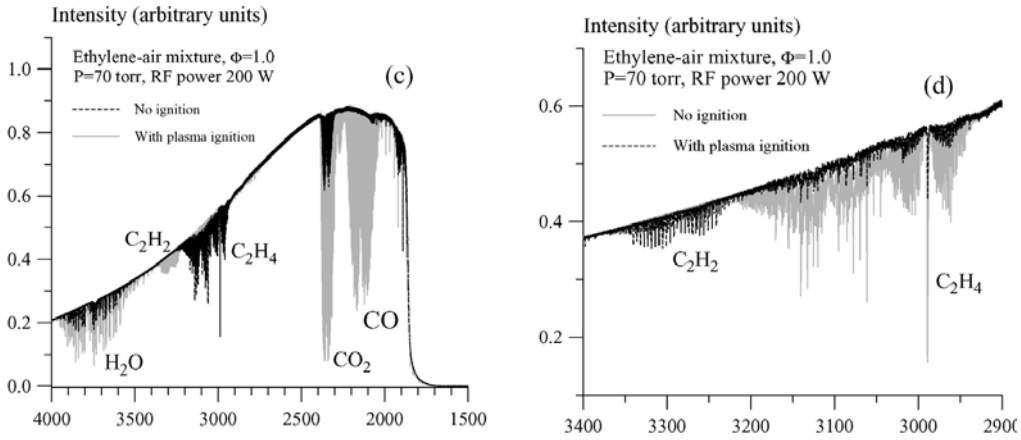

Figure 3.22: FT absorption spectra of a stoichiometric ethylene-air flow ignited by transverse RF discharge [21]. Φ=1, P=70 torr, RF power =200 W, background not subtracted.

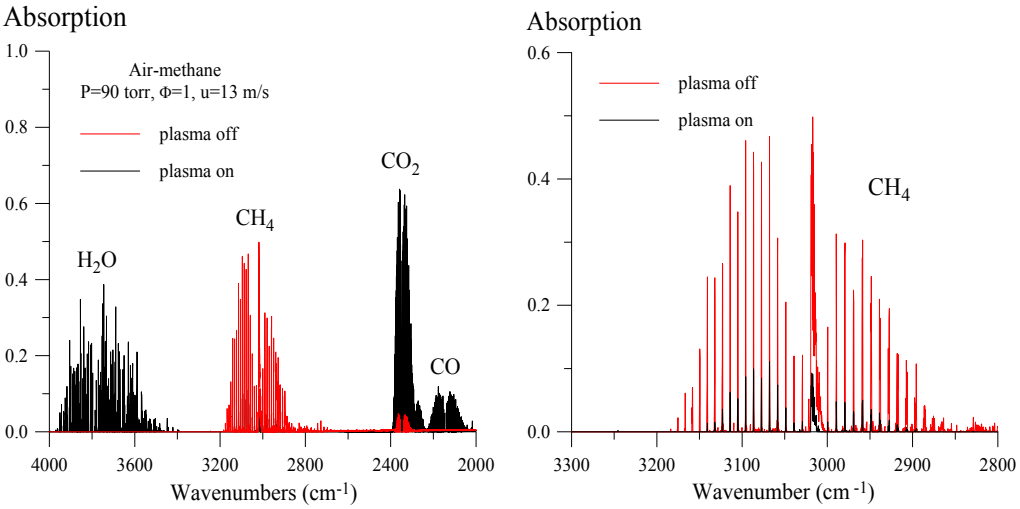

Figure 3.23: Typical FT absorption spectra of the flow sampled downstream of the discharge section, with and without repetitively pulsed plasma. Methane-air, Φ=1, P=90 torr, $\dot{m}$ =1.0 g/sec (u=13 m/sec), ν=50 kHz.

3.1.6 Gaseous fuel ignition by nanosecond discharge plasma

Figure 3.24 shows the flow temperature in the plasma and the reacted fuel fraction, as functions of the flow velocity in a stoichiometric ethylene-air flow at a pressure of P=70 torr and a pulse repetition rate of ν=50 kHz. Figure 3.24 also shows the

results of flow temperature measurements in air plasma (without fuel) at the same flow conditions. It can be seen that while both the air flow temperature and the fuel-air mixture temperature decrease with the flow velocity, as it increased from u=14.7 m/sec to u=44 m/sec (at $\dot{m}$ =0.8-2.4 g/sec), the temperature of the air-fuel mixture is significantly higher, by $\Delta T=200\text{-}350^0$ C. This suggests that the temperature increase may be due to heat generation during plasma chemical fuel oxidation. Note that the measured flow temperature rise of $\Delta T=350^0$ C at u=14.7 m/sec and $\Delta T=200^0$ C at u=44 m/sec (see Fig. 24) correspond to oxidation of approximately 12% and 7% fraction of ethylene in the plasma, respectively (the heat of combustion reaction for a stoichiometric ethylene-air mixture is 3025 kJ/kg). Note that the highest flow temperature measured at the present conditions is approximately 600^0 C, which is much lower than the adiabatic flame temperature at these conditions, $T=2270^0$ C. This is because the temperature is measured in the plasma region, upstream of the flame region (see Fig 3.6).

The results of Fig. 3.24 also suggest that when the plasma temperature approaches autoignition temperature (for ethylene-air mixtures, $T_{auto}=600\text{-}700^0$ C at P=70 torr [23], see Section 5.1.5), ignition occurs downstream of the plasma. Note that although complete combustion was achieved only at u=14.7 m/sec (reacted fuel fraction of 95%, see Fig. 3.24), ignition was produced and flame was detected in the entire range of flow velocities of up to u=44 m/s, i.e. at the air plasma temperatures as low as $T=120^0$ C (see Fig. 3.24). A long and stable flame was detected in the test section even at the conditions when the measured reacted fuel fraction was only a few per cent, at u=44 m/sec (see Fig. 3.24). This suggests that at these conditions most of the fuel burns downstream of the fuel sampling port (see Fig. 2.1). At u=44 m/sec, the estimated discharge energy loading per

unit mass necessary for ignition is 100 W / 2.4 g/sec ~ 40 kJ/kg (or ~0.01 eV/molecule). This is about 1.3% of the heat of combustion reaction. These results demonstrate that ethylene-air flows can be ignited by the repetitively pulsed plasma at low plasma temperatures, and with little flow preheating by the plasma.

Figure 3.25 summarizes the results of plasma assisted combustion measurements in ethylene-air mixtures at P=70 torr, $\dot{m}$ =1.0 g/sec (u=18.4 m/sec), ν=50 kHz, for different equivalence ratios. It can be seen that both the flow temperature and the reacted fuel fraction are highest at near stoichiometric conditions, T=490^0 C and 72-87%, respectively.

To verify whether the temperature rise in the air-fuel flow, compared to the air flow (see Fig. 3.24), is indeed due to plasma chemical fuel oxidation rather than relaxation of excited species generated in the air plasma, which may store some of the energy added to the flow by the discharge, the entire series of measurements shown in Fig. 3.24 was repeated after air was replaced with nitrogen. The results are summarized in Fig. 3.26. It can be seen that in this case the temperature rise in the nitrogen-fuel flow, compared to the nitrogen only flow, is much less significant, only about ΔT=50^0 C. This modest temperature increase is most likely due to faster relaxation of energy stored in the electronically and vibrationally excited nitrogen molecules in the presence of ethylene, in quenching processes such as

$$N_2(A^3\Sigma_u^+, B^3\Pi_g, C^3\Pi_u, a'^1\Sigma_u^-) + C_2H_4 \rightarrow N_2 + products \qquad (3.2)$$

Experimentally measured rate coefficients of these processes are comparable with the gas kinetic rate [44-46]. From Figure 3.26, one can also see that at these conditions the reacted fuel fraction does not exceed 5%, which is close to the uncertainty of the present

FTIR spectroscopy measurements. Summarizing, the results shown in Figs. 3.24 and 3.26 demonstrate that (i) temperature rise in the air-fuel plasma indeed occurs due to energy release during plasma chemical fuel oxidation, and (ii) direct fuel dissociation by electron impact and quenching processes of Eq. (3.2) is a relatively minor reaction channel.

The dependence of the plasma temperature and of the reacted methane fraction on the flow velocity and the equivalence ratio, measured at P=100 torr and ν=50 kHz, is similar to the results for ethylene-air mixtures (compare Figs. 3.27 and 3.28). Again, it can be seen that ignition is achieved, and a significant amount of fuel reacts, at flow velocities of u=10-23 m/sec ($\dot{m}$ =0.8-1.8 g/sec) and air flow temperatures as low as T=100-200°C, and that the highest flow temperature, T=430°C, and reacted fuel fraction, 75-88%, are achieved at near stoichiometric conditions.

At the present experimental conditions, the pulsed discharge power budget is rather low, $\sim 2.2\,mJ \cdot 50\,kHz \approx 110\,W$. This is significantly lower than the heat of combustion,

$$\begin{aligned} Q &= \dot{m}_{fuel} \cdot (H_{react} - H_{prod}) = \dot{m} \cdot \frac{H_f^o(C_2H_4) - 2 \cdot H_f^o(CO_2) - 2 \cdot H_f^o(H_2O)}{\mu(C_2H_4)} \\ &= \dot{m}_{fuel} \cdot \frac{52.47\,kJ/mol - 2 \cdot (-393.52\,kJ/mol) - 2 \cdot (-241.83\,kJ/mol)}{28\,g/mol} \\ &= \dot{m}_{fuel} \cdot 47.3\,kJ/g\,. \end{aligned} \tag{3.3}$$

Stoichiometric coefficients in Eq. (3.3) were obtained from the ethylene oxidation reaction,

$$C_2H_4 + 3O_2 + 3 \cdot 3.78N_2 \rightarrow 2CO_2 + 2H_2O + 3 \cdot 3.78N_2\,. \tag{3.4}$$

For $\dot{m}$ =3 g/s (flow velocity u=55 m/s), which is the highest flow rate at which ignition was achieved, and Φ=1 ($\dot{m}_{fuel}$ =0.195 g/sec), Q=9.2 kW >> 110 W. This shows that

plasma assisted ignition requires discharge power of approximately 1% of the heat of combustion.

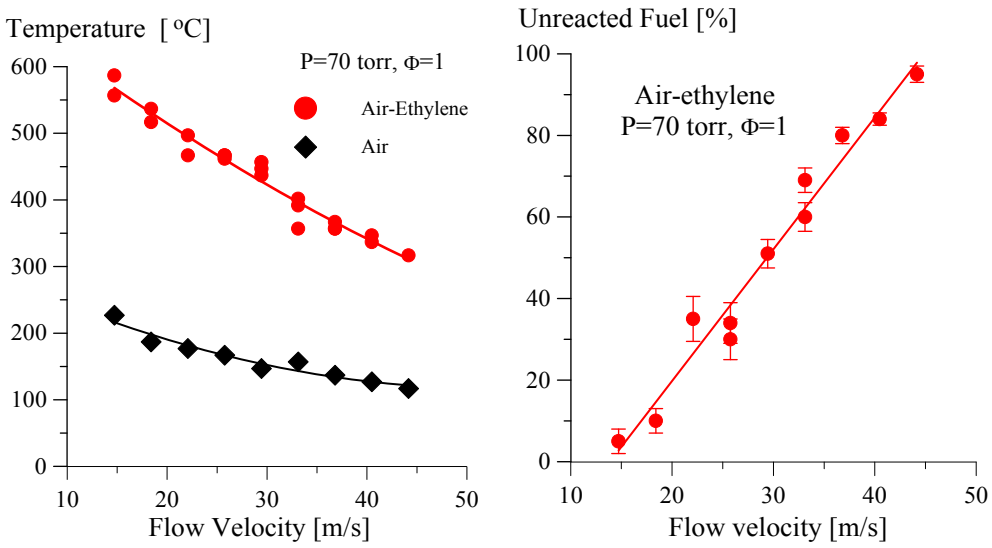

Figure 3.24: Flow temperature in the discharge section and unreacted fuel fraction downstream of the plasma as functions of the flow velocity. Ethylene-air, P=70 torr, equivalence ratio Φ=1.0, pulse repetition rate 50 kHz.

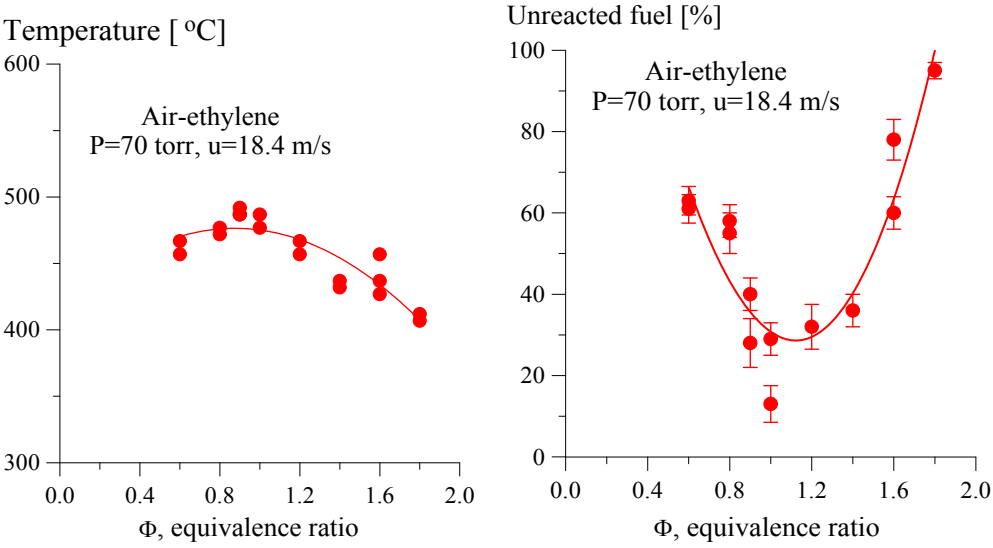

Figure 3.25: Flow temperature in the discharge section and unreacted fuel fraction downstream of the plasma as functions of the equivalence ratio. Ethylene-air, P=70 torr, mass flow rate $\dot{m}$ =1.0 g/sec, pulse repetition rate 50 kHz.

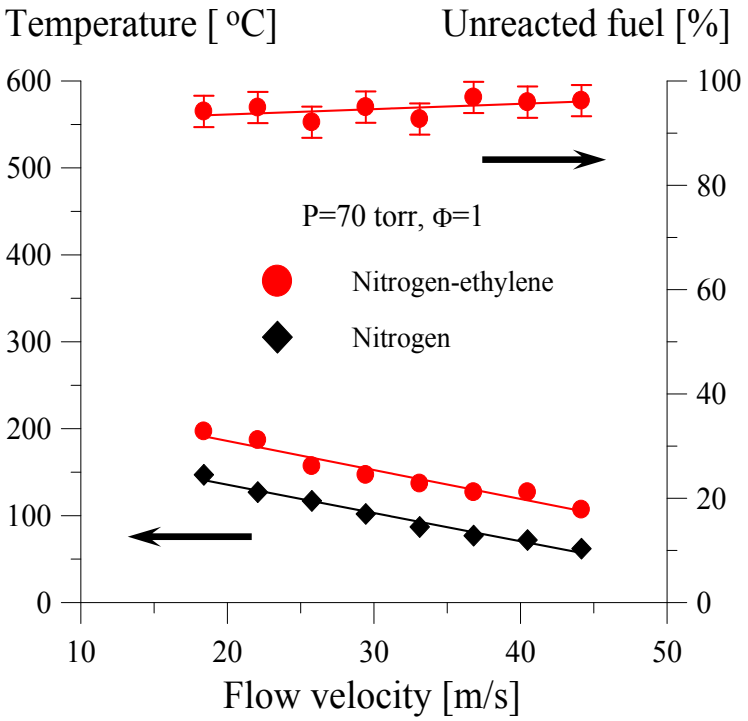

Figure 3.26: Flow temperature in the discharge section and unreacted fuel fraction downstream of the plasma as functions of the flow velocity. Nitrogen and ethylene-nitrogen mixture, Φ=1, P=70 torr, $\dot{m}$ =1.0 g/sec (u=18.4 m/sec), ν=50 kHz.

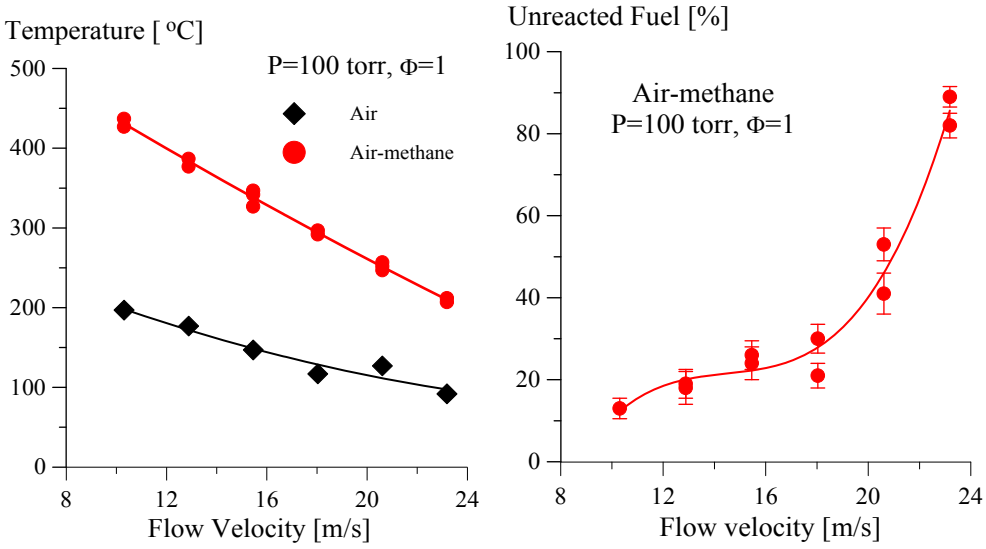

Figure 3.27: Flow temperature in the discharge section (left) and unreacted fuel fraction downstream of the plasma (right) as functions of the flow velocity. Methane-air, P=100 torr, equivalence ratio Φ=1.0, pulse repetition rate 50 kHz.

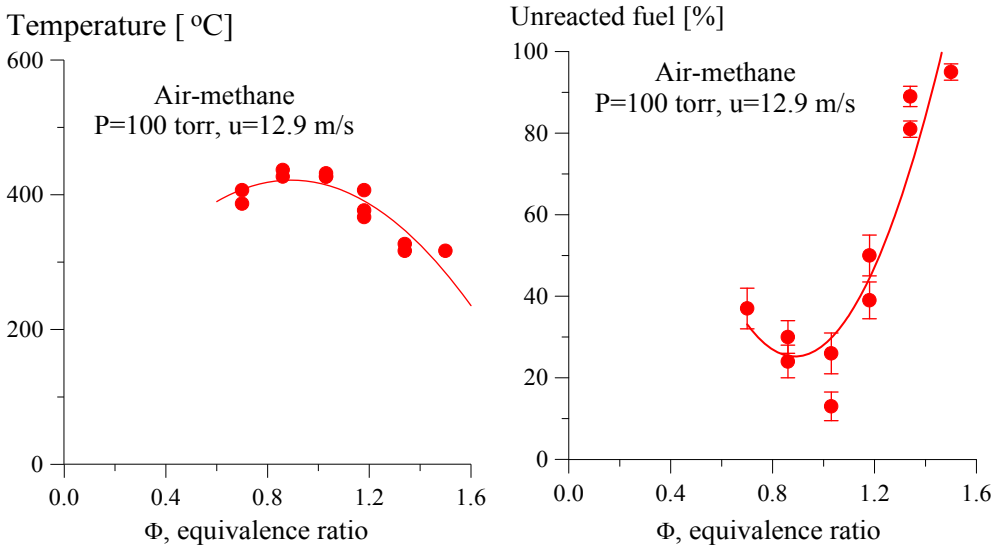

Figure 3.28: Flow temperature in the discharge section and unreacted fuel fraction downstream of the plasma as functions of the equivalence ratio. Methane-air, P=100 torr, mass flow rate $\dot{m}$ =1.0 g/sec, pulse repetition rate 50 kHz.

3.1.7 Ignition at different pulsed discharge durations

To determine whether ignition detected in the present experiments might be due to heating of the pulsed electrode blocks (i.e. test section walls), we conducted ignition tests at different pulsed discharge durations. Note that electrode heating, with subsequent heat transfer to the flow, is a relatively slow process. Therefore, if this "hot surface" ignition is indeed a dominant process in the present experiments, ignition would be likely to occur at long discharge durations ($\tau_{dis} \geq \tau_{HT}$) and less likely to occur at $\tau_{dis} << \tau_{HT}$, where τ_{HT} is the characteristic time for wall heat transfer. At the conditions of these ignition tests, the flow residence time in the discharge was τ_{flow}=3 msec.

Ignition tests have been conducted at different discharge durations and pulse frequencies, in a stoichiometric ethylene-air flow at pressure P=70 torr and $\dot{m}$=1 g/sec (u=18.4 m/sec). The results are summarized in Table 3.2. As can be seen from Table 3.2,

when the pulse repetition rate is lower than 27 kHz, no ignition could be detected in the test section, for discharge times varying from 0.01 sec up to 2 sec. When the pulse repetition rate was higher than 27 kHz, ignition was achieved in the entire range of discharge durations, from 0.01 sec to 1 sec, as shown in Table 3.2. At ν=27 kHz, ignition was sometimes achieved at discharge duration of 0.01 sec but it was not reproducible. At longer discharge durations, 0.1 and 1.0 sec, ignition was achieved in every run but the flame was unstable.

At shorter discharge durations, 1 msec and 2 msec, which correspond to 50 and 100 high-voltage pulses at the pulse repetition rate of ν=50 kHz, neither electrical breakdown nor ignition were reproducibly achieved. Basically, this shows that producing breakdown and establishing a quasi-steady-state pulsed discharge in the test section at the present conditions requires at least a few tens of pulses. Therefore the shortest discharge duration at which ignition could be reproducibly achieved in the present experiments was 0.01 sec.

The results summarized in Table 3.2 suggest that ignition is independent of the discharge duration at the conditions when stable discharge is generated, i.e. at $\tau_{dis} \geq 10$ msec. Basically, ignition either always occurs for $\tau_{dis} \geq 10$ msec or does not occur at all, regardless of what the discharge duration is. To estimate whether plasma assisted ignition may occur in a "hot spot" formed somewhere in the plasma, the minimum discharge duration at which ignition occurs needs to be compared with thermal ignition delay time, predicted by a thermal hydrocarbon combustion mechanism. The results of these calculations and comparison with the experimental data are discussed in Chapter 5.

Plasma temperature measurements at these conditions, shown in Fig. 3.29, also show that, when ignition occurs, the flow temperature is basically independent of the discharge duration (e.g. compare temperatures at ν=50 kHz, for discharge durations of 0.1 sec and 1.0 sec). In both cases, ignition results in temperature rise from approximately 100^0 C to about 500^0 C.

Summarizing, these tests suggest that ignition is not due to a relatively slow process of flow heating by a heated test section wall.

Frequency (kHz)	Discharge time (sec)	Ignition (Yes/No)
10	1	No
	0.1	No
	0.01	No
20	1	No
	0.01	No
25	1	No
	0.01	No
27	1	Yes (Unstable)
	0.1	Yes (Unstable)
	0.01	No
30	1	Yes
	0.01	Yes
50	1	Yes
	0.01	Yes

Table 3.2: Summary of ignition results for different pulse frequencies and discharge duration times. Air/C_2H_4, P=70 torr, Φ=1, $\dot{m}$ =1 g/sec (u=18.4 m/sec).

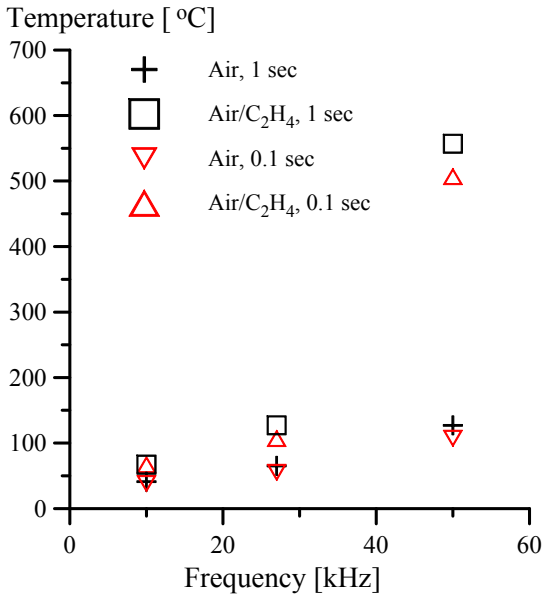

Figure 3.29: Air plasma temperatures for different pulse frequencies and discharge duration times. Air/C_2H_4, P=70 torr, Φ=1, $\dot{m}$ =1 g/sec (u=18.4 m/sec).

3.2 Ignition of gaseous hydrocarbon fuels by a repetitively pulsed discharge (FID pulse generator)

3.2.1 High-voltage pulse characterization

A separate series of ignition experiments was conducted using an FID pulser generating 30 kV, 5 nsec pulse duration, high voltage pulses at a pulse repetition rate of up to 100 kHz (see Section 2.3). The main objective of these measurements was to increase the pulse voltage and frequency, and possibly ignite hydrocarbon-air flows at higher flow velocities.

Figures 3.30-32 show typical single pulse voltage waveforms produced by the FID pulser. In these measurements, a grounded high voltage probe was connected with one of the two test section electrodes, shown in Fig. 2.1. Therefore, positive and negative polarity pulse voltages were measured separately. Figure 3.30 shows voltage waveforms for the first pulse generated without the flow in the test section, in air at P=1 atm. Figures 3.31 and 3.32 show the voltage waveforms for the first pulse in air and in the stoichiometric air-ethylene mixture, respectively, at P=70 torr and a mass flow rate of $\dot{m}$ =1 g/sec. In these measurements, all four channels of the FID pulse generator have been used to generate the highest possible voltage in the discharge section. As can be seen from Figs. 3.30 to 3.32, the peak voltage on the positive electrode is 22-23 kV and the peak voltage on the negative electrode is 17-18 kV, making the total voltage amplitude 39-41 kV. Note that this is approximately two times higher than the peak voltage produced by the CPT pulse generator (see Figs 3.1-3.4). The voltage pulse width at half maximum is approximately 5 nsec. Higher voltage and higher reduced electric

field E/N were expected to generate more ionization and dissociation of molecular species in the test section. On the other hand, shorter pulse duration of the FID pulse generator (5 nsec vs. 30 nsec for the CPT pulse generator) may result in a significantly lower pulse energy coupled to the plasma, and therefore lower radical concentrations generated in the plasma.

Note that the bandwidth of a Tektronix P6015A high voltage probe is 75 MHz, i.e. its time resolution is about 10 nsec. However, comparing the FID voltage pulse shape measured by the high voltage probe and by the back current shunt probe installed in one of the coaxial transmission line cables [47, 48] showed that the use of the high voltage probe for analysis of short duration (~ 5 nsec) pulses is justified. As an illustration, Figure 3.33 shows the FID voltage pulse shape measure by the high voltage probe (bandwidth of 75 MHz), at the end of the transmission cable, and the same voltage pulse shape measured by the current shunt probe (estimated bandwidth of ~1 GHz) inside the cable [48]. In these measurements, the end of the transmission cable was disconnected from the load. As discussed in Section 2.4, at these conditions the voltage at the end of the cable doubles, i.e. for a 7 kV peak voltage pulse propagating through the cable, the peak voltage at the end of the cable should be 14 kV. From Figure 3.33, it can be seen that the two pulse width are fairly close (both 5 nsec FWHM), with the high voltage probe underestimating the voltage amplitude at the end of the cable by only about 15%, (i.e. 12 kV vs. 14 kV).

Figure 3.30: FID pulse generator high voltage pulse shapes on the positive and negative test section electrodes, measured by a high voltage probe. Air, no flow, P=1 atm.

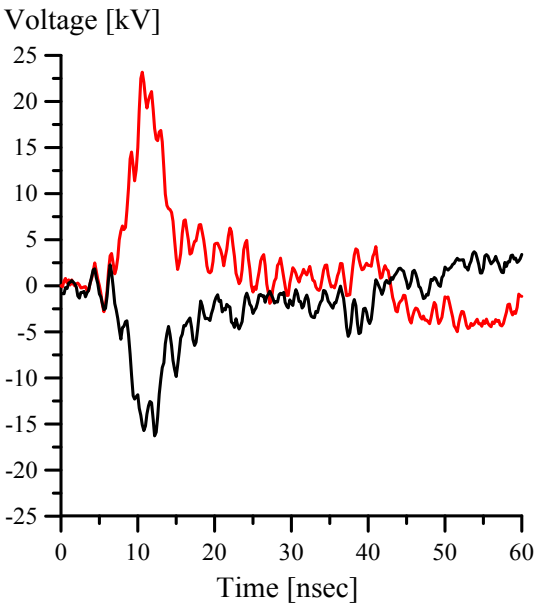

Figure 3.31: FID pulse generator high voltage pulse shapes on the positive and negative test section electrodes, measured by a high voltage probe. Air, mass flow rate $\dot{m}$ =1g/sec, P=70 torr.

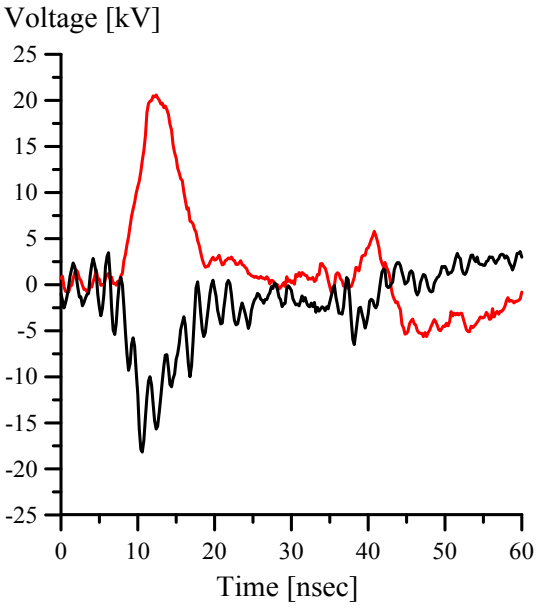

Figure 3.32: FID pulse generator high voltage pulse shapes on the positive and negative test section electrodes, measured by a high voltage probe. Air/C_2H_4, Φ=1, mass flow rate $\dot{m}$ =1g/sec, P=70 torr.

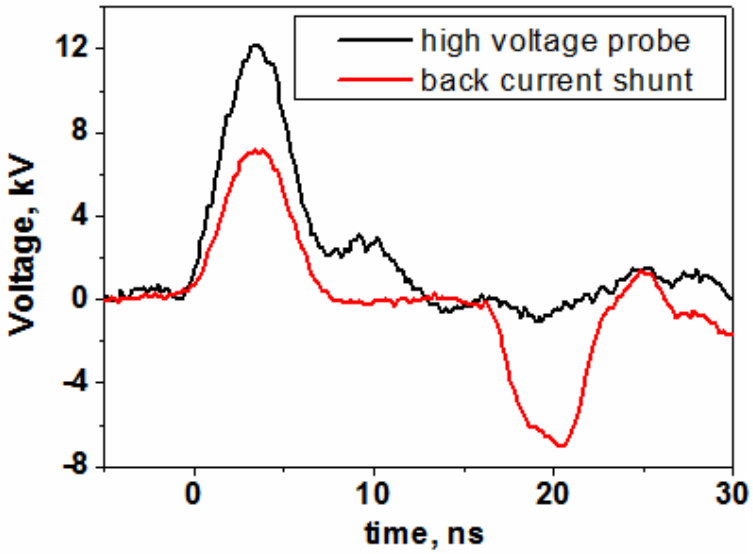

Figure 3.33: Signals from the back current shunt, showing the incident and the reflected high voltage pulses in the transmission cable, and from the high voltage probe, showing voltage at the end of the transmission cable. Pulser is operating on a single channel (single transmission cable), disconnected from the load [47].

3.2.2 Ignition tests

A series of ignition tests was conducted in a stoichiometric ethylene-air mixture, with and without air flow preheating. In these measurements, a stable and diffuse plasma was generated in test section. However, ignition is not detected at the baseline conditions, P=70 torr, $\dot{m}$ =1 g/sec. Figures 3.34 and 3.35 show the unreacted ethylene fraction, as well as air flow and air-fuel flow temperatures at these conditions. Note that the non-preheated air plasma temperature, 50^0 C (see Fig. 3.34), is significantly lower compared to the air plasma temperature generated by the CPT pulse generator at the same flow conditions, 220^0 C (see Fig. 3.24). Also, flow temperature rise when fuel is added to the flow is much lower compared to the results obtained with the CPT pulse generator at these conditions ($\Delta T=100^0$ C, $T_{air\text{-}fuel}=150^0$ C, see Fig. 3.34 vs. $\Delta T=380^0$ C, $T_{air\text{-}fuel}= 600^0$ C with the CPT pulser, see Fig. 3.24). This difference suggests that both the pulse energy and possibly the amount of radicals generated by the FID pulser are considerably less than for the CPT pulser.

To compare the performance of the two pulse generators at nearly the same air plasma temperatures, the air flow was preheated using a 6 kW in-line flow heater, discussed in Section 2.1. In this case, room temperature ethylene was injected into the preheated air flow downstream of the heater through an M1 fuel injector nozzle and the fuel-air flow was premixed in the in-line flow mixer downstream of the fuel injector. The preheated air-fuel temperature without plasma (up to 100^0 C) was measured by a thermocouple installed in the test section (see Fig. 2.2).

The results of these measurements are summarized in Figs. 3.34 and 3.35. It can be seen that although air flow preheating up to 100^0 C does increase the air plasma

temperature, up to 130^0 C (see Fig. 3.34), this is still lower than air plasma temperature in the plasma generated by the CPT pulse generator at the same flow conditions, T=200^0 C (Fig. 3.24). Also, one can see that adding fuel to the preheated air flow still results in a rather modest plasma temperature rise (less than 100^0 C), compared to the temperature rise in the plasma generated by the CPT pulse generator (up to 350^0 C, Fig. 3.24). In the entire range of air preheating temperatures, the oxidized fuel fraction did not exceed 10% (see Fig. 3.34).

Based on these results, we conclude that ignition in air-fuel plasma generated by the FID pulse generator does not occur due to a lower pulse energy coupled to the flow, which results in a lower plasma temperature and possibly in lower radical concentrations in the flow. Qualitatively, this would result to a slower net rate of plasma chemical fuel oxidation reactions.

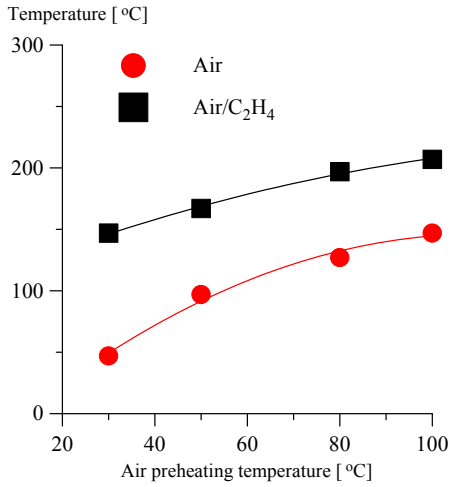

Figure 3.34: Plasma temperature in the discharge section vs. air flow preheating temperature. Ethylene-air, Φ=1, P=70 torr, mass flow rate $\dot{m}$ =1.0 g/sec (u=18.4 m/s), v=100 kHz.

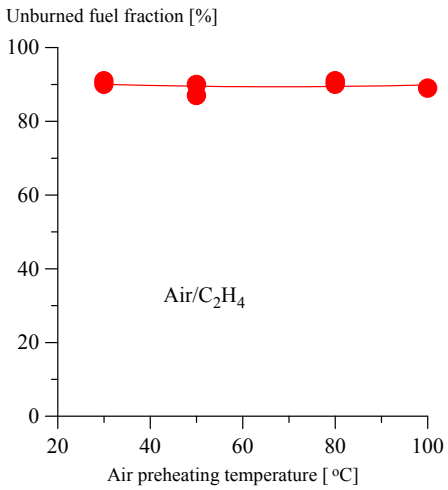

Figure 3.35: Unreacted fuel fraction downstream of the plasma vs. air flow preheating temperature. Ethylene-air, Φ=1, P=70 torr, mass flow rate $\dot{m}$ =1.0 g/sec (u=18.4 m/s), v=100 kHz.

3.3 Ignition of liquid hydrocarbon fuels by a repetitively pulsed discharge (CPT pulse generator)

3.3.1 Fuel concentration calibration

Determining liquid fuel vapor concentration in the flow requires calibration since measuring the fuel flow rate in this case is not sufficient. Indeed, even if the saturated vapor pressure of the fuel is high, there is no guarantee that all injected fuel would evaporate during the flow residence time in the test section. As discussed in Section 2.1, liquid fuel was injected through a spray nozzle into the air flow approximately 30 cm upstream of the test section, as shown in Fig. 2.1. For the calibration, the FTIR spectrometer absorption cell was evacuated and filled with methanol vapor by injecting liquid methanol into the cell, after which air was added to the cell. Methanol vapor pressure in the cell was measured a few minutes after injecting liquid methanol to allow for its complete evaporation and temperature equilibration. In all these measurements,

methanol partial pressure was kept below the saturated vapor pressure at room temperature, P=59 torr. Mole fraction of methanol vapor in the air-fuel mixture was determined by dividing the methanol partial pressure to the total pressure in the cell. After that, the cell pressure was reduced to P=20 torr by pumping the methanol vapor / air mixture out, and the absorption spectrum was taken. Figure 3.36 shows typical methanol absorption spectrum. The methanol vapor calibration curve, plotted in Fig. 3.37, shows the dependence of the integrated methanol band absorption at 2750-3100 cm^{-1} vs. its mole fraction in the mixture. In Fig. 3.37, mole fraction of 12.2% corresponds to the equivalence ratio of Φ=1. In the present experiments, this calibration curve was used to infer the methanol vapor mole fraction in the flow, with and without plasma, from the FTIR absorption spectra of flow samples at the actual experimental conditions. The absolute uncertainty of the methanol mole fraction inference using the calibration curve shown in Fig. 3.37 is approximately ±1% mole fraction (or ±8% relative uncertainty in the equivalence ratio at stoichiometric conditions).

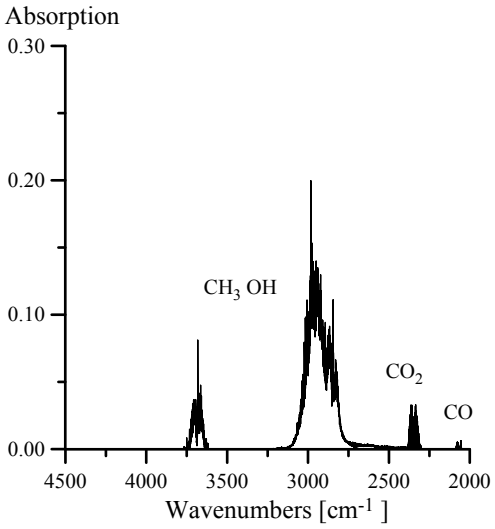

Figure 3.36: Typical methanol FT absorption spectra. FT spectrometer absorption cell pressure P=20 torr, CH_3OH mole fraction in air is 13%.

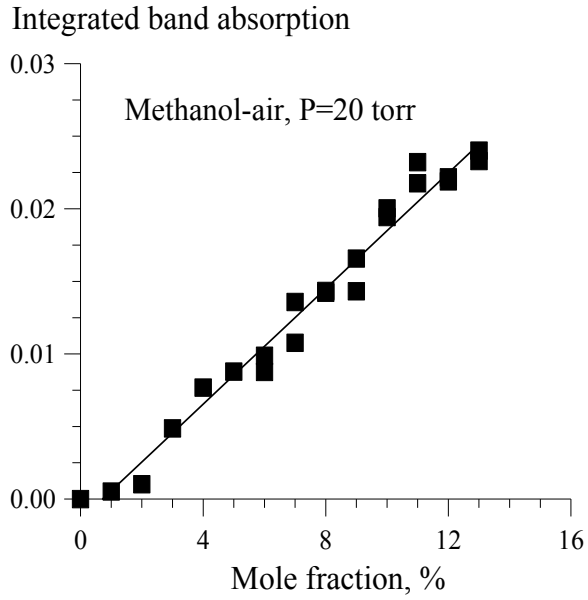

Figure 3.37: Methanol calibration curve. FT spectrometer absorption cell pressure P=20 torr.

3.3.2 Effect of air and fuel preheating on fuel evaporation

In the present experiments, both air and the fuel flows were preheated up to T=60^0 C, as discussed in Section 2.1. Preheating was necessary to accelerate the rate of fuel evaporation in the air flow and to prevented excessive cooling of the air-fuel mixture during evaporation. The saturated vapor pressure of methanol at T=20^0 C is 59 torr, which implies complete fuel evaporation at thermodynamic equilibrium at the present conditions. However, complete evaporation of methanol in an adiabatic stoichiometric liquid methanol / air mixture would result in its cooling by about 140^0 C.

As discussed in Section 2.1, the liquid fuel injection nozzle is rated for mass flow rates of $\dot{m}_{fuel}$=0.52-1.85 g/sec, which is considerably higher than the methanol flow rate in a stoichiometric air-fuel mixture at the present conditions (P=90 torr, $\dot{m}_{air}$=1 g/sec, $\dot{m}_{fuel}$=0.13 g/sec). At these lower flow rates, the spray pattern of the injector nozzle

becomes rather poor which was verified by visual inspection, and the droplet size of injected fuel increase. This reduces the rate of liquid fuel mixing and evaporation. This effect was somewhat countered by preheating the air and the fuel flows.

The effect of air and fuel preheating on liquid fuel evaporation was analyzed in the air-fuel flow without plasma. These measurements have been done at the baseline conditions, in methanol-air flow at P=90 torr, mass flow rate of $\dot{m}$ =1 g/sec, and equivalence ratio of Φ=1.2 (15% methanol mole fraction in the flow). A higher equivalence ratio was used to increase the fuel flow rate and to improve the spray nozzle performance. First, the fuel preheating temperature was varied while the air flow temperature was kept the same, $T_{air}=60^0$ C. The results, plotted in Fig. 3.38, show that the amount of fuel vapor rather weakly depends on the fuel preheating temperature, and that nearly all injected fuel is evaporated. At $T_{fuel}=20\text{-}30^0$ C, the data become less reproducible, and in some runs the fuel vapor mole fraction is as low as 8-10%, while at $T_{fuel}=40\text{-}70^0$ C it remains steady at 14-15%, indicating nearly complete evaporation for Φ=1.2 (see Fig. 3.38). Basically, Figure 3.38 suggests that fuel preheating does not significantly affect its evaporation in a preheated air flow.

Second, the air flow temperature was varied, while the fuel preheating temperature was kept the same, $T_{fuel}=60^0$ C. These measurements showed a strong dependence of the amount of fuel vapor on the air flow temperature, as shown in Fig. 3.39. In this case, it is apparent that preheating the air flow is critical for accelerating fuel evaporation. Note that in this case additional fuel evaporation may also occur on the walls of the test section, whose temperature is close to the temperature of the steady-state flow of preheated air. Summarizing, the results of Figs. 3.38 and 3.39 show that complete

fuel evaporation in the test section, without the plasma, requires operation with air flow preheated up to T_{air}=50-60^0 C.

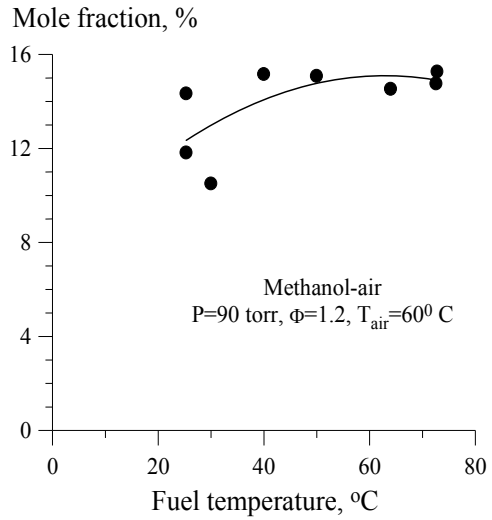

Figure 3.38: Fuel vapor mole fraction vs. fuel preheating temperature. Methanol-air, P=90 torr, mass flow rate $\dot{m}$ =1 g/sec, equivalence ratio Φ=1.2, air preheating temperature Tair=60^0 C.

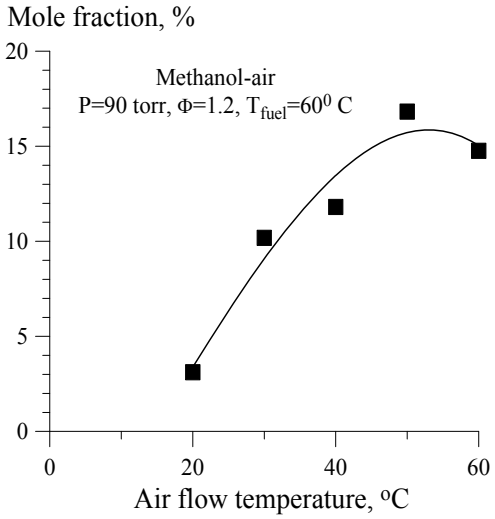

Figure 3.39: Fuel vapor mole fraction vs. air preheating temperature. Methanol-air, P=90 torr, $\dot{m}$ =1 g/sec, Φ=1.2, fuel preheating temperature Tair=60^0 C.

3.3.3 FTIR absorption spectra of liquid fuel and combustion products

In a methanol-air flow at the baseline conditions, at P=90 torr, $\dot{m}_{air}$=1 g/sec (u=13 m/sec), Φ=1.2, and $T_{air}=T_{fuel}=60^0$ C (fuel mass flow rate of $\dot{m}_{fuel}$=0.16 g/sec), ignition was achieved and stable combustion was maintained. Figure 3.40 shows typical FT absorption spectra of the methanol-air flow sampled downstream of the discharge at these conditions, with and without the plasma. Methanol vapor absorption bands at 2750-3100 cm^{-1} and 3650-3750 cm^{-1} can be clearly seen. At these conditions, turning on the repetitively pulsed discharge resulted in flow ignition, with a flame extending through the test section. From Fig. 3.40, it can be seen that the use of the repetitively pulsed plasma results in a significant reduction of ethanol vapor absorption (almost by a factor of 4) and an increase in concentrations of CO, CO_2, and H_2O in the flow. As in the gaseous fuel ignition experiments (see Section 3.1.6), oxidation of methanol does not result in its conversion to other hydrocarbons, such as methane, ethylene, or acetylene. As in the gas phase experiments, burned fuel fraction was determined using Eq. (3.1), and the plasma temperature was inferred from the N_2 second positive system emission spectra.

A separate series of ignition experiments was conducted in ethanol-air mixtures. In this case, ignition was also achieved at the following conditions, P=70 torr, Φ=1.2, mass flow rate $\dot{m}_{air}$=1 g/sec, $T_{air}=T_{fuel}=60^0$ C, ν=50 kHz. Figure 3.41 shows the FT absorption spectra of the air-ethanol mixture and of the combustion products at these conditions. From Fig. 3.41, it can be seen that approximately 30% of ethanol is burned. However, these results were not reproducible run-to-run and the flame remained unstable. This is most likely due to the fact that the mole fraction (and therefore the mass flow rate)

of fuel in a stoichiometric ethanol-air mixture is significantly lower than in stoichiometric methanol-air mixture (6.5% vs. 12.2%). At this low fuel mass flow rate through the injector nozzle, the nozzle spray pattern becomes extremely poor. Therefore, the present liquid fuel ignition experiments were limited to methanol-air mixtures.

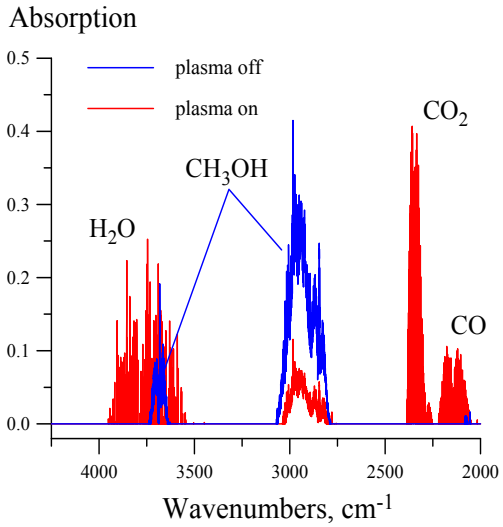

Figure 3.40: Typical FT absorption spectra of methanol-air flow, with and without plasma. P=90 torr, $\dot{m}$ =1 g/sec, Φ=1.2, Tair=60^0 C, Tfuel=60^0 C, ν=50 kHz.

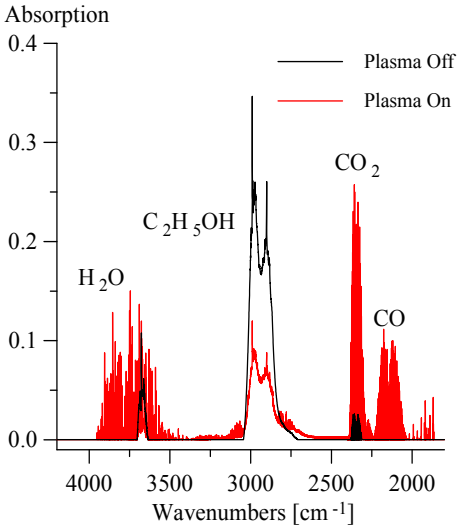

Figure 3.41: Typical FT absorption spectra of ethanol-air flow, with and without plasma. P=70 torr, $\dot{m}$ =1 g/sec, Φ=1.2, Tair=60^0 C, Tfuel=60^0 C, ν=50 kHz.

3.3.4 Liquid fuel ignition results

Figures 3.42 and 3.43 show the effect of the flow velocity in the test section on the temperature of the plasma and on the reacted fuel fraction. These measurements have been done in methanol-air flows at Φ=1.2, P=90 torr, $\dot{m}$ =1.0-2.5 g/sec, ν=50 kHz, and T_{air}= T_{fuel}=60^0 C. Figure 3.42 also shows the results of flow temperature measurements in the air plasma (without fuel) at the same flow conditions, T=130-240^0 C. It can be seen that while both the air flow temperature and the fuel-air mixture temperature decrease with the flow velocity, as it is increased from u=13 m/sec to u=32 m/sec ($\dot{m}$ =1.0-2.5 g/sec), the temperature of the air-fuel mixture remains significantly higher in the entire flow velocity range, by ΔT~250^0 C.

From Fig. 3.43, it can be seen that the reacted fuel fraction also decreases with the flow velocity. Unlike the results of the plasma temperature measurements, which are reproduced very well (see Fig. 3.42), the run-to-run reproducibility of the reacted fuel fraction measurements is not as good. At the baseline conditions (flow velocity of u=13 m/sec), the oxidized fuel fraction varies from 45% to 75% (see Fig. 3.43). This is most likely due to poor spray characteristics and poor mixing of the fuel injected into the air flow at the low flow rate, $\dot{m}_{fuel}$=0.16-0.32 g/sec. However, it is obvious from Fig. 3.43 that the reacted fuel fraction rapidly decreases with the flow velocity, down to less than 10% at u=26 m/sec. The flame in the test section was detected only at fairly low flow velocities, u=13 m/sec and 16 m/sec.

The plasma temperature rise detected in methanol-air flows compared to air flow, ΔT~250^0 C, is nearly independent of the flow velocity and the reacted fuel fraction (see Fig. 3.42), and is detected even when only a few per cent of the fuel is oxidized (see Fig.

3.43). Note that the discharge power in air and in air-fuel mixtures remains approximately the same (~100 W), and is insufficient to explain such a significant temperature rise. At $\dot{m}$ =1.0 g/sec, if the entire discharge power would instantly thermalize, the flow temperature rise would be only ~100^0 C from the initial value of $T_{air}=60^0$ C, which is fairly consistent with the air flow temperature at these conditions, $T=240^0$ C. Therefore the temperature rise after fuel injection must originate from reactions of species generated in the air plasma with fuel.

Since at the conditions of Figs. 3.42, 3.43, at $T_{air}=T_{fuel}=60^0$ C, nearly all fuel injected into the air flow is evaporated (see Figs. 3.38, 3.39), the present results in fact represent ignition of methanol vapor in air. To study feasibility of ignition of liquid / vapor methanol mixtures, the air flow preheating temperature was reduced. Figures 3.44 and 3.45 show the reacted fuel fraction and the plasma temperature at the baseline flow conditions, Φ=1.2, P=90 torr, $\dot{m}$ =1.0 g/sec, ν=50 kHz, and $T_{fuel}=60^0$ C, with the air flow temperature varied in the range of $T_{air}=20\text{-}60^0$ C. From Figure 3.44, it can be seen that reducing the air flow temperature from $T_{air}=60^0$ C to $T_{air}=20^0$ C causes drastic reduction in the reacted fuel fraction, from 50-60% to only 2-3%. This occurs primarily because at low air flow temperatures, fuel evaporation slows down, and the fuel vapor mole fraction in the flow decreases, to 3-10% at $T_{air}=20\text{-}30^0$ C (see Fig. 3.39). This reduces the vapor phase equivalence ratio (i.e. the actual fuel vapor / air ratio to the stoichiometric fuel vapor /air ratio) in the flow to Φ=0.25-0.8. Basically, only a relatively small fraction of injected fuel is evaporated at these conditions. Apparently, additional heating of the air flow in the discharge, at least up to $T=200^0$ C (see Fig. 3.45), remains insufficient to

evaporate the remaining liquid fuel at these conditions, due to the short flow residence time in the discharge.

Figure 3.45 also shows that at low air flow temperatures (T_{air}=20-30^0 C), the plasma temperature rise after the fuel is injected decreases, $\Delta T \sim 70^0$ C at $T_{air}=20^0$ C, compared to $\Delta T \sim 250^0$ C at T_{air}=50-60^0 C, when nearly all injected fuel evaporates. This shows that the plasma temperature rise after fuel injection is proportional to the fuel vapor concentration in the plasma (compare Fig. 3.39 and Fig. 3.45). The results of Figs. 3.44 and 3.45 suggest that preheating of the air flow upstream of the discharge is essential for ignition because the low-temperature plasma does not supply sufficient amount of heat to evaporate preheated liquid fuel injected into a non-preheated air flow.

Second, the fuel preheating temperature was varied from $T_{fuel}=60^0$ C to $T_{fuel}=20^0$ C, still at the baseline flow conditions. From Figure 3.46, it can be seen that reducing the fuel temperature did not result in significant reduction of the reacted fuel fraction. In this case, the oxidized fuel fraction varies from 30% to 60% due to run-to-run variation; however, it does not exhibit a tendency to decrease as the fuel temperature is reduced. From Fig. 3.47, it can also be seen that in this case the temperature rise in the plasma is essentially independent of the fuel preheating temperature. Again, comparison of Fig. 3.38 and Fig. 3.47 suggest that the temperature rise in the plasma is controlled by the fuel vapor mole fraction in the flow. Indeed, in this series of experiments nearly all fuel injected into the flow evaporates (see Fig. 3.38), while the plasma temperature rise, $\Delta T \sim 250^0$ C, remains approximately the same (see Fig. 3.47). In the entire range of fuel temperatures, T_{fuel}=20-60^0 C, the reacted fuel fraction, 30% to 60%, is consistent with the results obtained at $T_{air}=T_{fuel}=60^0$ C and $\dot{m}$ =1.0 g/sec (see Figs. 3.43, 3.46). Basically, the

results of Figs. 3.46 and 3.47 suggest that in this case the low-temperature plasma supplies sufficient amount of heat to evaporate non-preheated liquid fuel injected into a preheated air flow, so fuel preheating may be not necessary.

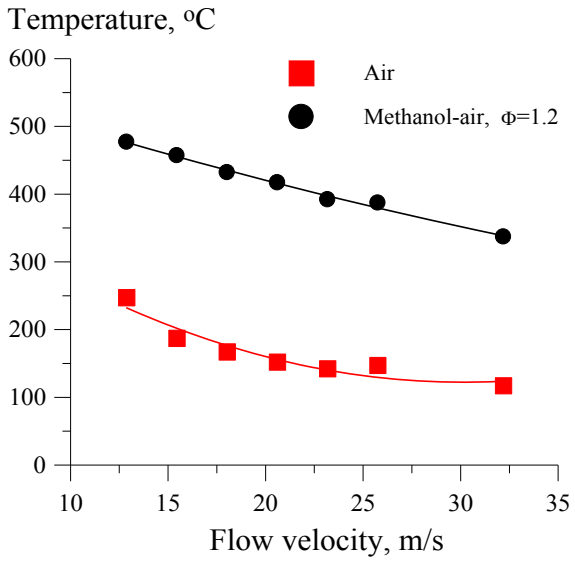

Figure 3.42: Flow temperature in the plasma (with and without fuel) vs. flow velocity. Methanol-air, P=90 torr, Φ=1.2, $T_{air}=60^0$ C, $T_{fuel}=60^0$ C.

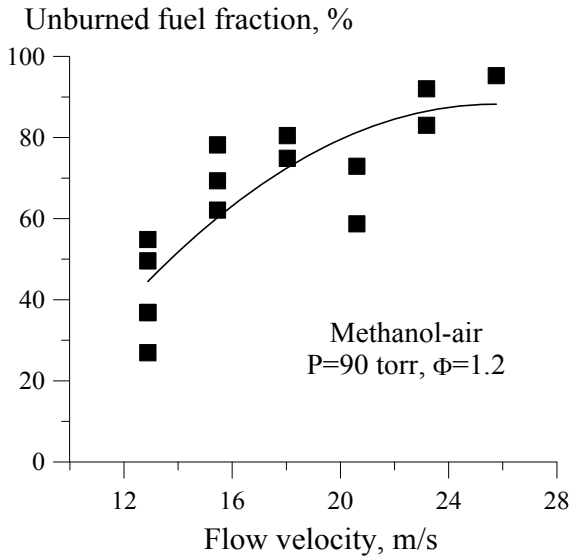

Figure 3.43: Unburned fuel fraction vs. flow velocity. Methanol-air, P=90 torr, Φ=1.2, $T_{air}=60^0$ C, $T_{fuel}=60^0$ C.

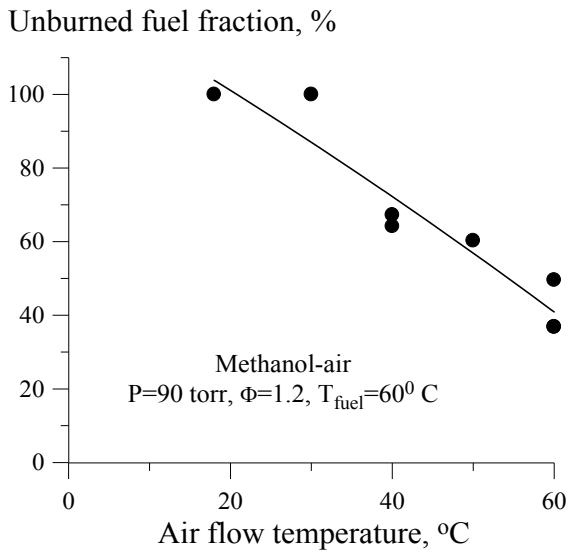

Figure 3.44: Unburned fuel fraction vs. air preheating temperature. Methanol-air, P=90 torr, $\dot{m}$ =1 g/sec, Φ=1.2, T_{fuel}=60^0 C.

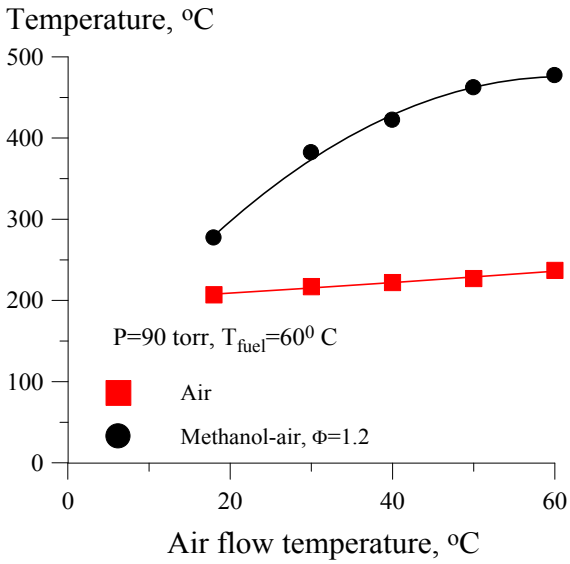

Figure 3.45: Flow temperature in the plasma (with and without fuel) vs. air preheating temperature. Methanol-air, P=90 torr, $\dot{m}$ =1 g/sec, Φ=1.2, T_{fuel}=60^0 C.

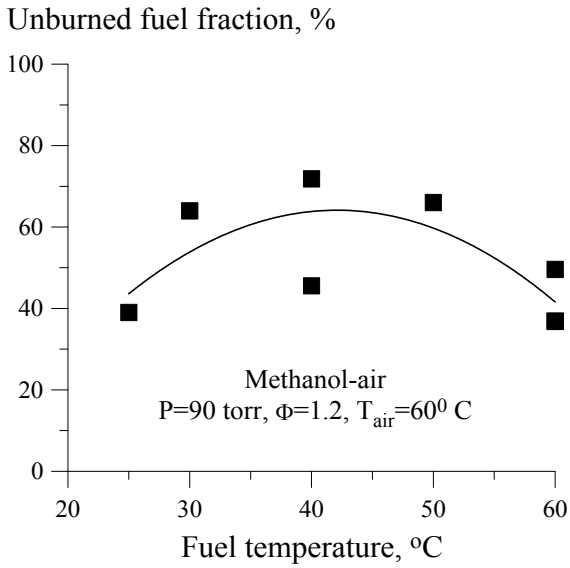

Figure 3.46: Unburned fuel fraction vs. fuel preheating temperature. Methanol-air, P=90 torr, Φ=1.2, $T_{air}=60^0$ C.

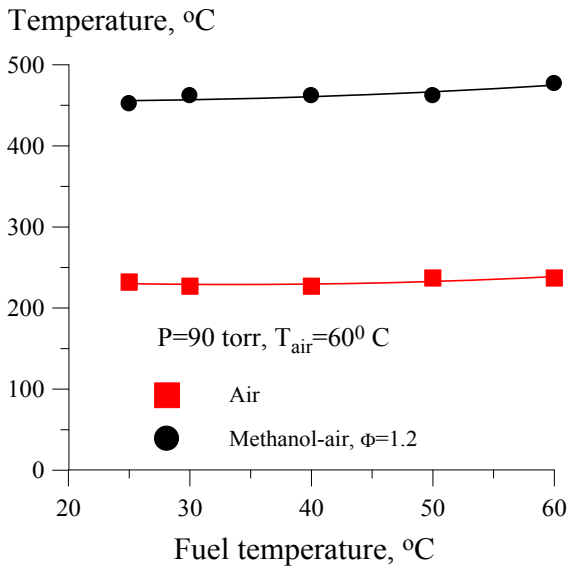

Figure 3.47: Flow temperature in the plasma (with and without fuel) vs. fuel preheating temperature. Methanol-air, P=90 torr, Φ=1.2, $T_{air}=60^0$ C.

CHAPTER 4

KINETIC MODEL

4.1 Kinetic model overview

The main objective of the present kinetic model is to simulate plasma assisted oxidation and ignition of hydrocarbon-air combustible mixtures by a repetitively pulsed, nanosecond pulse duration, low-temperature plasma. The model incorporates quasi-one-dimensional flow equations, chemical kinetics equations for the charged species and the neutral species generated in the plasma, and Boltzmann equation for the energy distribution function of plasma electrons.

The three integral parts of the model (i.e. Boltzmann equation, chemical kinetics equations, and flow equations) are coupled. Specifically, rate coefficients of electron impact processes in the plasma are calculated by the Boltzmann equation solver from the electron energy distribution function (EEDF) and experimental cross sections and supplied to the chemical kinetics equation / flow equation solver. Also, energy storage in plasma and combustion chemical reaction products is accounted for in the flow energy equation.

4.2 Governing equations

4.2.1 Quasi-one-dimensional flow equations

The present model uses the Lagrangian approach to describe the flow field in the repetitively pulsed discharge and in the afterglow. Specifically, the flow parameters, such as the axial coordinate x, velocity, temperature, pressure, and number density are calculated for a fluid particle with an initial axial coordinate x_{0p}, as functions of time elapsed, such as

$$T_p = T(x_{0p}, t), \tag{4.1}$$

where T_p is the fluid particle temperature and x_{0p} is its initial location (axial coordinate) at t=0, $x_{0p}=x_p(t=0)$. Note that this result can be also expressed as a function of the time-dependent particle coordinate, $x_p(t)$,

$$\frac{dx_p}{dt} = u_p, \tag{4.2}$$

where u_p is the particle velocity, for example

$$T_p = T(x_{0p}, x_p(t)), \tag{4.3}$$

In the present model, the calculations are performed for a fluid particle initially at $x_{0p} = 0$, i.e. at the entrance to the computational domain.

The one-dimensional flow equations [31] for a fluid particle include the motion equation,

$$\frac{du_p}{dt} = \frac{1}{u_p} \cdot \left\{ \frac{(\gamma - 1) \cdot M^2}{1 - M^2} \cdot \left[\frac{dQ}{dt} - \sum \left(\frac{h_i}{N_p} \cdot \frac{dn_i}{dt} \right) \right] \right\}, \tag{4.4}$$

the energy equation,

$$\frac{dT_p}{dt} = \frac{1}{c_{pm}} \cdot \left[\frac{dQ}{dt} - \sum \left(\frac{h_i}{N_p} \cdot \frac{dn_{ip}}{dt} \right) \right] (1 - \gamma M^2), \tag{4.5}$$

and the number density equation,

$$\frac{dN_p}{dt} = \left(\sum_i \frac{dn_{ip}}{dt} \right)_{chem} . \tag{4.6}$$

In Eqs. (4.4-4.6), t is time counted from the moment when the particle enters the computational domain, T_p and u_p are the temperature and the velocity of the particle, respectively, N_p is the number density in the particle, $\frac{dQ}{dt}$ is the power loading by the discharge, c_{pm} is the specific heat of the gas mixture at constant pressure, n_{ip} are the number densities of chemical and excited species, in molecules/m^3, and h_i are their enthalpies. The second term in the right-hand side of Eq. (4.5) describes the rate of energy storage in products of electron impact and chemical reactions. The right hand side of Eq. (4.6) describes the rate of the total number density change due to electron impact processes and chemical reactions. The expression for the specific heat at constant pressure is as follows,

$$C_{pm} = \frac{1}{N} \cdot \sum_i C_{pi} \cdot n_{ip} \ , \tag{4.7}$$

where C_{pi} is the mole-specific heat of species i, in $J / kmol \cdot K$. Note that c_{pm} in Eq. (4.4) is $c_{pm} = \frac{C_{pm}}{\mu_m}$ (i.e. the specific heat per unit mass). where

$$\mu_m = \frac{1}{N} \cdot \sum_i \mu_i \cdot n_{ip} \ , \tag{4.8}$$

is the molecular weight of the mixture. In Eq.(4.8), μ_i is the molecular weight for species i, in $kg / kmol$.

The power loading by the discharge in Eqs. (4.4) and (4.5) is calculated as follows:

$$\frac{dQ}{dt} = \frac{j \cdot E}{\rho_p}, \tag{4.9}$$

where j and E are the current density and the electric field in the discharge, respectively, and ρ_p is the density of the fluid particle, $\rho_p = \frac{N_p \mu_m}{N_A}$.

The pressure of the mixture is calculated from the equation of state for a perfect gas,

$$P = N_p \cdot k \cdot T, \tag{4.10}$$

where $k = \frac{R_0}{N_A}$ is the Boltzmann constant, R_0 is the universal gas constant and N_A is the Avogadro number.

In addition to equations (4.4-6) and (4.10), the total electric discharge power added to the flow, $\wp$ (in Watts) is calculated as follows:

$$\frac{d\wp}{\mathrm{dt}} = \dot{m} \cdot \frac{dQ}{dt} = \frac{j \cdot E}{\rho} \cdot \dot{m} = j \cdot E \cdot A \cdot u, \tag{4.11}$$

In Eq. (4.11), $\frac{dQ}{dt}$ (in $\frac{W}{kg}$) is given by Eq. (4.9), A is the cross sectional area of the flow, and $\dot{m}$ is the mass flow rate through the test section:

$$\dot{m} = \rho \cdot u \cdot A = const, \tag{4.12}$$

The initial value of the particle velocity, $u_{p0} = u_p(t = 0)$, is determined from the experimentally measured mass flow rate and pressure, at room temperature.

The discharge energy loading per molecule (in $\frac{eV}{molecule}$) is evaluated as follows,

$$Q_0 = \frac{Q}{e} \cdot \frac{\mu}{N_A} = \frac{1}{e} \cdot \frac{\wp}{\dot{m}} \cdot \frac{\mu}{N_A}, \tag{4.13}$$

where Q (in J/kg) is given by Eq. (4.9), $\wp$ is the discharge power in W, e is the elementary charge, and $\dot{m}$ is the mass flow rate. Eqs. (4.2), (4.4-6) and (4.10) provide axial coordinate, temperature, velocity, number density, and pressure of the fluid particle as functions of time, when the discharge current density and the electric field are known. The discharge current density is evaluated from the Ohm's law,

$$j = e \cdot n_e \cdot W_{dr}, \tag{4.14}$$

where n_e is the electron density and W_{dr} is the electron drift velocity. The electric field can be estimated from the experimentally measured discharge voltage, U,

$$E \approx \frac{U}{w}, \tag{4.15}$$

where w is the distance between the electrodes. However, this estimate does not take into account voltage drops in the near-electrode regions (sheaths), which can be quite significant [49]. Therefore, in the present model the effective electric field was considered to be an adjustable parameter, found by fitting the calculated pulsed discharge energy to the experimentally measured value (see Section 3.1.1).

In the present model, the pulse energy is calculated as follows,

$$Q_{pusle} = \int j(t) \cdot E(t) dt \cdot wA = \int I(t) \cdot U(t) dt, \tag{4.16}$$

where the time-dependent current density is found from Eq. (4.14), and the electric field pulse is approximated by a Gaussian shape function

$$U(t) = U_0 \exp\left[-\left(\frac{t - t_1}{t_2} \right)^2 \right]. \tag{4.17}$$

In Eq. (4.17), t_1 is the moment when the pulse voltage reaches maximum and t_2 is the pulse width, measured in the experiment. The time delay between the pulses, t_3 , is determined by the pulse repetition rate, $\nu=1/t_3$.

After the time-dependent fluid particle parameters are calculated, the steady-state flow field is determined by averaging the results over a group of particles with initial coordinates such as

$$0 \le x_{0p} \le u_{p0} t_3 , \tag{4.18}$$

For example, the steady-state flow temperature distribution is given as

$$\overline{T}(\overline{x}) = \frac{1}{u_{p0} t_3} \int_0^{u_{p0} t_3} T[x_{0p}, t] dx_{op} , \tag{4.19}$$

where

$$\overline{x} = \frac{1}{u_{p0} t_3} \int_0^{u_{p0} t_3} x_p[x_{0p}, t] dx_{op} \tag{4.20}$$

This approach converts the time-dependent fluid particle parameters in the repetitively pulsed discharge into the steady state flow parameters.

4.2.2 Species concentration equations

Species concentrations, n_i, can vary in time for two reasons, due to chemical reactions and due to the change of the mixture number density, which is described by the two terms in the right hand side of the following equation,

$$\left(\frac{dn_j}{dt} \right)_{total} = \left(\frac{dn_j}{dt} \right)_{chem} + n_i \cdot \frac{1}{N} \cdot \frac{dN}{dt} . \tag{4.21}$$

Chemical reactions considered by the present model are written in the following form [1]:

$$\sum_{i(react)} a_i \cdot A_i \overset{k_f}{\underset{k_r}{\Leftrightarrow}} \sum_{j(prod)} b_j \cdot B_j \ , \tag{4.22}$$

where A_i and B_i are the reactants and the products, respectively, and a_i and b_i are the corresponding stoichiometric coefficients.

The reaction rate per unit stoichiometric coefficient can be written as

$$R_l = k_f \cdot \prod_{\substack{i \\ (reactants)}} n_i^{a_i} - k_r \cdot \prod_{\substack{j \\ (products)}} n_j^{b_j} \ , \tag{4.23}$$

where k_f is the rate coefficient for the forward reaction, and k_r is the rate coefficient for the reverse reaction. The rate of species concentration change in a reaction is expressed as

$$\left(\frac{dn_j}{dt} \right)_{chem} = \left(b_j - a_j \right) \cdot R_l \, , \tag{4.24}$$

where b_j and a_j are the stoichiometric coefficients for species j, and n_j is its number density.

The total rate of the species concentration change due to all chemical reactions is

$$\left(\frac{dn_j}{dt} \right)_{chem} = \sum_{reactions} R_i \left(b_{ij} - a_{ij} \right) \tag{4.25}$$

The rate coefficients of thermal chemical reactions (i.e. reactions without participation of electrons or excited species) are related as follows:

$$\frac{k_f}{k_r} = \exp\left(\frac{-\sum_{react} G_i \cdot a_i + \sum_{prod} G_j \cdot b_j}{R_0 T} \right), \tag{4.26}$$

where G_i and G_j are the Gibbs free energies of the reactants and the products, respectively. For these reactions, the rate coefficients k_f and k_r are given in the Arrhenius form, such as

$$k_f = A \cdot T^n \cdot \exp\left(-\frac{E_A}{RT}\right), \tag{4.27}$$

where A and E_A are the pre-exponential factor and the activation energy, respectively. In the modeling calculations, only one of the two experimentally measured rate coefficients, k_f or k_r, given by Eq. (4.27) is used, and the other one is calculated using Eq. (4.26).

Rate coefficients of pressure-dependent reactions in the fall-off region were calculated as follows [50],

$$k = \frac{P_r k_\infty}{1 + P_r}, \tag{4.28}$$

where

$$P_r = \frac{k_o[M]}{k_\infty} \tag{4.29}$$

is the reduced pressure, $k_o\,[\frac{cm^6}{s}]$ is the forward reaction rate coefficient of a three-body reaction,

$$A + B + M \leftrightarrow AB + M, \tag{4.30}$$

(the low-pressure limit), $k_\infty\,[\frac{cm^3}{s}]$ is the forward reaction rate coefficient of a two-body reaction,

$$A + B \leftrightarrow AB, \tag{4.31}$$

(the high-pressure limit), and [M] is the number density in cm^{-3}. At low reduced pressures, when $P_r << 1$, the rate coefficient asymptotically approaches the low-pressure limit,

$k \to P_r k_\infty = k_0[M]$, i.e. it is proportional to the number density. On the other hand, at high reduced pressures, the rate coefficient approaches the high-pressure limit, $k \to k_\infty$, i.e. it becomes independent of the number density. This description of pressure dependence of reaction rate coefficients is very important for some hydrocarbon radical recombination reactions, such as

$$CH_3 + CH_3(+M) \leftrightarrow C_2H_6(+M)\,. \tag{4.32}$$

Thermochemical data of chemical species used in Eqs. (4.26) and (4.27), such as specific heats, enthalpies, entropies, and Gibbs free energies are calculated using polynomial fits from the CHEMKIN thermochemical database

$$C_{P,i} = C_{V,i} + R\,, \tag{4.33}$$

$$H_i(T) = \int_0^T C_{P,i}(T)dT\,, \tag{4.34}$$

$$S_i(T) = \int_0^T \frac{C_{P,i}(T)}{T}dT\,, \tag{4.35}$$

$$G_i(T) = H_i(T) - T \cdot S_i(T)\,, \tag{4.36}$$

After the time-dependent species concentrations in a fluid particle are calculated from Eq. (4.6), species concentrations in the steady-state flow are evaluated as discussed in the previous section,

$$\overline{n}_i(\overline{x}) = \frac{1}{u_{p0}t_3}\int_0^{u_{p0}t_3} n_i[x_{0p}, t]dx_{op}\,, \tag{4.37}$$

where $\overline{x}$ is calculated by Eq. (4.20)

4.2.3 Boltzmann equation

In the present model, rate coefficients of electron impact processes, such as

$$e + A \rightarrow e + A(excited), \tag{4.38}$$

are calculated using experimental cross sections for these processes, as functions of the electron energy, $\sigma = \sigma(\varepsilon)$. To calculate the rate coefficients, the cross sections are integrated over *f(ε)*, the electron energy distribution function (EEDF). The EEDF is calculated by solving the two-term expansion Boltzmann equation for plasma electrons.

The steady-state Boltzmann equation used in the present model is as follows [51],

$$0 = I_E + I_{e-M} + I_{in}, \tag{4.39}$$

where I_E is the plasma electron heating term by the applied electric field, I_{e-M} is the elastic collision term, and I_{in} is the inelastic collision term.

The electron heating term can be written as [51]

$$I_E = \frac{1}{3} \cdot \left(\frac{E}{N} \right)^2 \cdot N \frac{\partial}{\partial \varepsilon} \left(\frac{\varepsilon}{Q_T(\varepsilon)} \frac{\partial f}{\partial \varepsilon} \right), \tag{4.40}$$

where $\frac{E}{N}$ is the reduced electric field, ε is the electron energy, and $Q_T(\varepsilon)$ is the effective transport cross section as a function of the electron energy,

$$Q_T(\varepsilon) = \frac{1}{N} \sum_i Q_{T_i}(\varepsilon) \cdot n_i \ . \tag{4.41}$$

Here $Q_{T_i}(\varepsilon)$ are the transport cross sections for individual species in the mixture (molecules and atoms), and *f(ε)* is the exponential part of the EEDF, normalized as follows:

$$\int \sqrt{\varepsilon} \cdot f(\varepsilon) \cdot d\varepsilon = 1. \tag{4.42}$$

The elastic collision term, I_{e-M}, represents electron energy loss due to elastic (momentum transfer) collisions between electrons and heavy species. This term is written as follows [51],

$$I_{e-M} = \sum_i \frac{2m}{M_i} \frac{\partial}{\partial \varepsilon} \left[\varepsilon^2 \cdot Q_{T_i}(\varepsilon) \cdot N \left(f + \frac{kT}{e} \frac{\partial f}{\partial \varepsilon} \right) \right], \tag{4.43}$$

where m is the mass of the electron, and M_i are the masses of the heavy species.

The final term in the Boltzmann equation, I_{in}, represents electron energy loss due to rotational, vibrational, electronic excitation, and ionization of heavy species in collisions with electrons. In the present model, vibrational excitation processes are neglected since they are not expected to play an important role in the overall electron energy balance at high reduced electric field values for the present experimental conditions, E/N>10^{-15} Vcm^2=100 Td. Also, the process of ionization by electron impact, such as

$$e + A \rightarrow e + A^+ + e, \tag{4.44}$$

is treated in the same way as electronic excitation, i.e. it is assumed that the second electron produced by ionization does not affect the shape of the EEDF. Therefore, the inelastic collision term is written as follows:

$$I_{in} = I_{rot} + I_{el-ion}. \tag{4.45}$$

The rotational collision term accounts for rotational excitation of molecules by electron impact. This term can be written as follows [52],

$$I_{rot} = \sum_i B_i \frac{\partial}{\partial \varepsilon} \left[\varepsilon \cdot Q_{T_i}(\varepsilon) \cdot N \cdot \left(f + \frac{kT}{e} \frac{\partial f}{\partial \varepsilon} \right) \right], \tag{4.46}$$

where B is the rotational constant of a molecule.

The electronic excitation term describes the electron energy loss due to the energy transfer that excites a molecule from a ground state to an excited electronic state. A schematic of this process is shown in Fig. 4.1. In an electron impact process, a high-energy electron with energy ε, represented in Fig. 4.1 by point 2, collides with a molecule and excites it to an excited state with energy ε^*. During this process, the electron energy decreases by the amount of ε^* represented by the transition from point 2 to point 1 in Fig. 4.1. This would reduce the number of electrons with initial energy ε. However, as can also be seen from Fig. 4.1, a higher-energy electron with an initial energy $\varepsilon + \varepsilon^*$, shown as point 3 in Fig. 4.1, will transfer the same amount of energy, ε^*, to the molecule during the same excitation process and will have the final energy of ε, which is shown as a transition from point 3 to point 2 in Fig. 4.1. As a result, the general expression for the electronic excitation term can be written as

$$I_{el-ion} = N\sum_k \left\{Q_k\left(\varepsilon+\varepsilon^*\right)\cdot f\left(\varepsilon+\varepsilon^*\right)\cdot\left(\varepsilon+\varepsilon^*\right) - Q_k(\varepsilon)\cdot f(\varepsilon)\cdot\varepsilon\right\}, \tag{4.47}$$

where $Q_k(\varepsilon)$ are the cross sections of electronic excitation processes.

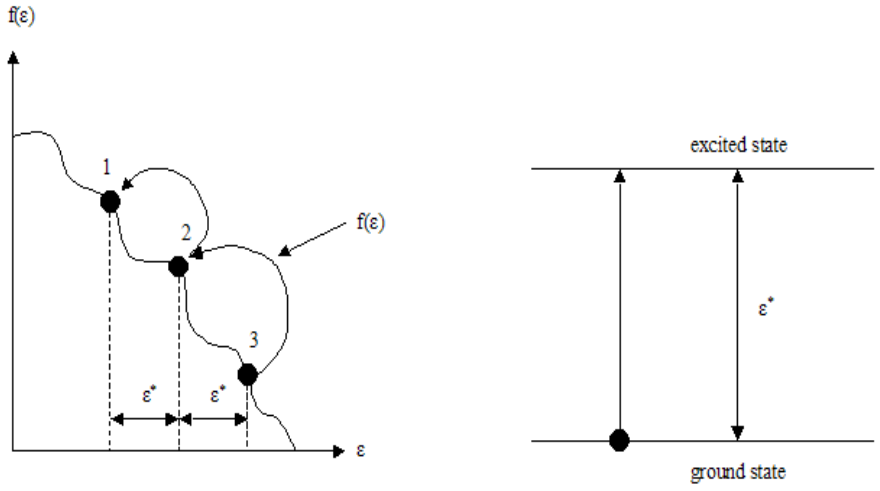

Figure 4.1: Schematic of an electronic excitation process.

Experimental cross section data for vibrational, rotational, and electronic excitation of each species are provided as inputs to the Boltzmann equation solver code [52, 53]. As a result, the Boltzmann equation given by Eqs. (4.38 - 4.47) is the second order ordinary differential equation for the EEDF, *f(ε)*. Using the experimental cross sections as inputs, the Boltzmann solver subroutine solves the equation iteratively and calculates *f(ε)*. The code then calculates the rate coefficients of electron impact processes,

$$k = \left(\frac{2 \cdot e}{m_e}\right)^{\frac{1}{2}} \int \sigma(\varepsilon) \cdot \varepsilon \cdot f(\varepsilon) d\varepsilon \,. \tag{4.48}$$

Figure 4.2 shows the experimental cross section of electron impact excitation of the $C^3\Pi_u$ electronic state of N_2 [52], which is used in the current model. Figure 4.3 plots the rate coefficients of electron impact excitation reaction, $N_2(X^1\Sigma_g^+) + e \rightarrow N_2(C^3\Pi_u) + e$, calculated by the Boltzmann solver using Eq. (4.48) and the cross section shown in Fig. 4.2. In Figure 4.3, the electron impact rate coefficient is plotted as a function of the reduced electric field, E/N.

Electron drift velocity, W_{dr}, and electron temperature, T_e, are calculated from the EEDF as follows [51]:

$$W_{dr} = -\frac{eE}{3N} \cdot \left(\frac{2}{m_e}\right)^{1/2} \int \frac{\varepsilon}{\sigma(\varepsilon)} \frac{d}{d\varepsilon}\left[f(\varepsilon)\right] d\varepsilon \,, \tag{4.49}$$

$$T_e = -\frac{1}{k} \cdot \left\{ \frac{\int \frac{\varepsilon}{\sigma(\varepsilon)} \left[f(\varepsilon)\right] d\varepsilon}{\int \frac{\varepsilon}{\sigma(\varepsilon)} \frac{d}{d\varepsilon}\left[f(\varepsilon)\right] d\varepsilon} \right\}. \tag{4.50}$$

Figures 4.4 and 4.5 show the dependence of the drift velocity and the electron temperature in air on the reduced electric field.

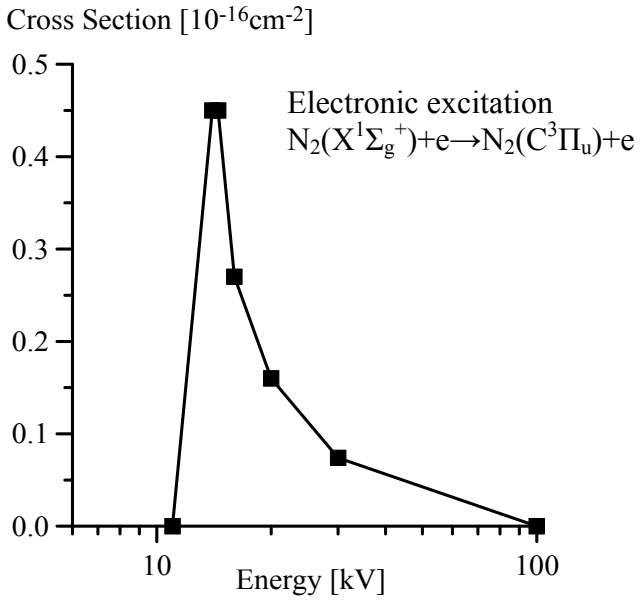

Figure 4.2: Experimental cross section of electronic excitation of $N_2(C^3\Pi_u)$ state.

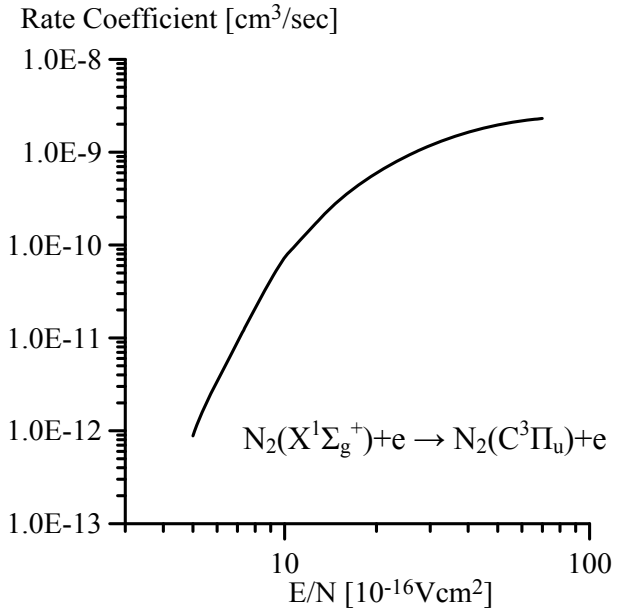

Figure 4.3: Rate coefficient of electron impact excitation process $N_2(X^1\Sigma_g^+ \rightarrow C^3\Pi_u)$ in air, calculated from the cross section plotted in Fig. 4.2.

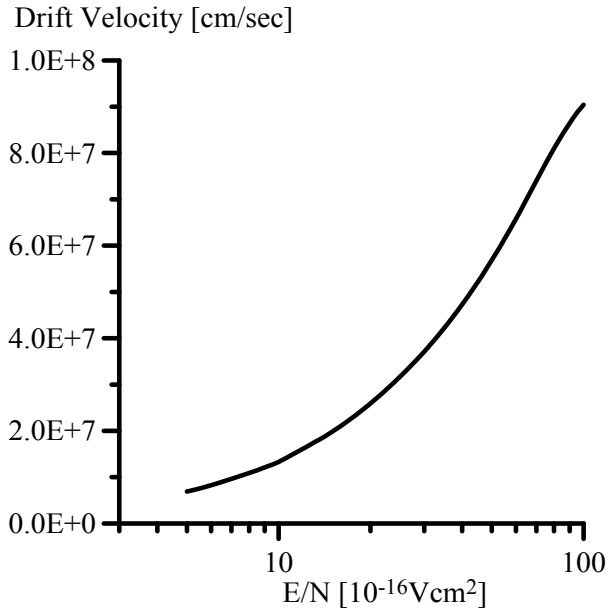

Figure 4.4: Electron drift velocity in air vs. the reduced electric field

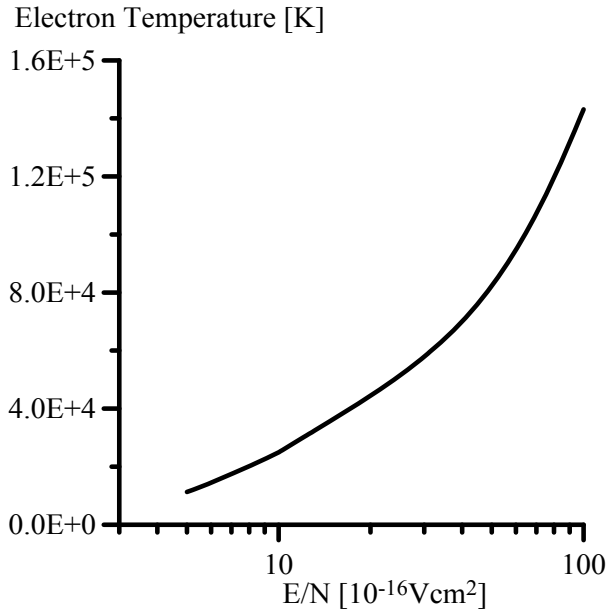

Figure 4.5: Electron temperature in air vs. the reduced electric field

In the modeling calculations, the Boltzmann solver is called in the beginning of the code execution for an array of E/N values. The calculated values of electron temperature, electron drift velocity, and electron impact rate coefficients are stored and later used as functions of E/N in the repetitively pulsed discharge, using linear interpolation.

In the present model, the unsteady term in the Boltzmann equation [51], $N\left(\frac{m_e\varepsilon}{2}\right)^{1/2}\frac{\partial}{\partial t}[f(\varepsilon)]$, is not taken into account. This is justified for time scales much longer than the time between electron-neutral collisions, $\tau_{coll} \sim 1/N\upsilon\sigma$ [28], where $\upsilon \sim \sqrt{\frac{kT_e}{m_e}} \sim 10^8$ cm/s (at T_e=8·10^4 K, see Fig. 4.5) is the electron thermal velocity and $\sigma \sim 10^{-15}$ cm^2 is the transport collision cross section. At T=300 K, P=0.1 atm, and N=2.45·10^{18}cm^{-3}, $\tau_{coll} \sim 10^{-11}$ sec. For discharge pulse durations typical for the present experiment, t_2~ 5-30 nsec, $t_2/\tau_{coll} \sim 10^3 >> 1$, which suggests that during the discharge pulse, the EEDF will have enough time to reach the quasi-steady-state, and the unsteady term in the Boltzmann equation would not affect the solution. Indeed, Figure 4.6 compares the results of the Boltzmann equation solution with and without the unsteady term, for E/N =500 Td, T=300 K, and P=0.1 atm [47]. It can be seen that for t>10^{-9} sec, the two solutions become very close to each other.

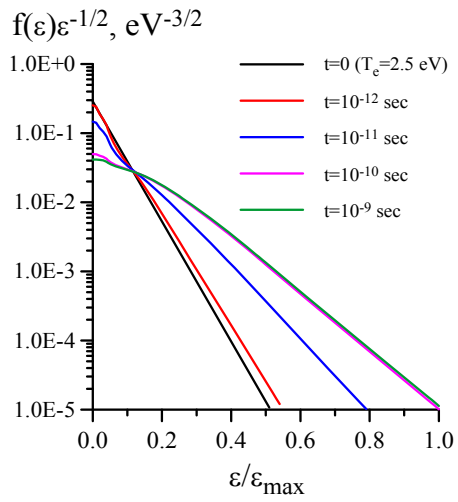

Figure 4.6 Time-resolved electron energy distribution function (exponential part) calculated with and without the unsteady term in the Boltzmann equation. Air, P=0.1 atm, T=300 K, E/N=500 Td, εmax=50 eV.

4.3 Kinetic processes and rates

Kinetic processes used in the present model can be separated into two types: (i) electron impact processes and electron-ion-molecule reactions, and (ii) neutral species reactions. The kinetic model of electron impact processes, electron-ion-molecule reactions, and neutral species reactions in an air plasma is based on Ref. [54]. The neutral species reaction model in hydrocarbon-air mixtures is based on GRI 3.0 combustion mechanism [55].

4.3.1 Electron impact processes in air plasma

Electron impact processes include reactions in which an electron collides with a molecule or an atom, and the energy transferred during the collision excites the target species to a higher energy state or breaks it apart. Such processes include rotational, vibrational, and electronic excitation, as well as ionization, dissociation, and dissociative

attachment. In the present kinetic model, vibrational excitation collisions are not considered. The model incorporates excitation of $A^3\Sigma_u^+, B^3\Pi_g, a^1\Sigma_u^-$ and $C^3\Pi_u$ levels of N_2, $a^1\Delta_g$, $b^1\Sigma_g^+$, $A^3\Sigma_u^+$, $A^3\Delta_u$ and $c^1\Sigma_u^-$ of O_2 (the latter three states of O_2 are collectively represented as a single level O_2(c)), and the ^1D state of O atom. The list of electron impact excitation processes is summarized in Table 4.1. Their rates are calculated by the Boltzmann solver, as discussed in Section 4.2, which is indicated by a symbol σ in Table 4.1.

Reaction	Rate coefficient (cm^3/s)
$N_2 + e^- = N_2(A) + e^-$	σ
$N_2 + e^- = N_2(B) + e^-$	σ
$N_2 + e^- = N_2(C) + e^-$	σ
$N_2 + e^- = N_2(a) + e^-$	σ
$N_2 + e^- = N + N + e^-$	σ
$O_2 + e^- = O_2(a) + e^-$	σ
$O_2 + e^- = O_2(b) + e^-$	σ
$O_2 + e^- = O_2(c) + e^-$	σ
$O_2 + e^- = O + O + e^-$	σ
$O_2 + e^- = O + O(D) + e^-$	σ
$N_2 + e^- = N_2^+ + e- + e^-$	σ
$O_2 + e- = O_2^+ + e- + e-$	σ
$O_2 + e- = O + O^+ + e- + e-$	σ
$O_2 + e- = O + O^-$	σ

Table 4.1: Reactions and rate coefficients of electron impact processes in air plasma

Figure 4.7 shows energy balance in an electric discharge, i.e. energy fractions into different electron impact processes, as functions of the reduced electric field, E/N. These results are obtained by using the Boltzmann solver described in Section 4.2. The energy fractions are calculated as follows:

$$\alpha_i = \frac{k_i \varepsilon_i N n_e}{jE} = \frac{k_i \frac{\varepsilon_i}{e} N}{W_{dr} E} \tag{4.51}$$

where k_i is the electron impact reaction rate coefficient, ε_i is the excited level energy, N is the number density, n_e is the electron density, and W_{dr} is the drift velocity. As can be seen from Fig. 4.7, at E/N>20·10^{-16} V·cm^2, a relatively small fraction of discharge power goes to vibrational excitation of nitrogen (less than 10%). This justifies neglecting vibrational energy transfer and reactions of vibrationally excited molecules in the present work.

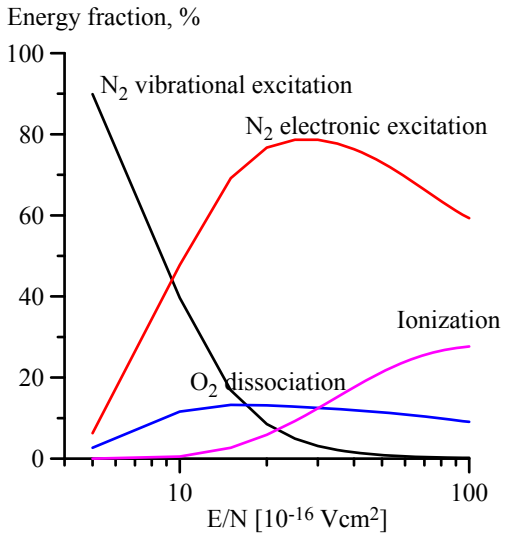

Figure 4.7: Discharge energy balance in air vs. reduced electric field (E/N).

4.3.2 Electron removal processes in air plasma

Kinetic processes affecting electron removal include dissociative recombination, three-body electron attachment, as well as electron detachment processes, summarized in Table 4.2.

In low-temperature air plasmas, the dominant electron removal process is the three-body electron attachment to oxygen,

$$e + O_2 + O_2 \rightarrow O_2^- + O_2 \ , \tag{4.52}$$

$$e + O_2 + N_2 \rightarrow O_2^- + N_2 \ . \tag{4.53}$$

Other electron attachment and detachment processes, including electron detachment from O^- and O_2^- ions in collision with excited molecules and atoms, and their reaction rates are given in Table 4.2, as functions of the electron temperature,

$$k = A \cdot T_e^n \ . \tag{4.54}$$

4.3.3 Electronically excited species reactions in air plasma

Quenching reactions of electronically excited species, $N_2(A^3\Sigma_u^+)$, $N_2(B^3\Pi_g)$, $N_2(a^1\Sigma_u^-)$, $N_2(C^3\Pi_u)$, $O_2(a^1\Delta_g)$, $O_2(b^1\Sigma_g^+)$, O_2(c), and $O(^1D)$, and their rate coefficients at room temperature are listed in Table 4.3. The main effect of these processes on chemical composition of air plasma is oxygen dissociation and O atom generation. Fig. 4.7 shows that at E/N =100-300 Td, up to 40-80% of the discharge power goes to electronic excitation of nitrogen, This demonstrates that quenching of electronically excited nitrogen molecules in collision with O_2 molecules, resulting in O_2 dissociation, could be a major dissociation channel. Rate coefficients of reactions in Table 4.3 are taken from Ref. [54].

4.3.4 Ion-molecule reactions in air plasma

Ion-molecule reactions involving ions formed during electron impact excitation processes, N_2^+, O_2^+, O^+, and ions formed during electron attachment processes, O^-, O_2^-, as well as the NO^+ ion, are listed in Table 4.4. Rate coefficients of these reactions at room temperature are also taken from Ref. [54]. In the present work, reactions of complex cluster ions , such as N_4^+, O_4^+, O_3^+, O_3^- , O_4^-, NO_2^-, etc. are neglected.

	Reaction	Rate coefficient A (cm^3/s or cm^6/s)	n
Electron attachment	$O_2 + O_2 + e^- = O_2^- + O_2$	4.20E-27	-1.00
	$O_2 + N_2 + e^- = O_2^- + N_2$	9.63E-25	-2.00
	$O + O_2 + e^- = O^- + O_2$	9.99E-32	0
	$O + O_2 + e^- = O_2^- + O$	9.99E-32	0
	$O_3 + e^- = O_2^- + O$	1.00E-09	0
	$O_3 + e^- = O^- + O_2$	1.00E-11	0
Electron Detachment	$O_2^- + N_2 = O_2 + N_2 + e^-$	1.13E-19	0
	$O_2^- + O_2 = O_2 + O_2 + e^-$	2.18E-18	0
	$O_2^- + O_2(a) = O_2 + O_2 + e^-$	2.00E-10	0
	$O_2^- + O_2(b) = O_2 + O_2 + e^-$	3.60E-10	0
	$O_2^- + N_2(A) = O_2 + N_2 + e^-$	2.10E-9	0
	$O_2^- + N_2(B) = O_2 + N_2 + e^-$	2.50E-9	0
	$O^- + O_2(a) = O_3 + e^-$	3.00E-10	0
	$O^- + O_2(b) = O + O_2 + e^-$	6.90E-10	0
	$O^- + N_2(A) = O + N_2 + e^-$	2.20E-09	0
	$O^- + N_2(B) = O + N_2 + e^-$	1.90E-09	0
	$O_2^- + O = O_3 + e^-$	1.50E-10	0
	$O^- + O = O_2 + e^-$	5.00E-10	0
	$O^- + N = NO + e^-$	2.60E-10	0
	$O^- + O_2 = O_3 + e^-$	5.00E-15	0
Electron-ion recombination	$N_2^+ + e^- = N + N$	4.85E-06	-0.50
	$O_2^+ + e^- = O + O$	5.99E-05	-1.00
	$NO^+ + e^- = N + O$	2.08E-03	-1.50
Ion-ion recombination	$O^+ + O_2^- = O_2 + O$	2.00E-7	0
	$O^+ + O^- = O + O$	2.00E-7	0
	$O_2^+ + O_2^- = O_2 + O_2$	2.00E-7	0
	$O_2^+ + O^- = O_2 + O$	2.00E-7	0
	$N_2^+ + O_2^- = N_2 + O_2$	2.00E-7	0
	$N_2^+ + O^- = N_2 + O$	2.00E-7	0
	$NO^+ + O_2^- = NO + O_2$	2.00E-7	0
	$NO^+ + O^- = NO + O$	2.00E-7	0

Table 4.2: Reactions and rate coefficients of electron removal processes

Reaction	Rate coefficient A (cm^3/s or cm^6/s)
$N_2(A) + O_2 = N_2 + O + O$	2.54E-12
$N_2(A) + O_2 = N_2 + O_2(a)$	1.29E-12
$N_2(A) + O = N_2 + O$	2.09E-11
$N_2(A) + O = NO + N$	6.99E-12
$N_2(A) + O_3 = N_2 + O + O_2$	3.39E-11
$N_2(A) + N_2 = N_2 + N_2$	3.01E-18
$N_2(A) + N_2(A) = N_2 + N_2(C)$	1.99E-12
$N_2(A) + NO = N_2 + NO$	6.99E-11
$N_2(B) + N_2 = N_2(A) + N_2$	5.00E-11
$N_2(B) + O_2 = N_2 + O + O$	3.01E-10
$N_2(B) + NO = N_2(A) + NO$	2.39E-10
$N_2(C) + O_2 = N_2 + O + O$	3.01E-10
$N_2(C) + N_2 = N_2(a) + N_2$	1.00E-11
$N_2(a) + N_2 = N_2(B) + N_2$	1.00E-13
$N_2(a) + O_2 = N_2 + O + O$	2.81E-11
$N_2(a) + NO = N_2 + N + O$	3.60E-10
$O_2(a) + N_2 = N_2 + O_2$	3.01E-21
$O_2(a) + O_2 = O_2 + O_2$	2.19E-18
$O_2(a) + O = O_2 + O$	6.99E-16
$O_2(a) + NO = O_2 + NO$	2.51E-11
$O_2(a) + O_3 = O_2 + O_2 + O$	5.35E-15
$O_2(b) + O_3 = O + O_2 + O_2$	1.79E-11
$O_2(b) + O = O_2(a) + O$	8.00E-14
$O_2(b) + O_2 = O_2(a) + O_2$	1.69E-16
$O_2(b) + N_2 = N_2 + O_2(a)$	2.13E-15
$O_2(b) + O = O_2 + O(D)$	2.81E-17
$O_2(b) + NO = O_2(a) + NO$	4.00E-14
$O_2(c) + M = O_2(b) + M$	3.01E-13
$O_2(c) + O = O_2(b) + O(D)$	9.00E-12
$O(D) + N_2 = O + N_2$	3.20E-11
$O(D) + O = O + O$	8.00E-12
$O(D) + O_2 = O + O_2(b)$	2.04E-11
$O(D) + O_2 = O + O_2(a)$	1.30E-12
$O(D) + O_2 = O + O_2$	3.84E-12
$O(D) + O_3 = O_2 + O$	1.20E-10
$O(D) + O_3 = O_2 + O_2$	1.20E-10

Table 4.3: Electronically excited species reactions and rate coefficients

Reaction	Rate coefficient A (cm^3/s or cm^6/s)
$N^+ + O + M = NO^+ + M$	9.98E-30
$N^+ + N + M = N_2^+ + M$	9.98E-30
$O^+ + N_2 + M = NO^+ + N + M$	6.00E-29
$O^+ + O + M = O_2^+ + M$	9.98E-30
$O^+ + N + M = NO^+ + M$	9.98E-30
$N^+ + O_2 = O_2^+ + N$	2.81E-10
$N^+ + O_2 = NO^+ + O$	2.51E-10
$N^+ + O_2 = O^+ + NO$	2.81E-11
$N^+ + O = N + O^+$	1.00E-12
$N^+ + O_3 = NO^+ + O_2$	5.00E-10
$N^+ + NO = N + NO^+$	8.00E-10
$N^+ + NO = N_2^+ + O$	3.00E-12
$N^+ + NO = O^+ + N_2$	1.00E-12
$O^+ + N_2 = NO^+ + N$	1.18E-12
$O^+ + O_2 = O_2^+ + O$	1.98E-11
$O^+ + O_3 = O_2^+ + O_2$	1.00E-12
$O^+ + NO = NO^+ + O$	2.40E-11
$O^+ + NO = O_2^+ + N$	3.00E-12
$O^+ + N = N^+ + O$	1.31E-10
$N_2^+ + O = NO^+ + N$	1.30E-10
$N_2^+ + O = O^+ + N_2$	1.00E-11
$N_2^+ + O_3 = O_2^+ + O + N_2$	1.00E-10
$N_2^+ + N = N^+ + N_2$	7.19E-13
$N_2^+ + NO = NO^+ + N_2$	3.30E-10
$O_2^+ + N_2 = NO^+ + NO$	1.00E-17
$O_2^+ + N = NO^+ + O$	1.20E-10
$O_2^+ + NO = NO^+ + O_2$	4.40E-10
$O_2^- + O = O_2 + O^-$	3.30E-10
$O^- + O_2(a) = O_2^- + O$	1.00E-10

Table 4.4: Ion-molecule reactions and rate coefficients

4.3.5 Neutral species reactions in air plasma

Neutral species reactions and their rate coefficients at room temperature are listed in Table 4.5. The most important neutral species reactions are O atom reactions with O_2 and O_3 which cause O atom decay in the afterglow plasma.

Reaction	Rate coefficient A (cm^3/s or cm^6/s)
$O + O_2 + M = O_3 + M$	5.90E-34
$O + O_3 = O_2 + O_2$	8.30E-15
$O + O + N_2 = O_2 + N_2$	4.69E-33
$O + O + O_2 = O_2 + O_2$	9.92E-33
$N + N + M = N_2 + M$	1.38E-33

Table 4.5: Neutral species reactions and rate coefficients

Summarizing, the air plasma model incorporates processes listed in Tables 4.1-4.5. Note that even in air plasmas, the number of ion species and their reactions can be quite significant. In hydrocarbon-air plasmas, the number of ion species and their reactions, including various chemi-ions, becomes extremely large. In addition, rate coefficients and their temperature dependence for many of these reactions are known with significant uncertainty or not known at all. In this situation, incorporating all these reactions into the kinetic model does not seem feasible. Therefore, in the present work, a different approach has been used. In this approach, the peak electron density during the discharge pulse was considered to be an adjustable parameter, varied in time in the same way as the pulse voltage,

$$n_e = (n_e)_{\max} \exp\left[-\left(\frac{t - t_1}{t_2}\right)^2\right] \tag{4.55}$$

(compared with Eq. (4.17)).

In this case, the peak electron density is varied to fit the calculated pulse energy (see Eq. (4.16)) to the experimental pulse energy (see Section 3.1.1). In this approach, all charged species reactions, including ionization, recombination, attachment, detachment, and ion conversion, were left out. This approach was validated by comparing the "full" model (with charged species reactions) and the "simplified" model (without charged species reactions) predictions with the experimental measurements of O atom density a pulsed air plasma (see Chapter 5). This approach was also used in modeling of hydrocarbon-air plasmas.

4.3.6 Plasma chemical reactions of hydrocarbon fuel species

Adding hydrocarbons to the air plasma results in (i) electron impact dissociation of hydrocarbons, and (ii) dissociation of hydrocarbon molecules in collisions with electronically excited nitrogen molecules. In addition to O atoms produced in the air plasma, these processes generate H atoms as well as CH_3 and C_2H_3 radicals. These processes are listed in Table 4.6. The experimental cross section of electron impact dissociation of methane, $CH_4 + e \rightarrow CH_3 + H + e$, is taken from Ref. [56]. Cross sections of electron impact dissociation of C_2H_4 into C_2H_3+H, C_2H_2+H_2, and C_2H+H_2+H were calculated in Ref [57]. Finally, rate coefficients of electronically excited nitrogen molecule quenching in collisions with CH_4 and C_2H_4 were taken from Refs. [44-46, 58-61].

Note that the quantum yield of H atoms, i.e. the probability of methane dissociation into H+CH_3 in quenching collisions with N_2^* has been measured only for quenching of $N_2(a^1\Sigma_u^-)$ state, ≈0.7 [60]. For $N_2(A^3\Sigma_u^+)$+C_2H_4 quenching, the H atom

quantum yield was estimated to be 0.2-0.3 [44]. Therefore the actual rates of CH_4 and C_2H_4 dissociation in collision with N_2^* are only known with some uncertainty. In the present work, we assume 100% quantum yield of H atoms in these reactions.

Reaction	Rate coefficient (cm^3/s)	Ref
$CH_4 + e- = CH_3 + H + e-$	σ	56
$C_2H_4 + e- = C_2H_3 + H + e-$	σ	57
$C_2H_4 + e- = C_2H_2 + H_2 + e-$	σ	57
$C_2H_4 + e- = C_2H + H_2 + H + e-$	σ	57
$N_2 (A) + CH_4 = N_2 + CH_3 + H$	0.268e-14	58
$N_2 (B) + CH_4 = N_2 + CH_3 + H$	0.24e-10	59
$N_2 (C) + CH_4 = N_2 + CH_3 + H$	0.40e-10	60
$N_2 (a) + CH_4 = N_2 + CH_3 + H$	0.24e-10	61
$N_2 (A) + C_2H_4 = N_2 + C_2H_3 + H$	0.97e-11	44
$N_2 (B) + C_2H_4 = N_2 + C_2H_3 + H$	0.3e-10	44
$N_2 (C) + C_2H_4 = N_2 + C_2H_3 + H$	0.3e-10	44
$N_2 (a) + C_2H_4 = N_2 + C_2H_3 + H$	0.4e-10	45
$N_2 (A) + C_2H_2 = N_2 + C_2H + H$	0.14e-10	44

Table 4.6: Reactions and rate coefficients of plasma chemical reactions in hydrocarbon-air mixtures.

4.3.7 Neutral species reactions in hydrocarbon-air mixtures

Chemical reactions among unexcited neutral species in hydrocarbon-air mixtures and their rate coefficients in the Arrhenius form are taken from the GRI-Mech 3.0 reaction mechanism [55]. The reverse rate coefficients are calculated from thermochemical equilibrium (see Eq. (4.26)). Full list of GRI-MECH 3.0 reactions and their rate coefficients is given in Appendix C.

4.4 Description of the computer code

The computer code based on the kinetic model discussed in Sections 4.2-4.3 consists of (i) the main driver code, which reads and processes input data, sets up the flow equations and the chemical kinetics equations, and prints out the results, (ii) stiff ordinary differential equation solver LSODE [62], and (iii) Boltzmann equation solver. The main driver needs three input files: a list of chemical and plasma reactions and reaction rate coefficients "mixture.rea", a thermochemical data file "mixture.trm", and an initial condition data file, "mixture.inp". The flow chart of the code algorithm is shown in Fig. 4.8.

Table 4.7 shows a list of typical initial flow and pulsed discharge conditions used in the present calculations. In the input data file, the printout frequency parameter Stlog determines the distance between two successive printouts of the results,

$$Stlog = \log_{10} \frac{x_{i+1}}{x_i}, \tag{4.56}$$

where x is the axial coordinate of a fluid particle along the test section, as a function of time.

The main driver also reads the list of chemical reactions and their rate coefficients from the file "mixture.rea". The reaction rate coefficients are given in the Arrhenius form. Rate coefficients of electron impact processes in this file are set to zero. The main driver calls the Boltzmann solver which calculates these rates. Species thermochemical data, such as specific heats ($C_{P,i}$), entropies (S_i), enthalpies (H_i), and Gibbs free energies (G_i) are calculated by the code based on polynomial curve fit coefficients from the CHEMKIN thermodynamics database, stored in the file "mixture.trm". The code

calculates these thermodynamic properties as functions of temperature and saves them in a file "methane.tbl" in the JANAF table [63] format.

After that, the main driver calls a subroutine RATECO which analyzes the list of reactants and products for every chemical reaction and identifies and "tags" electron impact reactions for which the rates will be calculated by the Boltzmann solver. After return to the main driver, the code sets up timing parameters for high-voltage pulses (i.e. the moments of time when the pulses are initiated).

After this, the code assigns initial values to the flow parameters, x, n_i, T, N, and P, and calls the ordinary differential equation solver LSODE. LSODE integrates the system of equations until it reaches the next result output point x_{out}, after which it returns to the main code. At the output point, the flow parameters are saved in the file "methane.dat". After that, the main code either calls LSODE again (if $x < x_{end}$), or stops the calculations (when $x = x_{end}$) (see Fig. 4.8).

On every time step, the LSODE solver calls subroutine DIFFUN, which calculates the right-hand-sides of the equations, integrated by the LSODE solver, Eqs. (4.2), (4.4-4.6), (4.9-4.11). DIFFUN also calculates the reverse reaction rates according to Eq. (4.26).

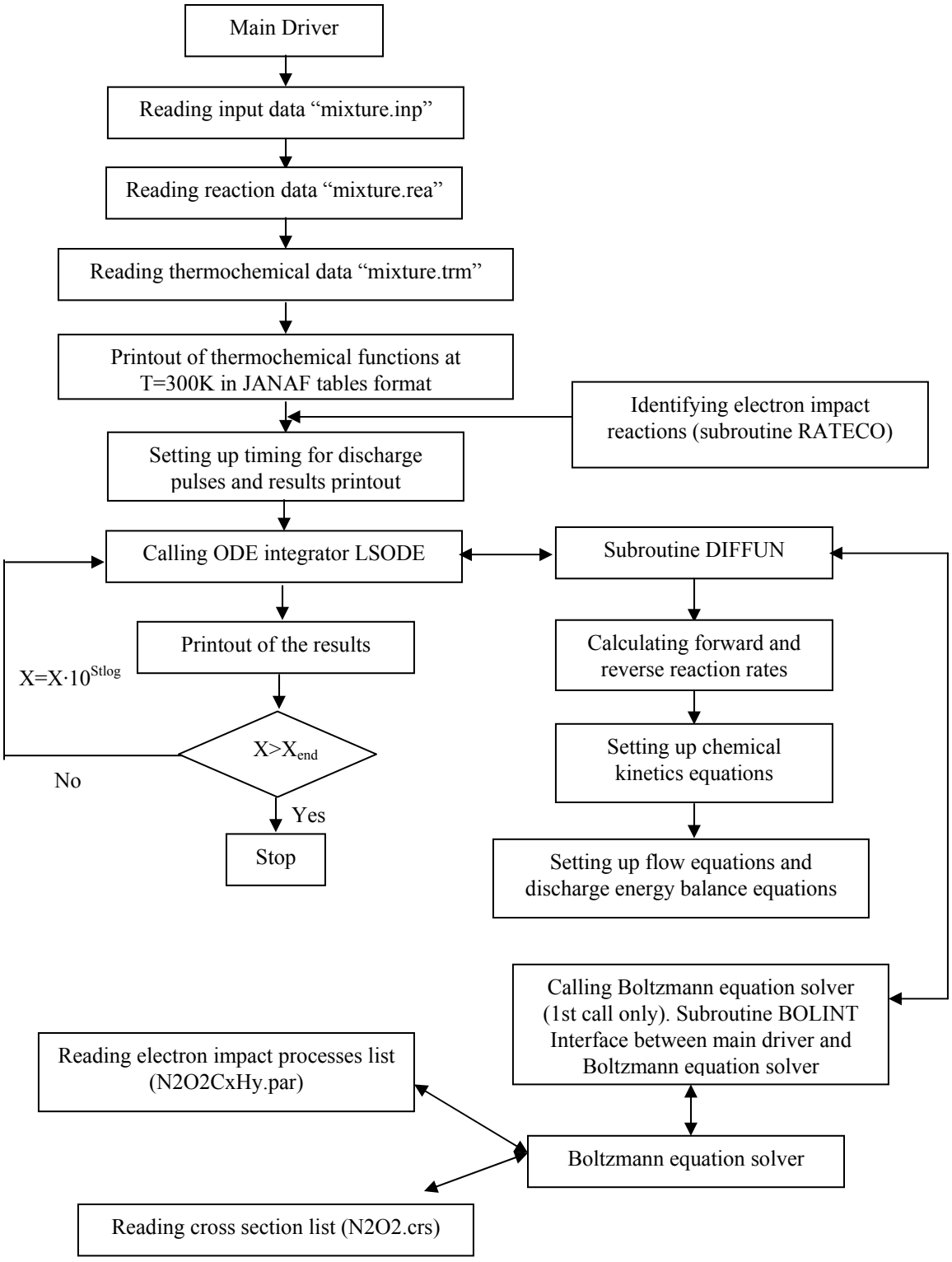

Figure 4.8: Flow chart of the code

		Unit	Typical Value
Flow parameters	Initial temperature	K	300
	Initial pressure	atm	0.0921
	Mass flow rate	g/s	0.8
Test section geometry	Width	m	0.05
	Height	m	0.01
	Discharge length	m	0.04
	Computational domain length	m	0.20
	Gap between the electrodes	cm	1.0
Pulsed discharge parameters	First pulse timing	m	1e-7
	Pulse duration	ns	15
	Delay time between the pulses	μs	20
	Peak pulse voltage	kV	7.55
	Peak pulse current	A	21.0
Initial mixture composition mole fraction	N_2		0.78
	O_2		0.22
	C_2H_4/CH_4		0.0
Stlog	Printout frequency		0.01

Table 4.7: List of initial conditions for a repetitively pulsed discharge in air in a file "mixture.inp"

On the first call of subroutine DIFFUN, it calls subroutine BOLINT, which is the interface between the Boltzmann equation solver and the rest of the code. The Boltzmann solver reads the list of electron impact processes from a file "N2O2CxHy.par", and the list of cross sections of these processes as functions of electron energy from a file "N2O2.crs". After that, the Boltzmann solver integrates the Boltzmann equation, Eq. (4.34), for an array of E/N values and obtains the electron energy distribution function (EEDF), f(ε), for a number of E/N values. Finally, Boltzmann solver calculates electron impact rate coefficients by integrating experimental cross sections over the EEDF (Eq. (4.43)), stores them, and returns to DIFFUN.

On every call, subroutine DIFFUN calculates the forward and the reverse reaction rate coefficients (using the relation between the forward and the reverse rates, Eq. (4.25), as functions of temperature. The rates of electron impact rate coefficients are assigned to appropriate reactions, using reaction "tags" given by subroutine RATECO. After this, right hand sides of chemical kinetics equations are evaluated using Eq. (4.20). Finally, right-hand-sides of flow equations Eqs. (4.4-4.5) are calculated. Before returning to the ODE integrator (LSODE), DIFFUN calls the graphics subroutine, GRAPHICS, and plots values of species mole fractions, temperature, E/N, etc., for the current value of axial location, on the screen.

Depending on the input parameter values, the code can be operated for a single pulse discharge or for a repetitively pulsed discharge.

CHAPTER 5

RESULTS OF MODELING CALCULATIONS

5.1 Kinetic model validation

To validate the kinetic model of hydrocarbon-air plasmas discussed in Chapter 4, the model predictions were compared to the results of O atom concentration measurements in a single-pulse, nanosecond pulse duration discharge [47, 64]. In Ref. [47], O atom number density after a high-voltage pulse in air, methane-air, and ethylene-air mixtures was measured using Two-Photon Absorption Laser-Induced Fluorescence (TALIF). Absolute O atom number density in a decaying plasma was measured as a function of delay time after the pulse.

In the present work, the kinetic model is used to model the results of TALIF measurements in a single-pulse discharge produced by two different pulse generators, CPT and FID pulsers (see Section 2.3), at three different pressures, P=40, 60, and 80 torr. In the experiments of Ref. [47], a single-pulse, nanosecond duration discharge was generated between two copper plate electrodes (2 cm x 6.4 cm) placed outside of a 2 cm x 1 cm, rectangular cross section quartz channel (see Fig. 5.1). The gap between the electrodes was 1.4 cm, and the quartz channel wall thickness was 1 mm. High-voltage, nanosecond duration pulses were generated at a pulse repetition rate of 10 Hz. The flow

velocity of gases through the discharge section was u≈1 m/s. Therefore the flow residence time between the electrodes was about 60 msec, i.e. the flow experienced only one pulse.

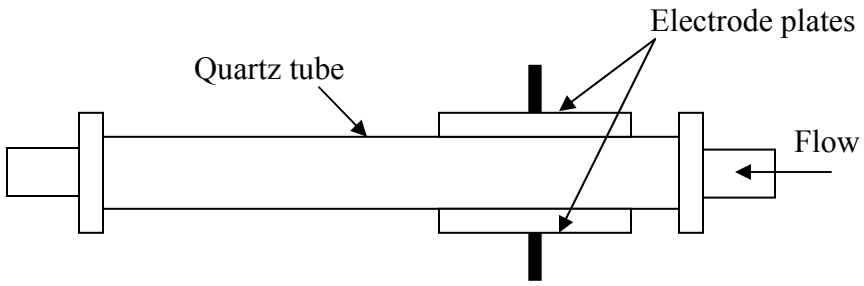

Figure 5.1: Schematic of the test section and discharge electrodes in TALIF experiments [47].

5.1.1 Single pulse discharge in air

Single-pulse discharge was modeled using a Lagrangian approach discussed in Section 4.1, without averaging over different fluid particles (see Eq. (4.3)). Since every fluid particle experiences only one pulse, averaging is not required. The model predicted plasma parameters as functions of time.

The list of kinetic processes included electron impact processes (Table 4.1), electron removal processes (Table 4.2), electronically excited species reactions (Table 4.3), ion-molecule reactions (Table 4.4), and neutral species reactions (Table 4.5). In these calculations, the electric field pulse was approximated by a Gassian shape function, (Eq. (4.17)). The pulse width was chosen to fit the experimental pulse width, t_2=15 nsec for the CPT pulse generator and t_2=3 nsec for the FID pulse generator. Figures 5.2 and 5.3 compare the normalized experimental and the model pulse shapes for CPT and FID pulse generators, respectively. As discussed in Section 4.1, pulse peak voltage was

considered an adjustable parameter. This was done to account for the effect of voltage drops across the sheaths near the dielectric-covered electrodes [49].

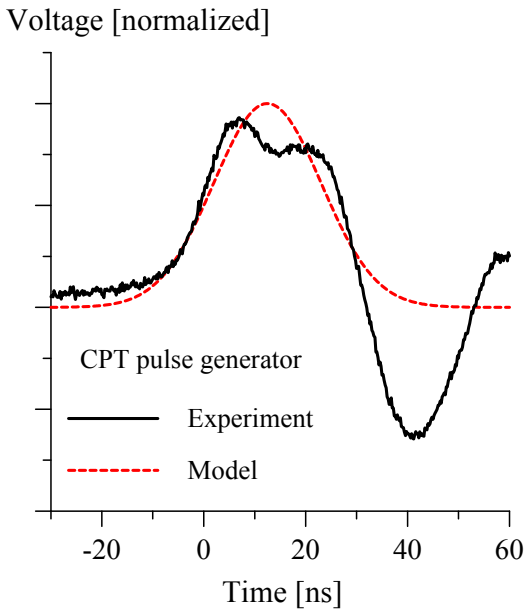

Figure 5.2. Normalized experimental and model voltage pulse shapes for the CPT pulse generator. Gaussian pulse width parameter is t_2=15 nsec.

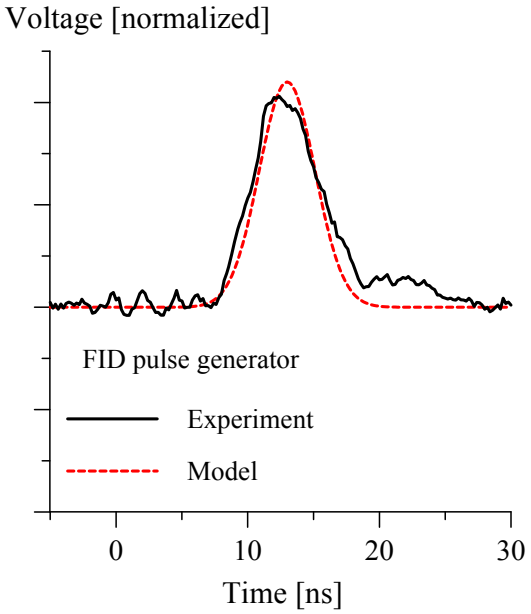

Figure 5.3. Normalized experimental and model voltage pulse shapes for the FID pulse generator. Gaussian pulse width parameter is t_2=3 nsec.

Figure 5.4 compares the experimental results and the model predictions in a single-pulse discharge produced by the CPT pulse generator at P=60 torr. In Figure 5.4, O atom mole fraction is plotted in a semi-log scale and in a linear scale. Both in the experiment and in the modeling calculations, peak O atom mole fraction is $1.4 \cdot 10^{-4}$, corresponding to the O atom concentration of $2.6 \cdot 10^{14}$ cm^{-3}. The atomic oxygen decay time (1/e) is about 2 msec. The experimental data taken at short delay times after the pulse, ~2-20 μsec, suggest that O atom number density continues to increase after the pulse is over (see Fig. 5.4). This behavior suggests that O atom dissociation after the pulse is produced by collisions of oxygen molecules with excited species generated during the pulse.

Indeed, the results of modeling calculations show that approximately 20% of O atoms are generated during the high-voltage pulse, with about 80% produced after the pulse, in collisions with electronically excited nitrogen molecules (see Fig. 5.4). Figure 5.5 shows some of species concentrations during and after the pulse. It can be seen that the rise time of O atoms after the pulse, ~10 μsec, is approximately the same as the decay time of $N_2(A^3\Sigma_u^+)$ molecules. This shows that a reaction

$$N_2(A) + O_2 \rightarrow N_2 + O + O, \tag{5.1}$$

is the dominant oxygen dissociation process after the pulse. The importance of this process can be also illustrated by the pulsed discharge energy balance plotted in Fig. 4.7. Figure 4.7 shows that approximately 80% of discharge energy is spent on electronic excitation of nitrogen. After the discharge pulse, excited electronic states of nitrogen, $C^3\Pi_u$ $a^{1'}\Sigma_u^-$, and $B^3\Pi_g$ rapidly cascade to the $A^3\Sigma_u^+$ state in collisions with N_2 and O_2,

$$N_2(C^3\Pi_u, a^1{}'\Sigma_g, B^3\Pi_g) + M \rightarrow N_2(A^3\Sigma_g^+) + M \ . \qquad (5.2)$$

Rate coefficients of theses processes are comparable with the gas kinetic rate (see Table 4.3).

Comparison of Figs. 5.4 and 5.5 also shows that the decay time of O atoms after the pulse, ≈2 msec, is the same as the rise time for the ozone concentration. This shows that the dominant O atom decay process after the pulse is the reaction

$$O + O_2 + M \rightarrow O_3 + M \ . \qquad (5.3)$$

From Fig. 5.4, it can be seen that the present kinetic model correctly reproduces the decay time of O atoms after the pulse. The fact that the model predicts a somewhat faster O atom rise time after the pulse after the pulse suggests that the detailed mechanism of O atom dissociation in collision of excited nitrogen molecules might be not completely understood. However, the overall agreement of the model predictions with the experiment is quite satisfactory.

In the modeling calculations shown in Fig. 5.4, input pulse energy is 2.11 mJ, which is close to the experimentally measured value, 1.7-1.9 mJ per pulse [47]. Figure 5.6 shows the predicted input pulse energy and the thermalized energy vs. time at these conditions. From Fig. 5.6, it can be seen that approximately one half of the input pulse energy is spent on oxygen dissociation and is stored in O atoms. After the pulse, O atom conversion into ozone by the reaction of Eq. (5.3) results in partial thermalization of this energy. However, even 10 msec after the pulse, approximately 40% of the input energy remains stored in ozone and does not thermalize. As a results, the flow temperature after a single 2.11 mJ pulse increases by $\Delta T=1.1^0$ C.

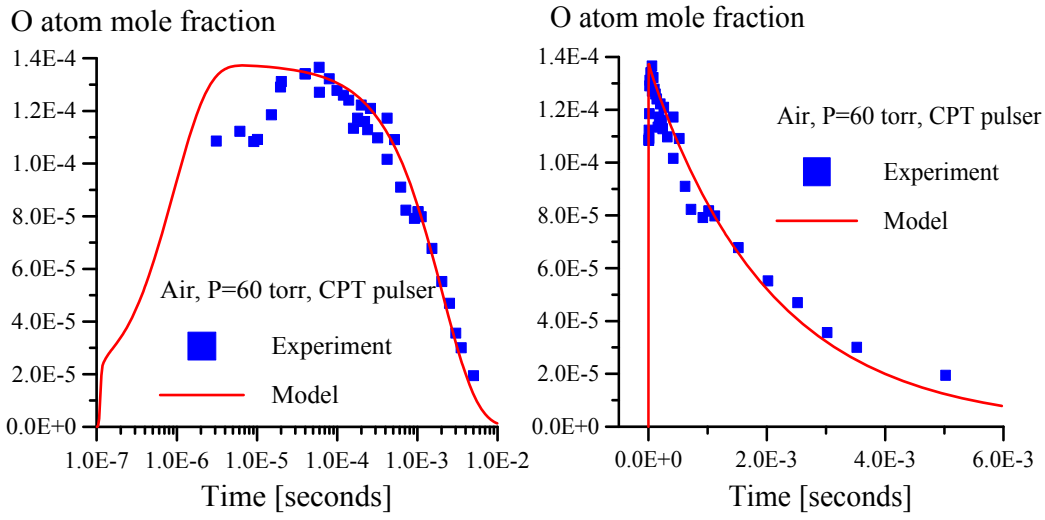

Figure 5.4: O atom mole fraction generated by a single-pulse discharge in air. Semi-log scale (left) and linear scale (right). CPT pulser, E/N=253 Td, P=60 torr, model peak voltage U=6.73 kV, calculated pulse energy 2.11 mJ.

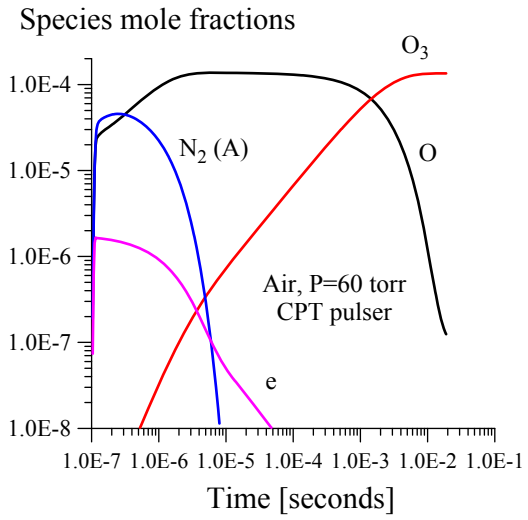

Figure 5.5: Species mole fractions generated by a single-pulse discharge in air at the conditions of Fig. 5.4.

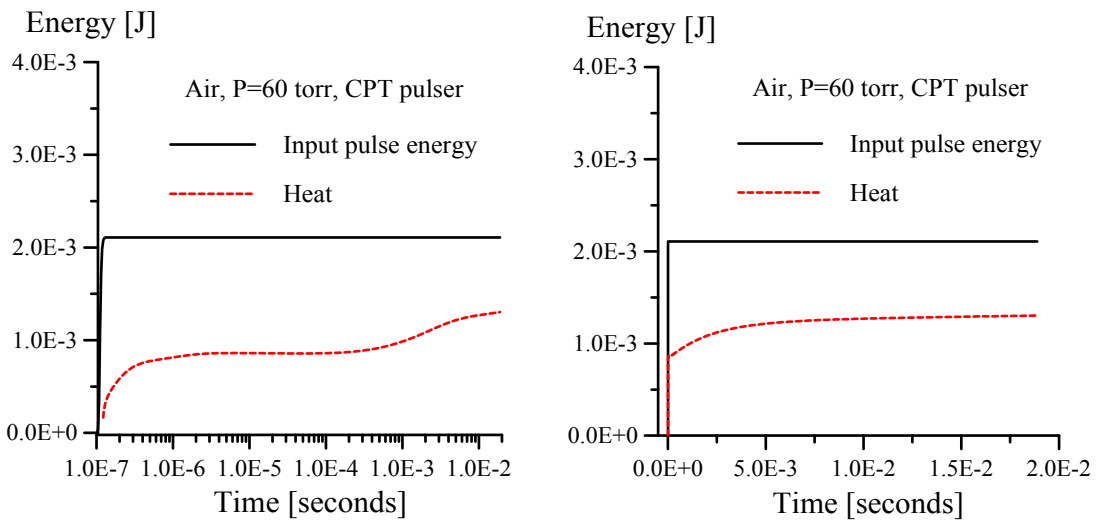

Figure 5.6: Input pulse energy and thermalized energy in a single-pulse discharge in air at the conditions of Fig. 5.4. Semi-log scale (left) and linear scale (right).

Figures 5.7 and 5.8 compare the model predictions with the TALIF measurements of O atom number density in a single-pulse discharge in air at P=40 torr and 80 torr, for the CPT pulse generator. It can be seen that the agreement between the model and the experiment is satisfactory, although the model somewhat underpredicts the O atom decay rate at 40 torr (see Fig. 5.7) and overpredicts the peak O atom density at 80 torr (see Fig. 5.8). Figures 5.9-5.11 compare simulation results with the single-pulse experimental measurements using the FID pulser, also at P=40, 60, and 80 torr. From Fig. 5.9-5.11, it can be seen that the model also adequately reproduces the results of the TALIF measurements using the FID pulser. In fact, in this case the predicted O atom concentrations at short delay times after the pulse (1-100 μsec) are in better agreement with the experimental results. The results of Figs. 5.4 – 5.11 demonstrate consistent agreement between the model predictions and the experimental data. This comparison provides validation of the pulsed discharge air plasma model.

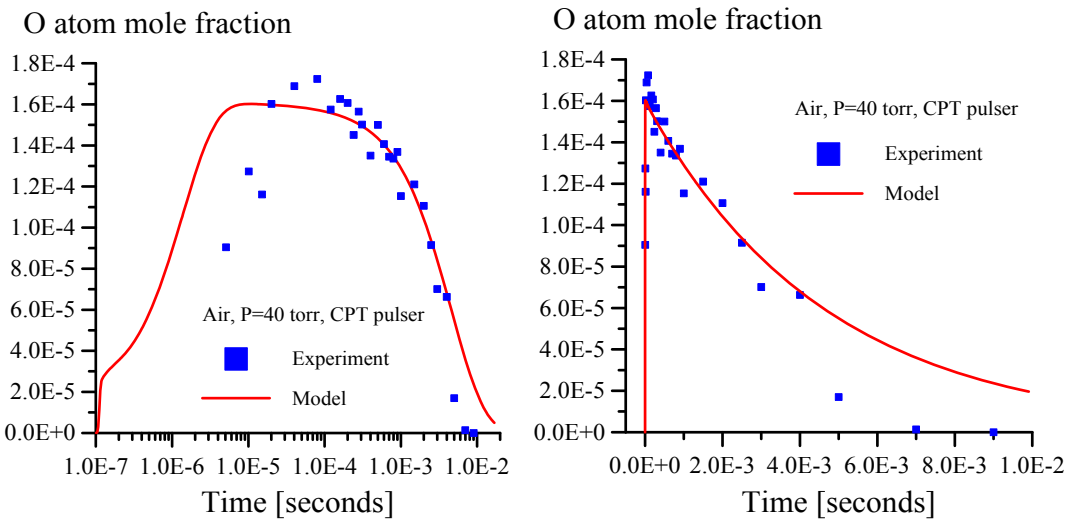

Figure 5.7: O atom mole fraction generated by a single-pulse discharge in air. Semi-log scale (left) and linear scale (right). CPT pulser, E/N=282 Td, P=40 torr, model peak voltage U=5.01 kV, calculated pulse energy 1.61 mJ.

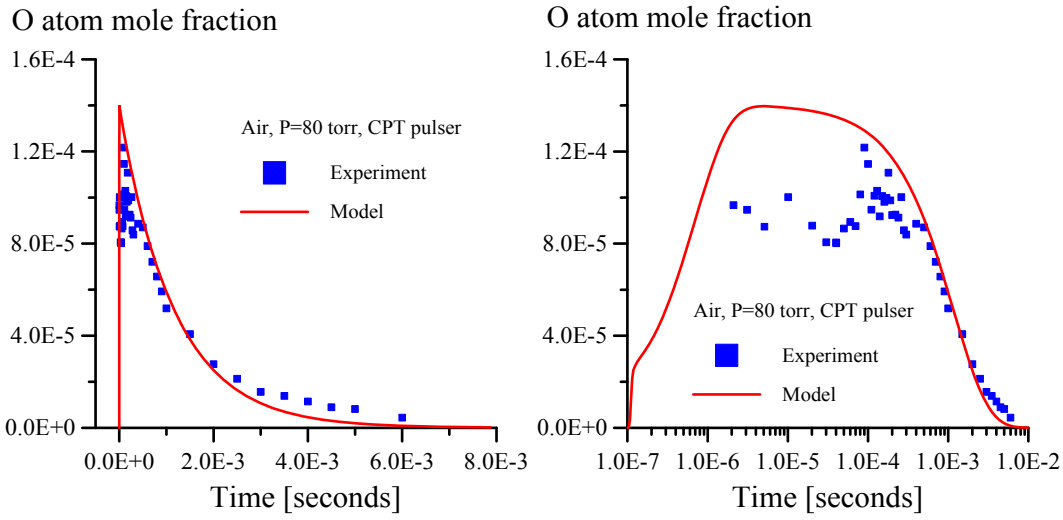

Figure 5.8: O atom mole fraction generated by a single-pulse discharge in air. Semi-log scale (left) and linear scale (right). CPT pulser, E/N=235 Td, P=80 torr, model peak voltage U=8.36 kV, calculated pulse energy 2.91 mJ.

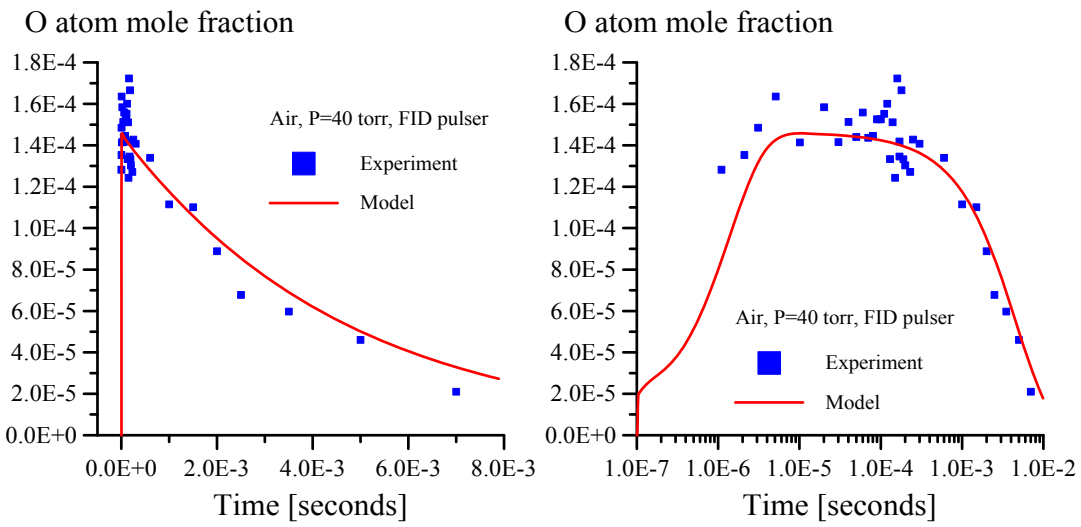

Figure 5.9: O atom mole fraction generated by a single-pulse discharge in air. Semi-log scale (left) and linear scale (right). FID pulser, E/N=477 Td, P=40 torr, model peak voltage U=8.47 kV, calculated pulse energy 1.53 mJ.

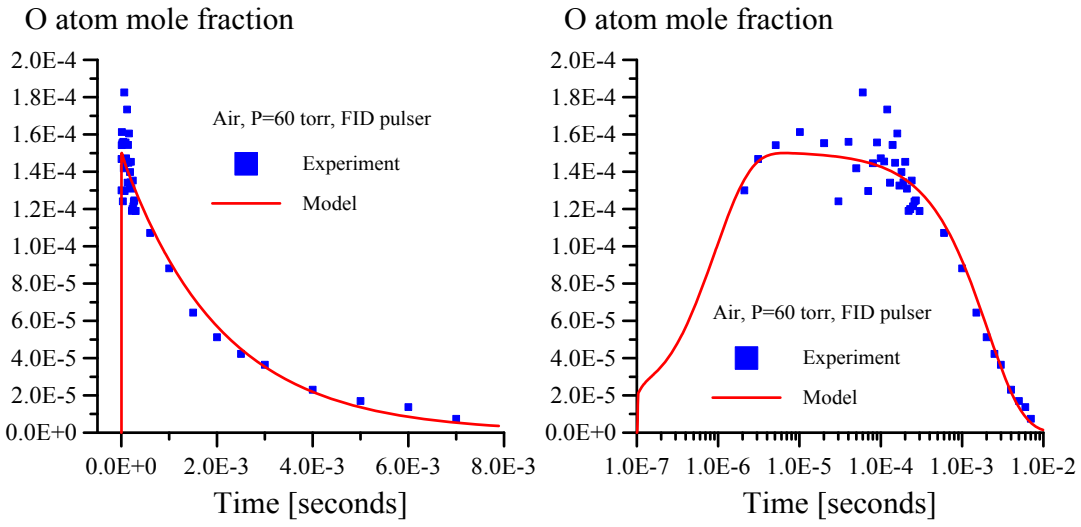

Figure 5.10: O atom mole fraction generated by a single-pulse discharge in air. Semi-log scale (left) and linear scale (right). FID pulser, E/N=415 Td, P=60 torr, model peak voltage U=11.03 kV, calculated pulse energy 2.33 mJ.

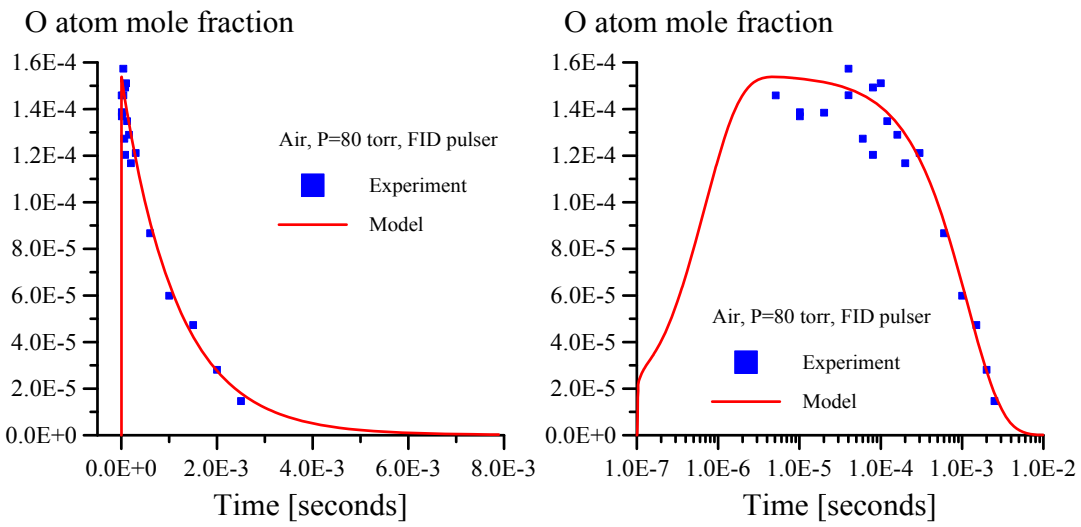

Figure 5.11: O atom mole fraction generated by a single-pulse discharge in air. Semi-log scale (left) and linear scale (right). FID pulser, E/N=377 Td, P=80 torr, model peak voltage U=13.33 kV, calculated pulse energy 3.15 mJ.

Since the ionization fraction in the nanosecond pulse is low compared to the oxygen dissociation fraction (~10^{-6} vs. ~10^{-4}, see Fig 5.5), ion-molecule reactions listed in Tables 4.2 and 4.4 are unlikely to affect the neutral species chemistry. For this reason, the only charged species that strongly affects the neutral species kinetics is the electron. Note that the electron density also directly affects the pulse energy, calculated by Eq. (4.16). For this reason, a simplified kinetic model can be used for a single-pulse discharge, in which the electron density is not calculated from the kinetic equation such as Eq. (4.6), but is used as an adjustable parameter, varying in the same way as the applied electric field,

$$n_e(t) = n_{eo} \exp\left[-\left(\frac{t-t_1}{t_2}\right)^2\right], \tag{5.4}$$

(compared with Eq. (4.17)). In Eq. (5.4), n_{eo} is the peak electron density adjusted to match the pulse energy calculated using the full kinetic model (with ion-molecule reactions).

Figure 5.12 (a) plots the time-dependent reduced electric field and the current for the full kinetic model, for the conditions of Fig. 5.4 (air, P=60 torr, CPT pulser). It can be seen that electric breakdown occurs and the current increases from zero at near peak voltage. After this moment, both the electron density and the current increase exponentially and then drop due to the electric field reduction toward the end of the pulse (see Fig. 5.12 (a)). Figure 5.12 (b) shows the reduced electric field and the current for the simplified kinetic model (without ion-molecule reactions of Tables 4.2, 4.4). In this case, the reduced electric field profile is the same as for the full model, and the electron density is calculated from Eq. (5.4). The peak electron density is adjusted to produce the same pulse energy as predicted by the full model, 2.11 mJ. For the sake of convenience, this is done by varying the peak current value in the input file, "mixture.inp" (see Section 4.4). As can be seen from Fig. 5.12 (b), the electron density for the simplified model is in phase with the E/N pulse.

Figure 5.13 compares O atom mole fractions predicted by the full and the simplified models with the experimental results (air, P=60 torr, CPT pulser). It can be seen that both models predictions are very close to each other. This demonstrates that species concentrations predicted by the model are mainly determined by the pulse peak voltage (pulse energy) rather than by the electron density profile during the pulse, or by details of charged species kinetics.

This result is very helpful for kinetic modeling of hydrocarbon-air plasmas in a nanosecond pulse discharge. Indeed, in a hydrocarbon-air plasma, the number of possible ion species becomes very large, and the number of ion-molecule reactions among these species can be a few hundreds. Since rate coefficients for many of these reactions are known with significant uncertainty, or not known at all, kinetic modeling of these plasmas, with charged species chemistry incorporated, becomes nearly impossible. On the other hand, the result of Fig. 5.13 shows that the neutral species kinetics is mainly controlled by the pulse energy. Therefore, if the experimental pulse energy is measured, hydrocarbon-air pulsed plasma kinetics can be modeled using the simplified model described above.

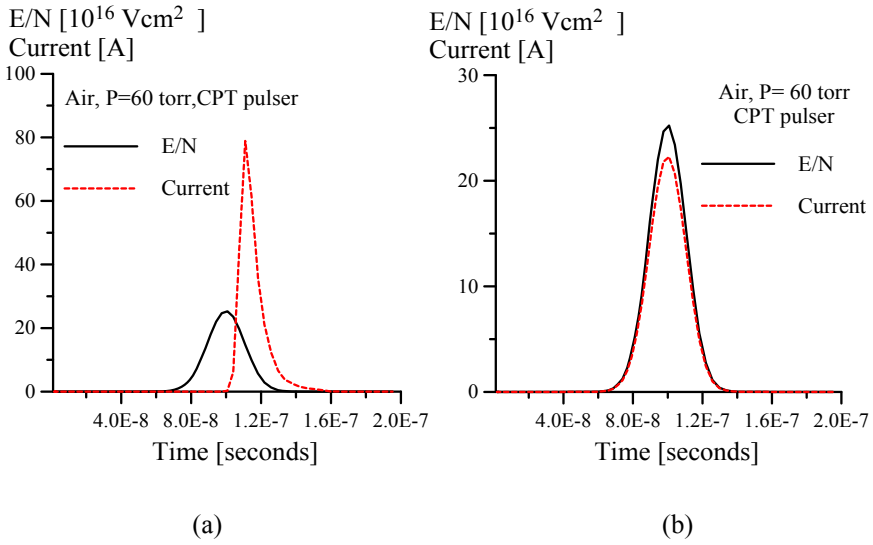

Figure 5.12: Time-dependent reduced electric field and current calculated using the full kinetic model (left) and the simplified kinetic model (right). Air, P=60 torr, peak E/N for the full model is chosen to fit the experimental data for the CPT pulser (see Fig. 5.4).

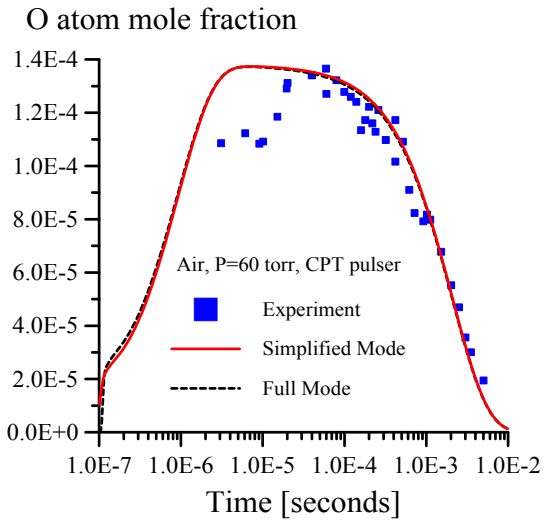

Figure 5.13: O atom concentrations predicted by the full and the simplified kinetic models, compared with the experimental results at the conditions of Fig. 5.4.

After removing charged species kinetics, the simplified air plasma model still incorporates several tens of reactions (see Tables 4.1, 4.3, 4.5). To obtain insight into air plasma kinetics, the reduced kinetic mechanism was identified by removing processes which do not strongly affect the O atom concentration and the thermalized pulse energy from the reaction list. The remaining key processes are listed in Table 5.1. They include (i) oxygen dissociation by electron impact, (ii) nitrogen electronic excitation by electron impact, (iii) excited nitrogen quenching in collisions with O_2 molecules, resulting in cascading to $N_2(A^3\Sigma_u^+)$ and oxygen dissociation, and (iv) O atom decay in reactions with O_2 and O_3.

Figures 5.14 and 5.15 compare O atom mole fraction and thermalized pulse energy for the full and the reduced kinetic mechanisms. It can be seen that the two mechanisms indeed predict very close results.

	Reaction
O atom generation	$N_2 + e^- = N_2(A) + e^-$
	$N_2 + e^- = N_2(B) + e^-$
	$N_2 + e^- = N_2(C) + e^-$
	$N_2 + e^- = N_2(a) + e^-$
	$O_2 + e^- = O + O + e^-$
	$N_2(C) + O_2 = N_2(a) + O_2$
	$N_2(a) + O_2 = N_2(B) + O_2$
	$N_2(B) + O_2 = N_2(A) + O_2$
	$N_2(A) + O_2 = N_2 + O + O$
O atom decay	$O + O_2 + M = O_3 + M$
	$O + O_3 = O_2 + O_2$

Table 5.1: Reduced kinetic mechanism of a pulsed air plasma

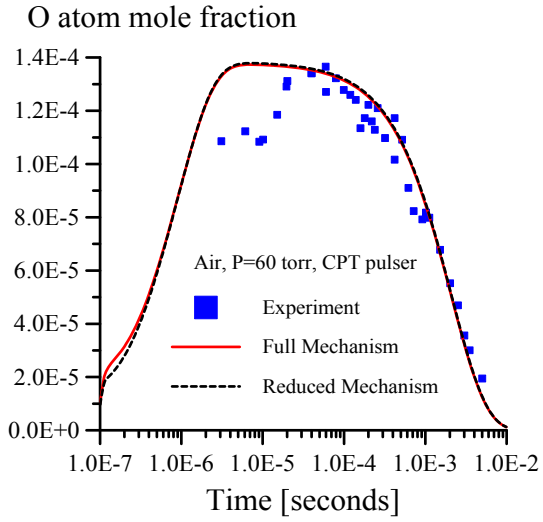

Figure 5.14: Comparison of O atom mole fractions for the full and the reduced kinetic mechanisms at the conditions of Fig. 5.4.

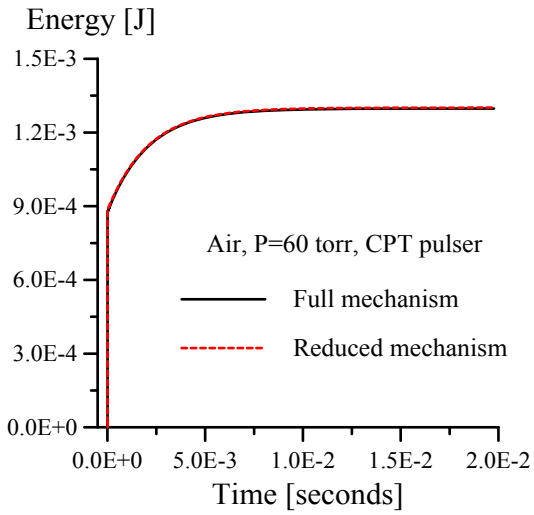

Figure 5.15: Comparison of the thermalized pulse energy for the full and the reduced kinetic mechanisms at the conditions of Fig. 5.4.

5.1.2 Single pulse discharge in a methane-air mixture

The simplified kinetic model (without charged species reactions) was used to model O atom measurements in a pulsed discharge in a stoichiometric methane-air mixture at P=60 torr, using the CPT pulse generator. Note that xenon calibration of absolute O atom number densities repeated in this series of experiments showed that previous O atom concentrations in air (see Figs. 5.4, 5.7-5.11) were considerably overestimated (by about a factor of three). For this reason, in the following calculations, the pulse energy was reduced to produce peak O atom number density in air close to the experimentally measured and recalibrated value. Specifically, for all CPT pulse experiments at P=60 torr, discussed in Sections 5.1.2 and 5.1.3, the pulse energy was 0.60 mJ (peak pulse voltage of U=6.48 kV). Figure 5.16 compares time-dependent O atom mole fractions in a single-pulse discharge in air and in a stoichiometric methane-air mixture, both at P=60 torr, using the CPT pulser. It can be seen that in methane-air, the O atom density decays faster than in air.

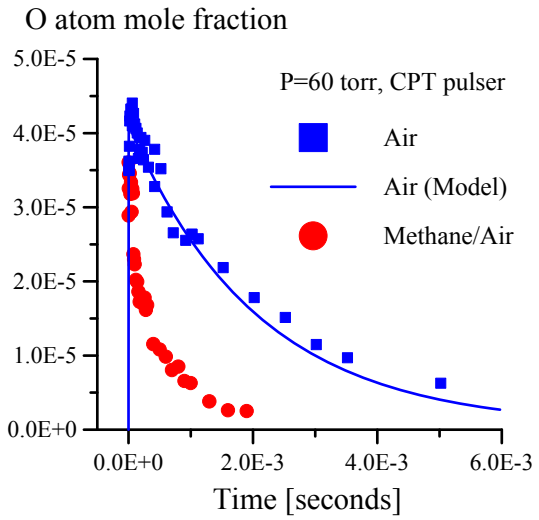

Figure 5.16: Comparison of O atom mole fractions in a single-pulse discharge in air and in a stoichiometric methane-air. P=60 torr, CPT pulser.

To identify kinetic processes responsible for the accelerated O atom decay in methane-air, the kinetic modeling calculations have been done for following kinetic mechanisms:

Case 1: Air plasma model (see Tables 4.1, 4.3, and 4.5) combined with the GRI-Mech 3.0 mechanism (see Appendix C) of hydrocarbon oxidation (baseline model).

Case 2: Baseline model with electron impact dissociation of methane (see Table 4.6).

Case 3: Baseline model with electron impact dissociation of methane and methane dissociation in collisions with electronically excited nitrogen molecules (see Table 4.6).

Figure 5.17 compares modeling calculation results for these three cases with the experimental data. It can be seen that for Case 1, the predicted O atom decay rate is

essentially the same as in air. This is expected since the rate coefficient of O atom reaction with CH_4,

$$O + CH_4 \rightarrow OH + CH_3, \tag{5.5}$$

at room temperature is very slow, $k=4.7\cdot10^{-18}$ cm^3/s. Basically, this demonstrates that the accelerated O atom decay in a CH_4-air mixture occurs due to generation of additional radical species in the plasma, such as H and CH_3, in fuel dissociation processes.

Indeed, adding electron impact dissociation of methane (Case 2) results in a faster O atom decay (see Fig. 5.17). Finally, adding methane dissociation in collisions with electronically excited nitrogen (Case 3) accelerates O atom decay after the pulse even more, and it becomes close to the experimental data (see Fig. 5.17). Note that adding this last group of processes to the model results in a reduction of the peak O atom number density (see Fig. 5.17). Basically, fewer electronically excited N_2 molecules are now available to dissociate O_2 molecules. This result is at variance with experimental observations, which show that peak O atom mole fractions in air and in methane-air mixture are approximately the same (see Fig. 5.16). This suggests that the kinetic mechanism of methane dissociation in the pulsed discharge might be more complex. However, the overall agreement between the model and the experiment is satisfactory.

Figure 5.18 shows input pulse energy and thermalized energy at the conditions of Fig. 5.17 (Case 3). It can be seen that the thermalized energy is close to the input energy at the end of simulation (t=20 msec), exceeding it by approximately 15%. Comparing these results with the model predictions for a single-pulse discharge in air (see Fig. 5.6), one can see that there is basically no energy storage in reaction products, and there is also a modest additional energy release due to oxidation of fuel. This result suggests that there

is almost no additional energy release (heat) in methane-air mixtures due to plasma chemical reactions of fuel oxidation. In other words, the discharge acts simply as a flow heater, and its effect on the combustible mixture is predominantly thermal.

Figure 5.19 plots stable oxidation product concentrations and radical species concentrations, as functions of time. It can be seen that the dominant oxidation products are water vapor, formaldehyde (CH_2O), and carbon monoxide. The total mole fraction of all carbon-containing product species (CO, CO_2, and CH_2O) is $1 \cdot 10^{-5}$, which is considerably less than the peak mole fraction of the primary radical generated by the discharge, O atoms, ($2.5 \cdot 10^{-5}$), see Fig. 5.17. The total carbon-containing product species mole fraction is fairly close to the sum of mole fractions of H and CH_3 radicals generated by the discharge (see Fig. 5.19). This demonstrates that the stable product species (CO, CO_2, and CH_2O) are mainly produced by recombination of the primary radicals generated in the plasma (O, H and CH_3), without significant chain reactions involved. Producing stable product species in excess of the amount of radicals generated by the plasma would be evidence of such chain reaction process, which does not seem to occur here. This conclusion is confirmed by identifying the reduced mechanism of methane oxidation in a single-pulse discharge.

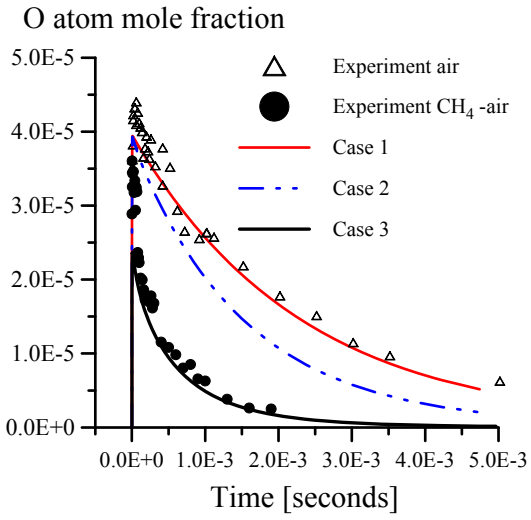

Figure 5.17: Experimental and predicted O atom mole fractions in a single-pulse discharge in a stoichiometric methane-air mixture (P=60 torr, CPT pulser).
Case 1: baseline mechanism (air plasma model + GRI-Mech mechanism of hydrocarbon oxidation)
Case 2: baseline mechanism + electron impact dissociation of methane
Case 3: baseline mechanism + electron impact dissociation of methane + methane dissociation by N_2*.

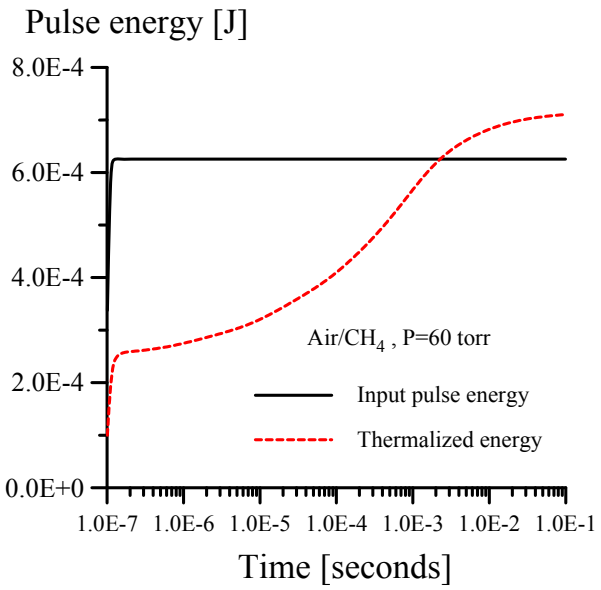

Figure 5.18: Input pulse energy and thermalized energy in a stoichiometric methane-air mixture at the conditions of Fig. 5.17 (Case 3).

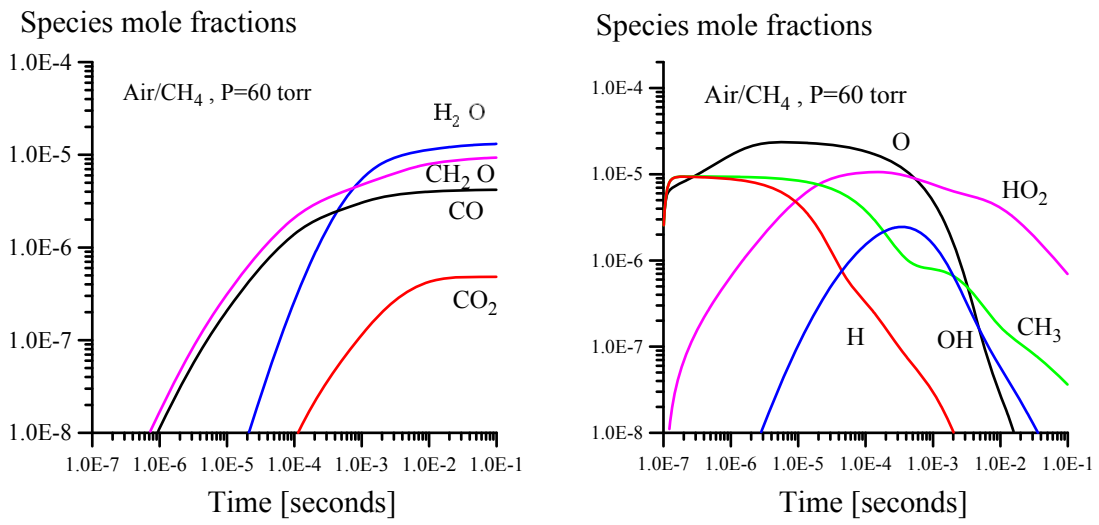

Figure 5.19: Stable oxidation product mole fractions (left) and radical species mole fractions (right) in a single-pulse discharge in a stoichiometric methane-air mixture at the conditions of Fig. 5.17 (Case 3).

The reduced kinetic mechanism of methane oxidation in a single-pulsed discharge is listed in Table 5.2. It has been obtained by using the same approach as for the air plasma, discussed in Section 5.1.1. Note that in Table 5.2, reduced mechanism of O atom generation and decay in air (see Table 5.1) is omitted. To describe kinetics of O atom generation and fuel oxidation in air-methane mixtures, the mechanisms of Table 5.1 and Table 5.2 need to be combined. In Table 5.2, the reduced mechanism processes are divided into three groups, (i) fuel dissociation reactions, both by electron impact and collisions with excited nitrogen, (ii) rapid reactions of ground electronic state species controlling the rate of O atom decay, and (iii) relatively slow exothermic fuel oxidation reactions controlling energy release after the pulse. Figures 5.20 and 5.21 compare O atom mole fraction and thermalized energy for the full methane oxidation mechanism (Case 3 in Fig. 5.17) and the reduced mechanism (Tables 5.1 and 5.2 combined). It can be seen that the reduced mechanism reproduces both these parameters very well.

Summarizing, the kinetic mechanism used in the present work (air plasma model combined with fuel dissociation reactions and GRI-Mech 3.0 mechanism of hydrocarbon oxidation) does not predict low-temperature chain reaction fuel oxidation or the additional energy release due to plasma chemical reactions, so ignition by this mechanism is unlikely to be achieved.

Index	Reaction
Fuel dissociation reactions	$CH_4 + e- = CH_3 + H + e-$
	$N_2(A) + CH_4 = N_2 + CH_3 + H$
	$N_2(B) + CH_4 = N_2 + CH_3 + H$
	$N_2(C) + CH_4 = N_2 + CH_3 + H$
	$N_2(a) + CH_4 = N_2 + CH_3 + H$
O atom decay reactions	$O + HO_2 = OH + O_2$
	$O + CH_3 = H + CH_2O$
	$H + O_2 + M = HO_2 + M$
Energy release reactions	$H + O_2 = O + OH$
	$OH + HO_2 = O_2 + H_2O$
	$OH + CH_4 = CH_3 + H_2O$
	$HO_2 + CH_3 = OH + CH_3O$
	$CH_3O + O_2 = HO_2 + CH_2O$

Table 5.2: Reduced kinetic mechanism for methane-air plasma (complements processes of Table 5.1).

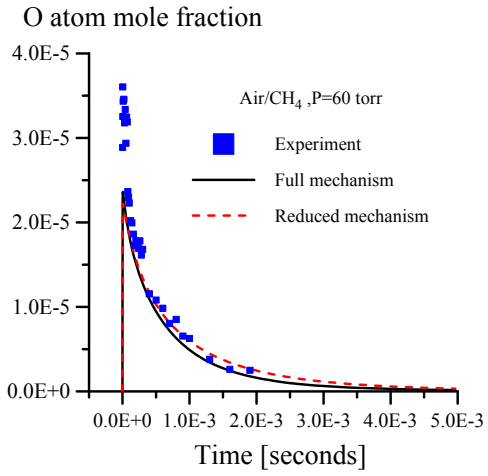

Figure 5.20: Comparison of O atom mole fractions for the full and the reduced kinetic mechanisms for methane-air. The conditions are the same as in Fig. 5.17.

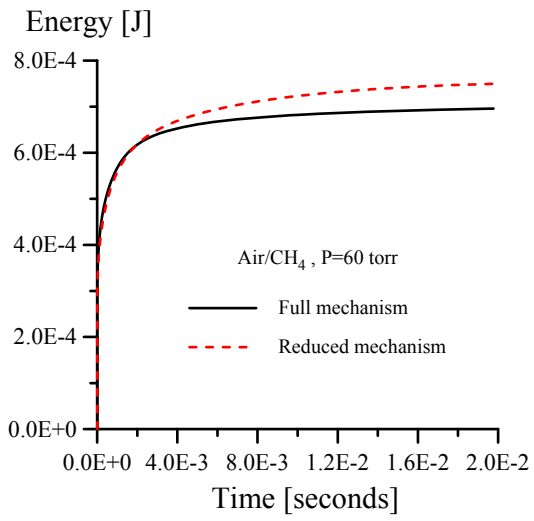

Figure 5.21: Comparison of the thermalized pulse energy for the full and the reduced kinetic mechanisms for methane-air. The conditions are the same as in Fig. 5.17.

5.1.3 Single pulse discharge in an ethylene-air mixture

The simplified kinetic model was also used to model the O atom mole fraction in a single-pulse discharge generated by the CPT pulser in a Φ=0.5 ethylene-air mixture at P=60 torr, and to compare it with the results of TALIF experiments. The peak pulse voltage in these calculations was the U=6.48 kV (see Section 5.1.2). Figure 5.22 compares O atom mole fractions in a single-pulse discharge in air and in a Φ=0.5 ethylene-air mixture, at P=60 torr. It can be seen that in the ethylene-air mixture, the O atom density decays much faster than in air.

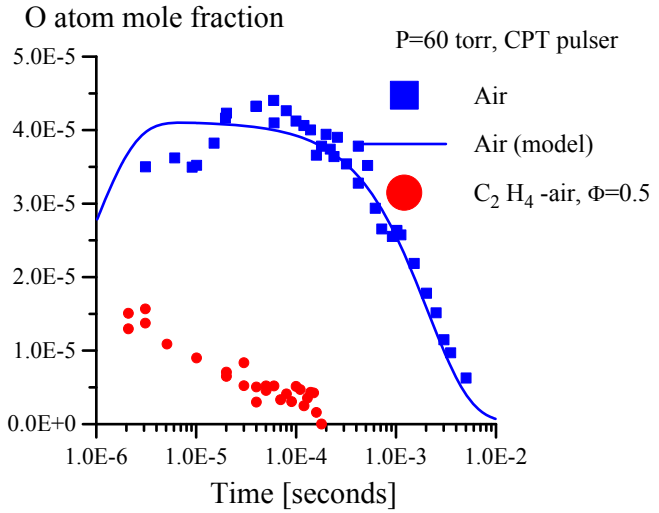

Figure 5.22: Comparison of O atom mole fractions in a single-pulse discharge in air and in a Φ=0.5 ethylene-air mixture. P=60 torr, CPT pulser.

To identify kinetic processes responsible for the rapid O atom decay, several kinetic mechanisms were considered (see Section 5.1.3):

Case 1: Air plasma model (Tables 4.1, 4.3, and 4.5) combined with GRI-Mech 3.0 mechanism (see Appendix C) of hydrocarbon oxidation (baseline model).

Case 2: Baseline model with electron impact dissociation of ethylene (see Table 4.6).

Case 3: Baseline model with electron impact dissociation of ethylene and ethylene dissociation in collisions with electronically excited nitrogen molecules (see Table 4.6).

Figure 5.23 compares modeling results for these three cases with the experimental data. Even for the baseline case (Case 1), the predicted O atom decay is much faster than in methane-air, since the rate coefficients of O atom reactions with C_2H_4,

$$O + C_2H_4 \rightarrow CH_3 + HCO \qquad (5.6)$$

and

$$O + C_2H_4 \rightarrow H + CH_2CHO\,, \tag{5.7}$$

at room temperature are fairly high, $k=4.9\cdot10^{-13}$ cm^3/s and $k=2.6\cdot10^{-13}$ cm^3/s, respectively. This is much faster than the rate coefficient of the reaction of O with CH_4, see Eq. (5.5), $k=4.7\cdot10^{-18}$ cm^3/s. Therefore the rapid O atom decay in the ethylene-air mixture occurs mainly due to reactions of Eqs. (5.7, 5.8). However, the peak O atom number density for Case 1 is overestimated (see Fig. 5.23). Adding electron impact dissociation of ethylene (Case 2) produces almost no difference compared to Case 1 (see Fig. 5.23). Finally, adding ethylene dissociation in collisions with electronically excited nitrogen results in a reduction of the peak O atom density, which becomes close to the experimental result (see Fig. 5.23). Basically, adding the processes of Case 3 reduces the number of N_2^* molecules available to dissociate O_2 since they are used to dissociate ethylene. For Case 3, the agreement between the model and the experiment is very well.

Figure 5.24 compares the input pulse energy and the thermalized energy in ethylene-air at the conditions of Fig. 5.23 (Case 3). It can be seen that the thermalized energy exceeds the input energy at the end of the simulation, at t=100 msec, by about 80% (1.1 mJ vs. 0.6 mJ). In this case, there is a significant additional energy release due to plasma chemical reactions of ethylene oxidation.

Figure 5.25 plots stable oxidation product concentrations and radical species concentrations, as functions of time. It can be seen that the dominant oxidation products are carbon monoxide, formaldehyde (CH_2O), and water vapor. The total mole fraction of all carbon containing product species (CO, CH_2O, and CO_2) is $5\cdot10^{-5}$, which exceeds the peak mole fraction of O atoms generated in the plasma ($1.5\cdot10^{-5}$, see Fig. 5.25). The total mole fraction of all carbon containing product species is greater than the sum of mole

fractions of radicals (H, CH_3, and O) generated in the plasma, $3 \cdot 10^{-5}$. This suggests presence of chain processes of plasma chemical ethylene oxidation.

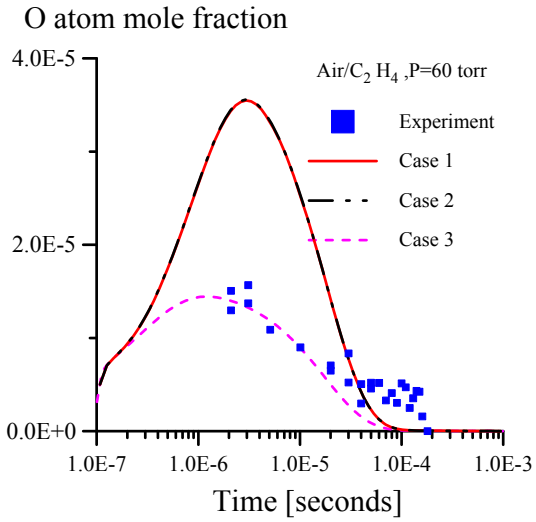

Figure 5.23: Experimental and predicted O atom mole fractions in a single-pulse discharge in a Φ=0.5 ethylene-air mixture (P=60 torr, CPT pulser) in a semi-log scale.
Case 1: baseline mechanism (air plasma model + GRI mechanism of hydrocarbon oxidation)
Case 2: baseline mechanism + electron impact dissociation of ethylene
Case 3: baseline mechanism + electron impact dissociation of ethylene + ethylene dissociation by N_2*.

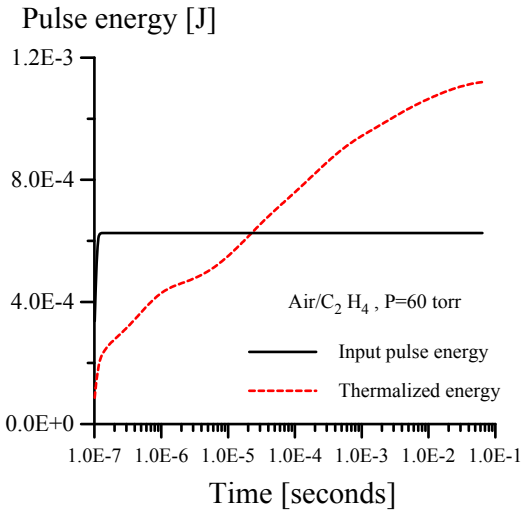

Figure 5.24. Input pulse energy and thermalized energy in a Φ=0.5 ethylene-air mixture at the conditions of Fig. 5.23 (case 3).

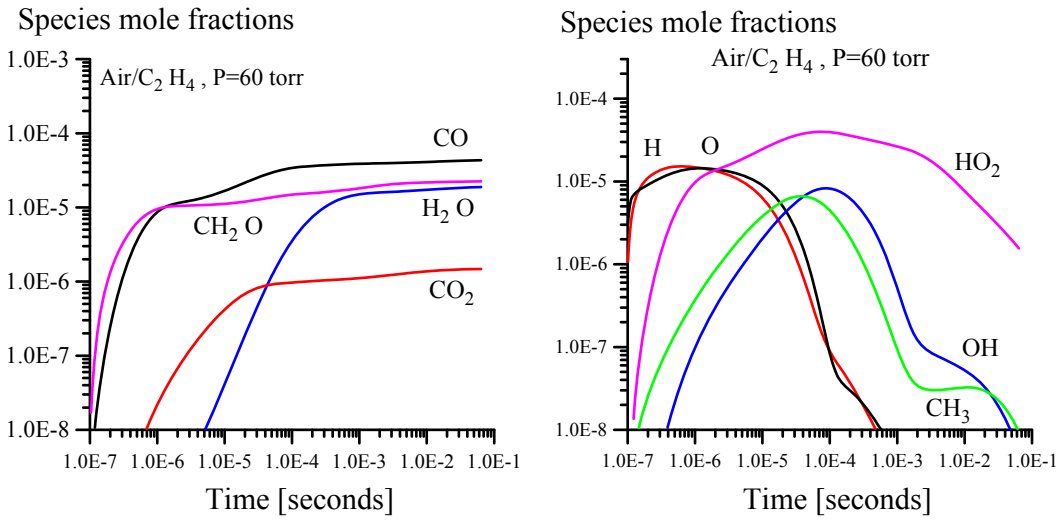

Figure 5.25: Stable oxidation product mole fractions (left) and radical species mole fractions (right) in a single-pulse discharge in a Φ=0.5 ethylene-air mixture at the conditions of Fig. 5.23 (case 3).

The reduced kinetic mechanism of ethylene oxidation in the pulsed discharge is listed in Table 5.3. Combining Tables 5.1 and 5.3 can describe kinetics of O atom generation/decay and fuel oxidation in ethylene-air mixtures. Similar to Table 5.2, the reactions in Table 5.3 are divided into three groups, (i) fuel dissociation reactions, (ii) rapid O atom decay reactions, and (iii) relatively slow energy release reactions. Figures 5.26 and 5.27 compare O atom mole fraction and thermalized pulse energy for the full ethylene oxidation mechanism and the reduced mechanism (combined Tables 5.1 and 5.3). It can be seen that the agreement between the full model and the reduced model is very good.

Summarizing, the kinetic mechanism of a single-pulse discharge plasma in a ethylene-air mixture (air plasma model combined with fuel dissociation reactions and GRI-Mech 3.0 mechanism of hydrocarbon oxidation) predicts existence of low-temperature chain reactions of ethylene oxidation and additional energy release due to plasma chemical reactions.

	Reaction
Fuel dissociation reactions	$C_2H_4 + e- = C_2H_3 + H + e-$
	$N_2(A) + C_2H_4 = N_2 + C_2H_3 + H$
	$N_2(B) + C_2H_4 = N_2 + C_2H_3 + H$
	$N_2(C) + C_2H_4 = N_2 + C_2H_3 + H$
	$N_2(a) + C_2H_4 = N_2 + C_2H_3 + H$
O atom decay reactions	$O + C_2H_4 = H + CH_2CHO$
	$O + C_2H_4 = CH_3 + HCO$
	$C_2H_3 + O_2 = HCO + CH_2O$
	$C_2H_3 + O_2 = O + CH_2CHO$
Energy release reactions	$O + HO_2 = OH + O_2$
	$O + CH_2CHO = H + CH_2 + CO_2$
	$H + O_2 + M = HO_2 + M$
	$OH + HO_2 = O_2 + H_2O$
	$OH + C_2H_4 = C_2H_3 + H_2O$
	$HO_2 + HO_2 = O_2 + H_2O_2$
	$HO_2 + CH_3 = OH + CH_3O$
	$O_2 + CH_2CHO = OH + HCO + HCO$
	$CH_2 + O_2 = H + H + CO_2$
	$HCO + O_2 = HO_2 + CO$
	$CH_3O + O_2 = HO_2 + CH_2O$

Table 5.3: Reduced kinetic mechanism of ethylene-air plasma (complements processes of Table 5.1)

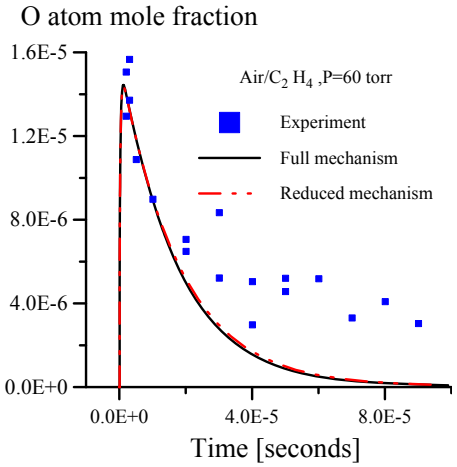

Figure 5.26: Comparison of O atom mole fractions for the full and the reduced kinetic mechanisms for ethylene-air. The conditions are the same as in Fig. 5.23.

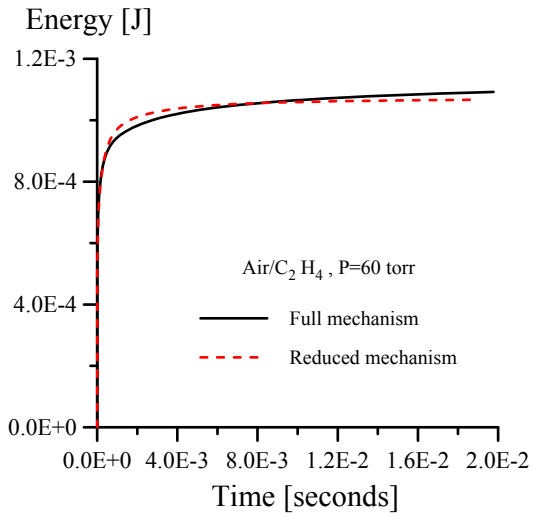

Figure 5.27: Comparison of the thermalized pulse energy for the full and the reduced kinetic mechanisms for ethylene-air. The conditions are the same as in Fig. 5.23.

5.1.4 GRI 3.0 mechanism validation: ethylene autoignition temperature

To provide additional validation of the GRI-Mech 3.0 hydrocarbon oxidation mechanism, it was used to calculate ignition delay time in a stoichiometric ethylene-air mixture at constant pressure, as a function of initial temperature. In these calculations, plasma chemical processes were not incorporated. Ignition delay time was defined as

$$\left.\frac{d^2T}{dt^2}\right|_{t=t_{delay}} = 0, \tag{5.8}$$

which occurs when $\frac{dT}{dt}$ reaches maximum. Figure 5.28 shows the temperature and the normalized $\frac{dT}{dt}$ distributions at P=0.1 bar and the initial temperature of T_i=2000 K. The peak value of $\frac{dT}{dt}$ corresponds to ignition delay time of t_{ign}=63 μsec. Figure 5. 29 plots ignition delay times vs. initial temperature for stoichiometric C_2H_4-air and CH_4-air mixtures at 70 torr and 90 torr, respectively. It can be seen that at low temperatures,

ignition delay time asymptotically goes to infinity as the temperature approaches autoignition limit, 650^0 C for ethylene-air and 750^0 C for methane-air. Figure 5.30 plots experimental autoignition temperatures in ethylene-air mixtures for different equivalence ratios and pressures [23]. As can be seen from Fig. 5.30, autoignition temperature is 570^0 C for 5% ethylene in air and 710^0 C for 10% ethylene in air, which is consistent with the 650^0 C predicted by the model for a stoichiometric ethylene-air mixture (6.5% ethylene in air). Autoignition temperature predicted by the model for a 5% ethylene/air mixture (Φ=0.77) is 600^0 C, which is again close to the experimental value of 570^0 C (see Fig. 5.30).

Figure 5.31 compares ignition delay time in a stoichiometric ethylene-air mixture at P=0.1 bar with the modeling calculations of Ref. [3]. This is done to cross-validate the present model by comparing it with other kinetic models. It can be seen that the results of both models are very close.

Figures 5.29-5.31 show that the present kinetic model correctly describes thermal oxidation and ignition of ethylene-air mixtures. In the present experiments, flow residence in the discharge is approximately 2-3 msec. From Figs. 5.29 and 5.31, it can be seen that for thermal ignition to occur during this time, flow temperature in the discharge has to be in the range of 1050-1150^0 C, which is twice as high as the temperature measured in ethylene-air flows, 500-600^0 C (see Fig 3.24). Also, ignition delay time at near autoignition temperature in a stoichiometric ethylene-air mixture, T=650^0 C, is greater than 1 sec (see Fig. 5.29(a)). On the other hand, ignition in the present experiments occurs at much shorter discharge durations, as short as 10 msec (see Section

3.1.7). These results suggest that thermal ignition at the conditions of the present experiments is very unlikely.

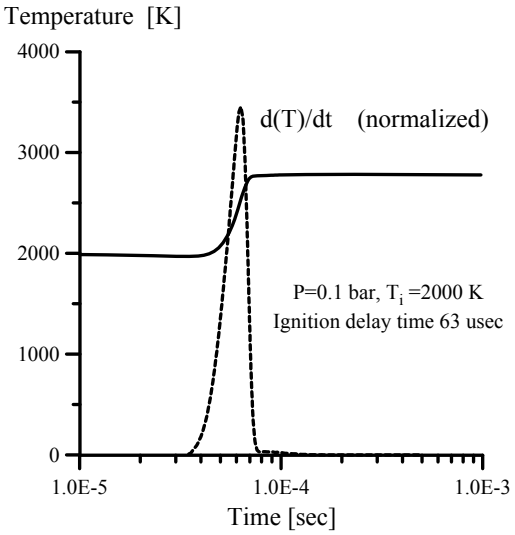

Figure 5.28: Ignition delay time in a stoichiometric ethylene-air mixture at P=0.1 bar, Ti=2000 K, calculated using Eq. (5.9).

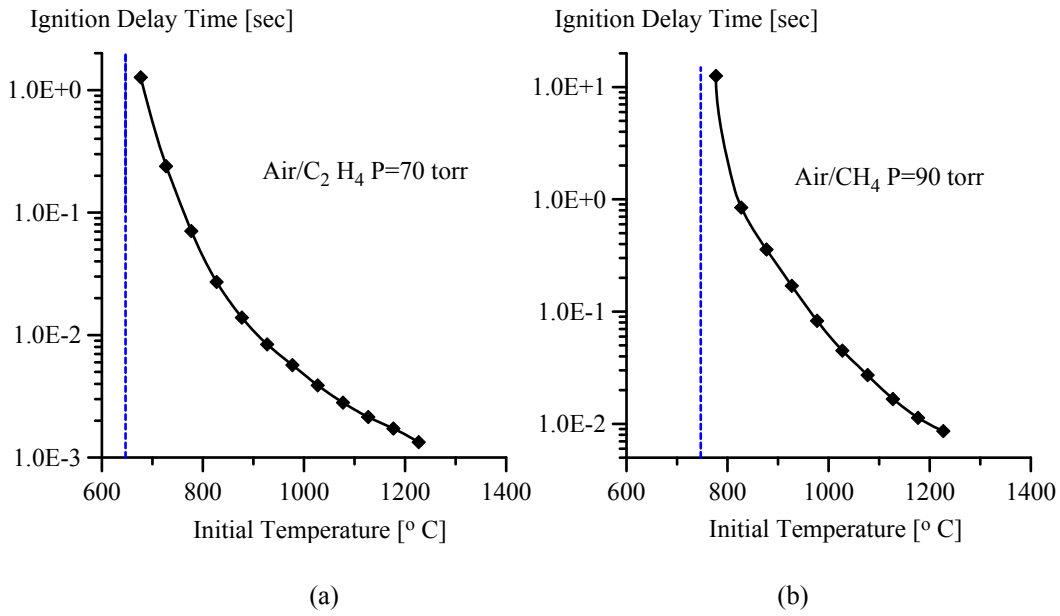

Figure 5.29: Ignition delay time in stoichiometric ethylene-air and methane-air mixtures vs. initial temperature at 70 torr and 90 torr, respectively. Autoignition limits are Tauto=650^0 C and Tauto=750^0 C, respectively.

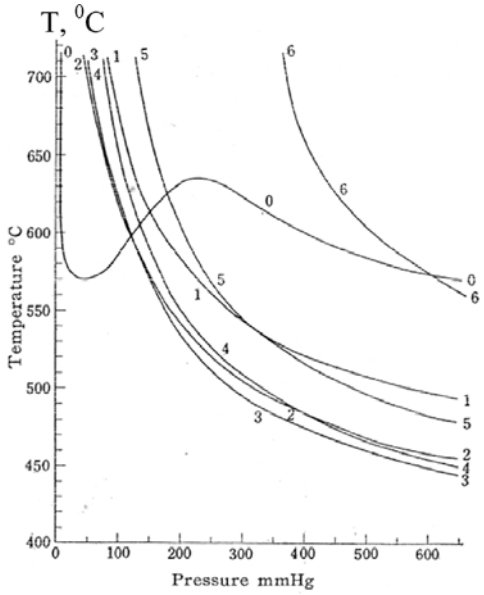

Figure 5.30: Autoignition temperatures of ethylene–air mixtures vs. initial pressure [23]. Curve 0—5% ethylene in air, 1—10, 2—20, 3—30, 4—40, 5—50, and 6—60%.

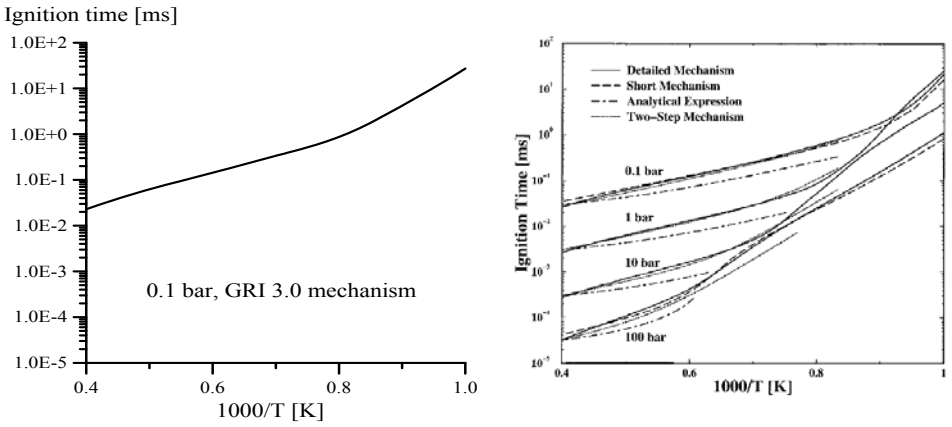

Figure 5.31: Comparison of ignition delay times calculated by the GRI-Mech 3.0 mechanism in the present work with the results of Ref. [3]. Stoichiometric ethylene-air mixture, P=0.1 bar.

5.2 Repetitively pulsed discharge modeling results

The kinetic model of hydrocarbon-air plasmas described in Section 4.3 and validated in Section 5.1 has been used to model the results of gaseous hydrocarbon ignition experiments discussed in Section 3.1.6. For all subsequent modeling calculations, a simplified model (i.e. without charged species kinetics), as discussed in Section 5.1.1, has been used.

5.2.1 Repetitively pulsed discharge in air

The model was used to simulate a repetitively pulsed discharge in dry air at the following conditions: CPT pulse generator, mass flow rate $\dot{m}$ =0.8 g/sec, pulse repetition rate ν=50 kHz, initial temperature T=300 K, test section pressure P=70 torr, test section geometry and pulsed discharge parameters are as listed in Table 4.7. Peak pulse voltage used was 7.55 kV, an average value between two pulse voltages used in the single-pulse discharge calculations, 6.73 kV for P=60 torr and 8.36 kV for 80 torr, see Section 5.1.1. Peak electron density during the pulse was adjusted for the calculated pulse energy to be close to the experimentally measured value, 2.3 mJ (see Table 3.1). This corresponds to the peak pulse current in the mixture.inp input data file of 22.4 A. Figures 5.32 and 5.33 show the results of these calculations using the Lagrangian approach discussed in Section 4.1 (without averaging over the fluid particles). Therefore, these figures plot the temperature as well as O and O_3 mole fractions in a fluid particle vs. time. Figure 5.33 (b) shows a magnified part of Fig. 5.33 (a) for the first 0.3 msec, which shows O atom and ozone concentrations stepwise increase after every pulse. At these conditions, the total number of pulses every fluid particle experiences in the discharge is 121, and the time-

average discharge power, calculated using Eq. (4.16), is 115 W. The modeling calculations predict that 83 W is thermalized, with the rest stored in O atoms and ozone. At the end of the discharge region, the flow temperature increases up to 130^0 C, and the O atom mole fraction reaches 0.3%. This shows that, as expected, O atoms produced by individual discharge pulses are accumulated in the flow, due to their slow decay in a recombination reaction

$$O + O_2 + M \rightarrow O_3 + M \,, \tag{5.9}$$

which is responsible for a long O atom decay time, ≈2 msec (see Fig. 5.4).

Note that the flow temperature rise predicted by the model, up to 130^0 C, is somewhat less than measured in the experiment at these conditions, approximately $T=200^0$ C (see Fig. 3.24). This suggests that the discharge power at these conditions may be higher than the power based on the pulse energy measurements (see Section 3.1.1).

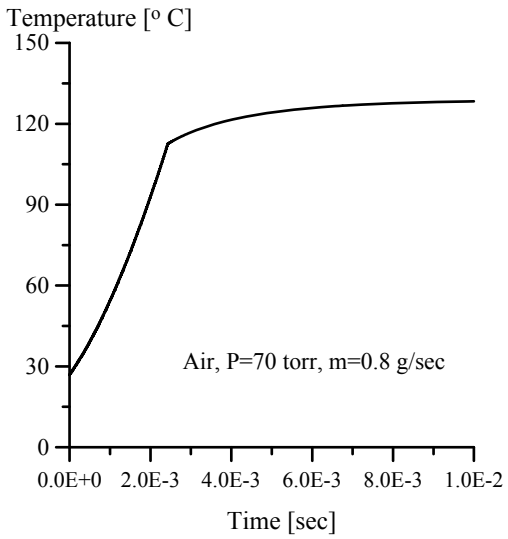

Fig 5.32: Fluid particle temperature in the repetitively pulsed discharge in air as a function of time. Air, P=70 torr, mass flow rate $\dot{m}$ =0.8 g/sec, pulse repetition rate ν=50 kHz, peak voltage U=7.55 kV, residence time in the discharge is 2.4 msec.

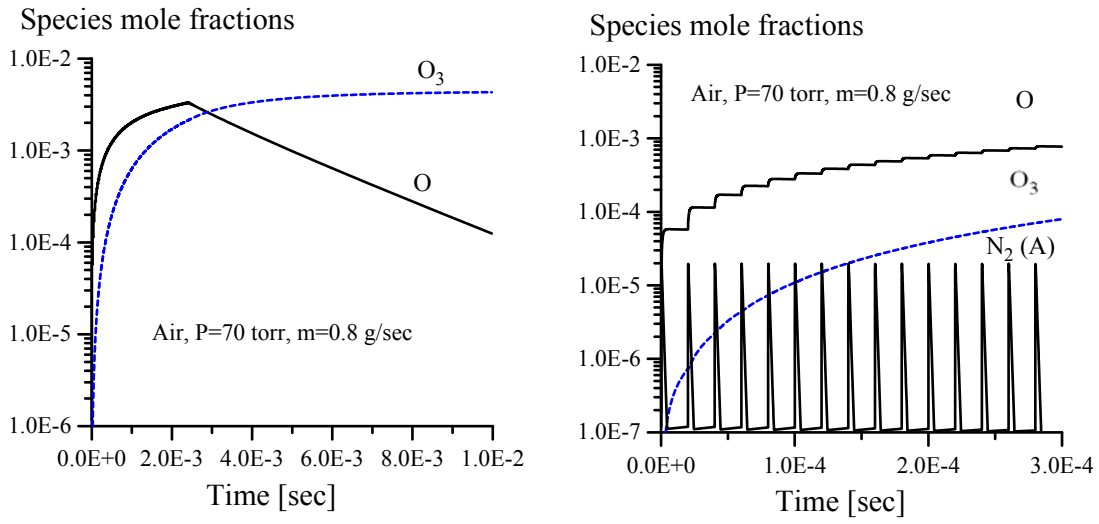

Fig 5.33: O atom, ozone, and $N_2(A)$ mole fractions in a fluid particle as functions of time, at the conditions of Fig. 5.32. (a) entire discharge and the afterglow, (b) near the discharge entrance.

Operating the code in the pulse-periodic regime, with ~100 high voltage pulses produced during a ~2 msec flow residence time in the discharge requires long computation time (up to several hours). This is due to the fact that the duty cycle of the pulsed discharge is very low, ~1/1000. Resolving nanosecond duration voltage pulses and following chemical kinetic processes on a ~100 μsec scale between the pulses requires repeatedly changing the time step by several orders of magnitude.

In addition, the results of the pulsed-periodic discharge modeling need to be averaged over a number of fluid particles with different initial coordinates (see Eq. (4.19)). In fact, this averaging can be reduced to averaging of the high-voltage pulse waveform over an ensemble of pulses fired at different moments of times t_1, such as

$$\bar{n}_e(t) = \frac{1}{t_3}\int_0^{t_3} n_{e0}\cdot\exp\left[-\left(\frac{t-t_1}{t_2}\right)^2\right]dt_1 = \frac{1}{t_3}\int_t^{t_3+t} n_{e0}\cdot\exp\left[-\left(\frac{\tau_1}{t_2}\right)^2\right]d\tau\,, \qquad (5.10)$$

where $\tau = t - t_1$, n_{e0} is peak electron density, t_2 is the pulse width, and t_3 is the pulse repetition period. Eq. (5.10) can be solved easily when $t_2 << t_3$,

$$\overline{n}_e(t) \approx \frac{n_{e0}}{t_3} \int_{-\infty}^{+\infty} \exp(-x^2) dx = \sqrt{\pi} \cdot \frac{t_2}{t_3} \cdot n_{e0} \sim 1.33 \cdot 10^{-3} \cdot n_{e0} . \quad (5.11)$$

Therefore the fluid particle averaging reduces a pulse-periodic discharge excitation to continuous excitation, with the constant in time electron density $\overline{n}_e$, proportional to the peak electron density during the pulse, n_{e0}, times the pulsed discharge duty cycle, t_2/t_3.

This operation converts the Lagrangian description of the flow into the Eulerian description. After this averaging, fluid particle parameters as functions of the location at time *t* are converted into the steady-state flow parameters, expressed as functions of the axial distance *x*. Note that the operation described above allows running the code for the continuous excitation discharge, instead of the pulsed-periodic discharge with subsequent averaging of the results. This approach reduces the computational time by about a factor of 100. Figure 5.34 compares the discharge current for the pulse-periodic excitation and for the continuous excitation. The peak current for the first model is 21 A, and the steady-state current for the second model is 0.021 A. To validate this approach, the modeling results for the pulse-periodic discharge in air (without averaging) have been compared to the results for the continuous excitation. Figures 5.35 and 5.36 compare the flow temperature, the O atom mole fraction, and the O_3 mole fraction vs. axial distance for these two models. It can be seen that the results are very close, except for the fine scale pulse structure for the pulse-periodic excitation. This demonstrates the applicability of the continuous excitation approach. All subsequent modeling calculations have been done using the continuous excitation model.

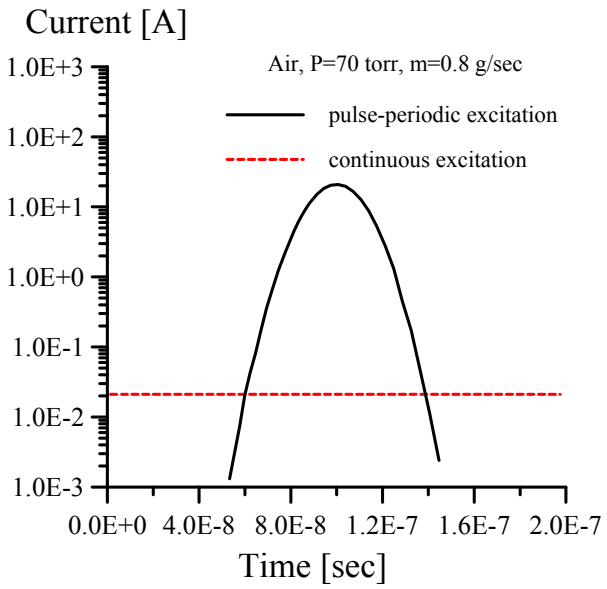

Fig 5.34: Discharge current for pulse-periodic and continuous excitation models. Peak current for the pulse-periodic model is 21 A. Continuous excitation current is 0.021 A.

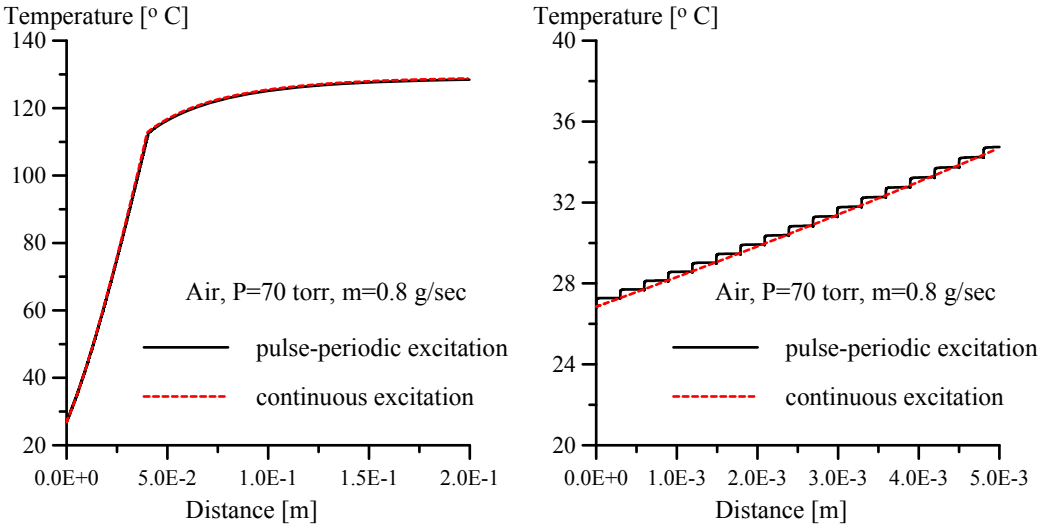

Fig 5.35: Flow temperatures calculated for pulse-periodic and continuous excitation models. Air, P=70 torr, $\dot{m}$ =0.8 g/sec, ν=50 kHz, U=7.55 kV, pulse-periodic and continuous excitation current are the same as in Fig. 5.32.

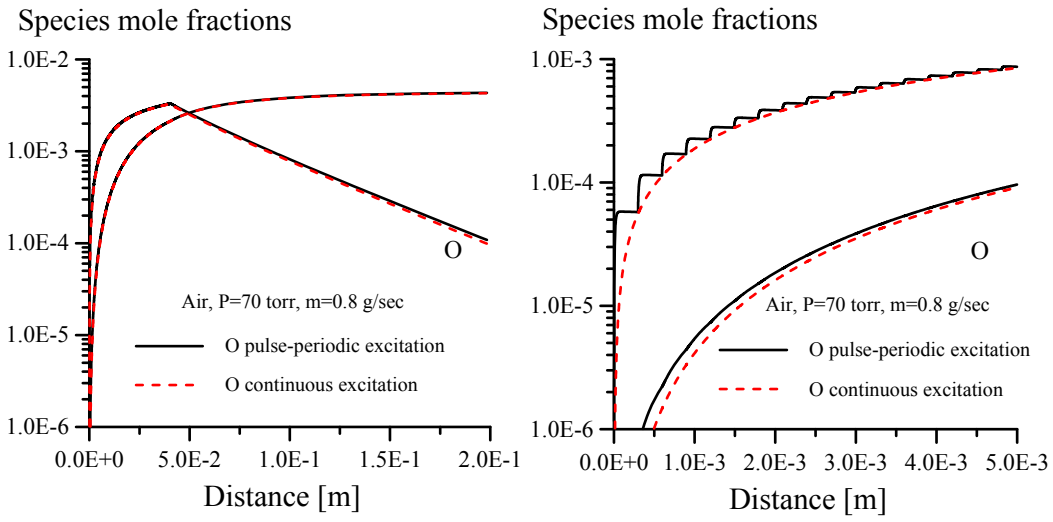

Fig 5.36: O atom mole fractions calculated for pulse-periodic and continuous excitation models at the conditions of Fig. 5.32.

5.2.2 Repetitively pulsed discharge in ethylene-air

The results of calculations for the repetitively pulsed discharge in a stoichiometric ethylene-air flow are shown in Figs. 5.37-5.39. The flow and discharge conditions are P=70 torr, mass flow rate $\dot{m}$ =0.8 g/sec, and pulse repetition rate ν=50 kHz, which corresponds to the present experimental conditions (see Section 3.1.6). The pulse peak voltage and the discharge power are the same as in the air discharge, 7.55 kV and 115W, and the constant electron density corresponds to the continuous excitation current of 0.021 A. Figure 5.37 compares flow temperature distributions in air and in a C_2H_4-air mixture at the same flow and plasma conditions. It can be seen that the temperature in the C_2H_4-air flow is significantly higher than in air. However, the peak temperature in the C_2H_4-air flow is 260^0 C, considerably lower than the experimental value at these conditions, 550^0 C (see Fig. 3.24). Also, unlike in the experiment, no ignition occurs in the computational domain, either in the discharge or in the afterglow. At these conditions,

a fluid particle in the discharge experiences 102 pulses. The input discharge power and the thermalized power are 115 W and 193 W, respectively. Note that in the C_2H_4-air mixture, the thermalized power is significantly higher than the input discharge power. This occurs due to the additional energy release in plasma chemical fuel oxidation reactions (compare this result with the result for a single-pulse discharge in C_2H_4-air, see Fig. 5.24). However, this additional heat release predicted by the model is not sufficient to significantly accelerate fuel oxidation and to produce ignition.

Figure 5.38 shows fuel mole fraction in the mixture at these conditions. It can be seen that the fuel fraction in the discharge decreases from 6.5% mole fraction to 6.0% mole fraction, by only 7.7%. This reduction is much less than measured in the experiment at these conditions, about 90% (see Fig. 3.24). One can also see that no significant additional fuel oxidation occurs downstream of the discharge (see Fig. 5.38), i.e. plasma chemical fuel oxidation does not become a self-sustained process.

Figure 5.39 shows product species and radical species mole fractions in the discharge and in the afterglow. It can be seen that product species (CO, CO_2, H_2O, and CH_2O) fractions all increase in the discharge but rapidly reach stationary values in the afterglow. Also, radical species (O, H, OH, CH_3 and HO_2) fractions in the afterglow rapidly decrease (see Fig. 5.39). Basically, the flow temperature and the radical concentrations at the discharge exit are far too low to sustain further oxidation and to produce ignition.

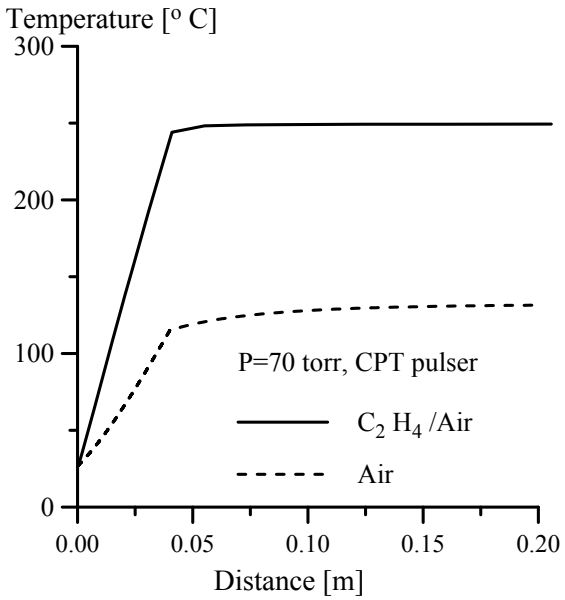

Figure 5.37: Flow temperature distributions in the repetitively pulsed discharges in air and in stoichiometric ethylene-air flow. Air, P=70 torr, $\dot{m}$ =0.8 g/sec, ν=50 kHz, U=7.55 kV.

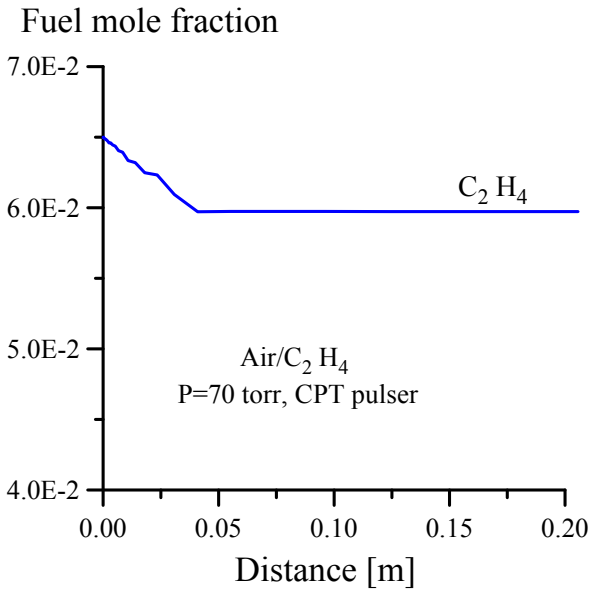

Figure 5.38: Ethylene mole fraction distribution at the conditions of Fig. 5.37

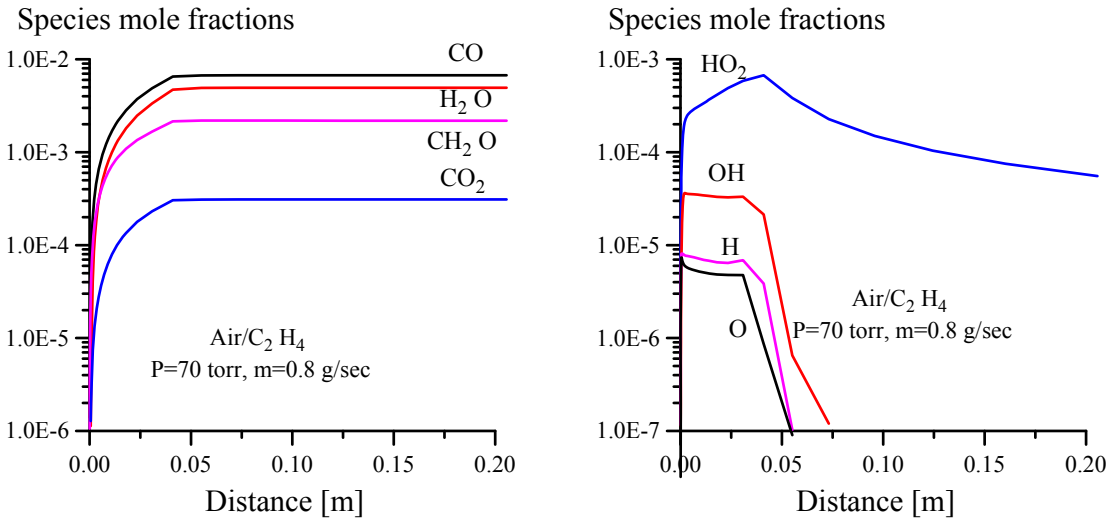

Figure 5.39: Product species fractions (left) and radical species fractions (right) at the conditions of Fig. 5.37.

5.2.3 Repetitively pulsed discharge in methane-air

The modeling calculation results for a repetitively pulsed discharge in a stoichiometric methane-air flow are shown in Figs 5.40-5.42. The flow and plasma conditions are P=90 torr, $\dot{m}$ =0.8 g/sec, and ν=50 kHz, which corresponds to the present experimental conditions (see Section 5.1.6). The pulse peak voltage is 9.17 kV, extrapolated from peak voltages at P=60 torr and 80 torr, and the constant electron density corresponds to the continuous excitation current of 0.018 A (discharge power of 120 W). The results are similar to ethylene-air results (see Section 5.2.2). Figure 5.40 shows temperature distributions in the discharge in air and in the methane-air mixture. It can be seen that the peak temperature in the methane-air flow, T=190^0 C, is considerably lower than in the experiment, 440^0 C (see Fig. 3.27). Figures 5.41 and 5.42 show fuel, product species, and radical species mole fractions in the discharge and in the afterglow. Again, the methane mole fraction reduction is very small, about 2.2% (see Fig. 5.41), which is much less than the experimental result (about 90% fuel oxidation, see Fig. 3.27).

Due to a slower methane oxidation, combustion product concentrations are lower than in C_2H_4-air mixture, (compare Figs. 5.39 and 5.42). The input discharge power and the thermalized power are 120 W and 141 W, respectively, i.e. a modest additional heat release due to plasma chemical reactions is observed. However, no ignition occurred in the entire computational domain.

Summarizing, the present kinetic model, validated using O atom concentration measurements in single-pulse discharges in air, methane-air, and ethylene-air, does not predict significant fuel oxidation or ignition, observed in the present experiments.

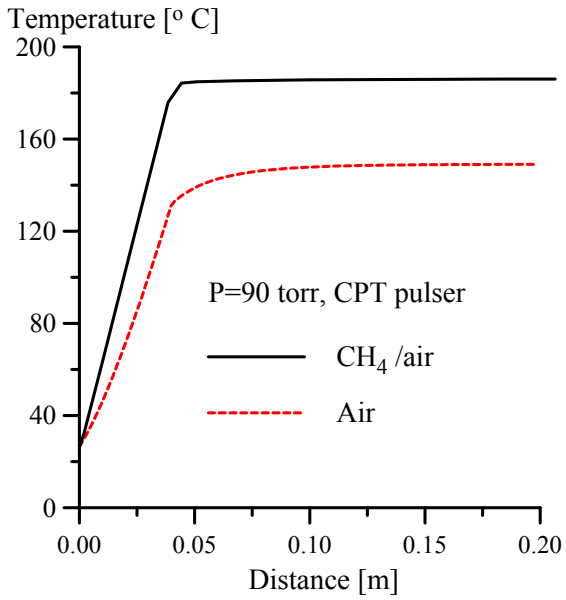

Figure 5.40: Flow temperature distribution in repetitively pulsed discharges in air and in a stoichiometric methane-air flow. P=90 torr, $\dot{m}$ =0.8 g/sec, Φ=1.0, ν=50 kHz, U=9.17 kV.

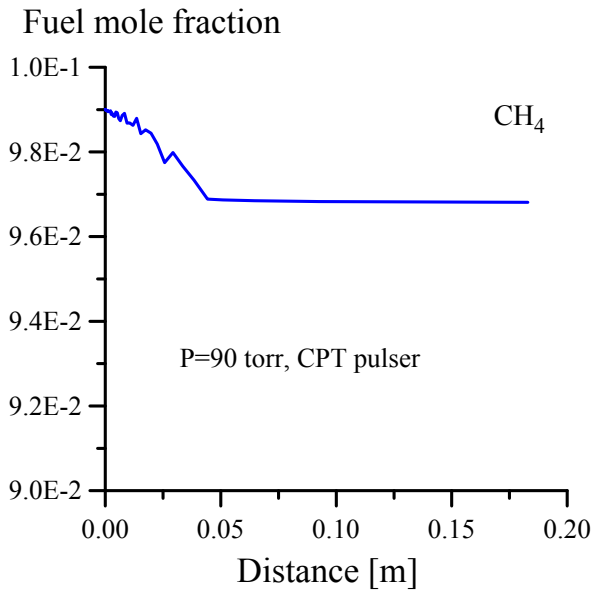

Figure 5.41: Methane mole fraction distribution at the conditions of Fig. 5.40

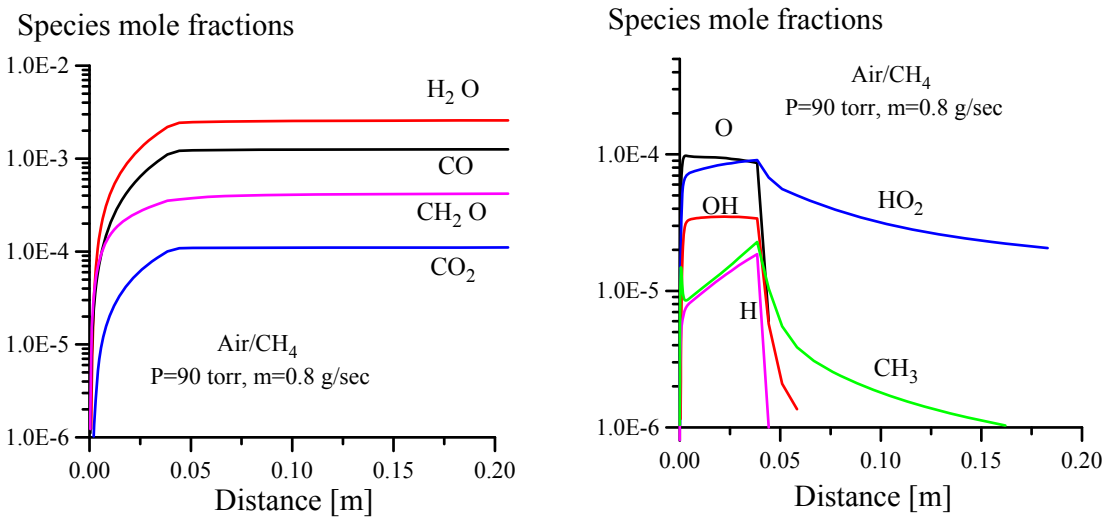

Figure 5.42: Product species fractions (left) and radical species fractions (right) at the conditions of Fig. 5.40.

5.3 Ignition of an ethylene-air flow at higher discharge power

The results of modeling calculation discussed in Section 5.2 show that flow temperatures in fuel-air mixtures predicted by the model are much lower than in the experiment, fuel oxidation is less than in the experiment, and ignition is not achieved, unlike in the experiment. The question is, how high does the discharge power need to be to produce ignition in the discharge or in the afterglow? For this, discharge power was increased by varying the time-averaged discharge current, which is equivalent to varying the pulse peak current (see discussion in Section 5.2). The results are summarized in Figs. 5.43-5.45. Figure 5.43 shows temperature distributions for the pulse peak current value of 50A (discharge power of 275 W). From Fig. 5.43, it can be seen that in this case ignition occurs downstream of the discharge, at the axial distance of 80 cm. At these conditions, the temperature in the discharge reaches 520^0 C, which is close to the experimental value of 580^0 C, also shown in Fig. 5.43. For comparison, Figure 5.43 shows axial temperature distribution in air, at the same discharge power of 275 W. It can be seen that the predicted air flow temperature in the discharge is 260^0 C, again close to the experimental value of 230^0 C (see Fig. 5.43). The fact that the temperatures in air and in fuel-air flows, predicted by the model, are in good agreement with the experimental results, suggests that the discharge power in the present experiments might be considerably higher than the result based on the pulse energy measurements (see Section 3.1.1). Note that although the model predicts ignition at x=0.8 m, in the experiment the flame front could move upstream, into the test section, due to a flashback propagation through the boundary layer where the flow velocity is low.

Figures 5.44 and 5.45 show species concentration distributions at the conditions of Fig. 5.43, at I_{peak}=50 A and discharge power of 275 W. From Figures 5.43-5.45, it can be seen that additional heating of the fuel-air flow in the discharge, compared to the air flow ($T=520^0$ C vs. $T=260^0$ C) occurs due to plasma chemical fuel oxidation generating additional energy release (compare Fig.5.43 with Fig. 5.24). After that, ignition downstream of the discharge is purely thermal, since excited species and most radicals produced in the discharge rapidly decay. However, the role of plasma chemical oxidation is to heat the flow to the temperature approaching autoignition temperature. In other words, plasma chemical fuel oxidation "open the door" to thermal ignition. The modeling calculation results demonstrate that it occurs at the discharge power approximately 2.5 times higher than the measured power, which suggests a significant uncertainty in pulse energy measurements.

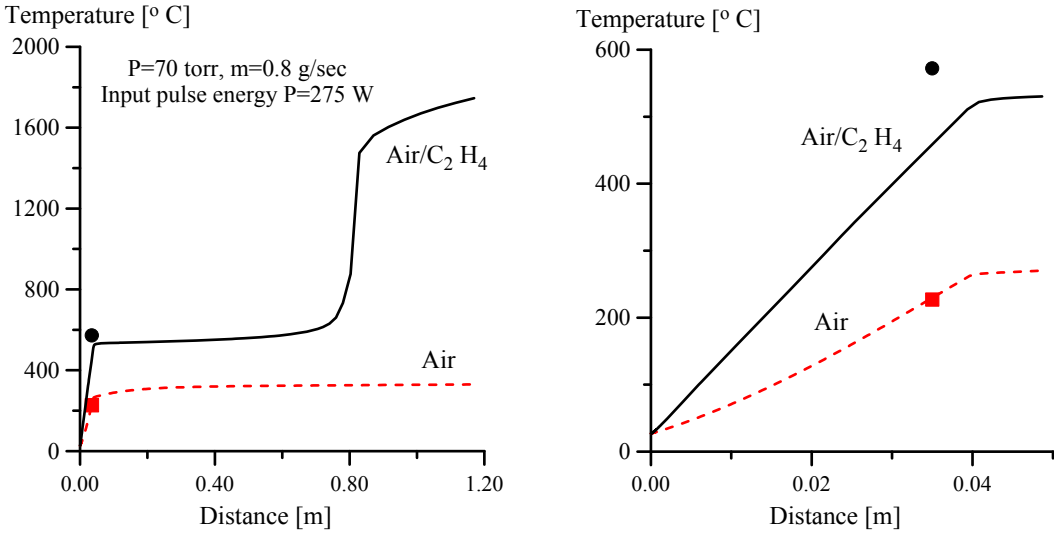

Figure 5.43: Flow temperature distributions in the discharge and in the afterglow, for a higher discharge power of 275 W. Stoichiometric ethylene-air mixture, P=70 torr, $\dot{m}$ =0.8 g/sec, ν=50 kHz, U=7.55 kV, discharge length 4 cm. Experimentally measured temperatures are shown for comparison.

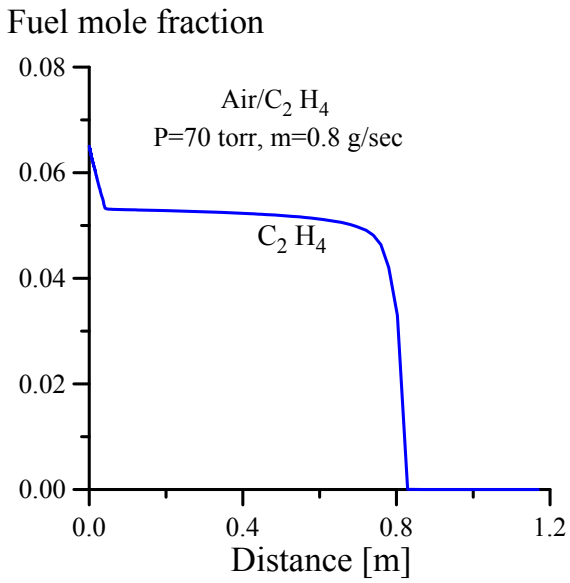

Figure 5.44: Fuel mole fraction at the conditions of Fig. 5.43 (I_{peak}=50 A).

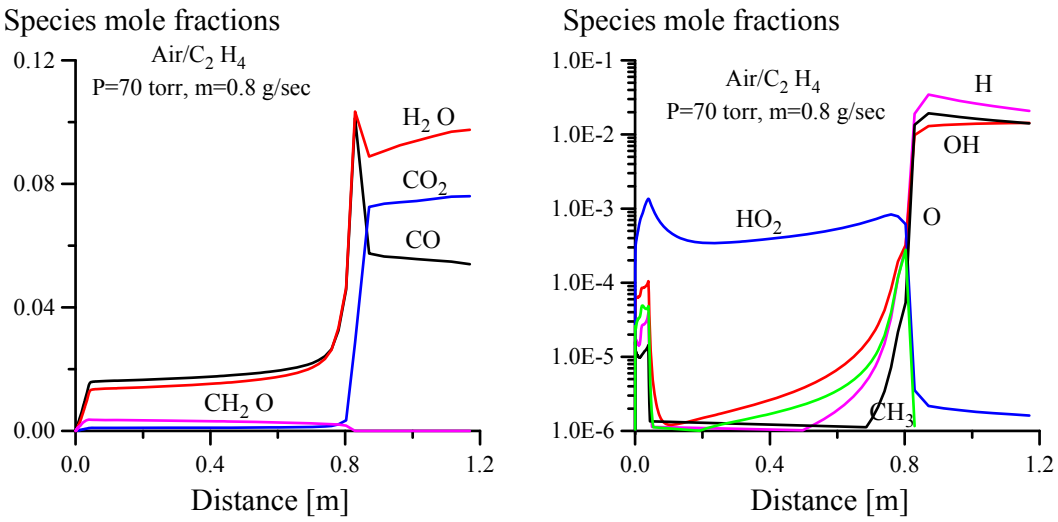

Figure 5.45: Combustion product mole fractions (left) and radical species mole fractions (right) at the conditions of Fig. 5.43 (Ipeak=50 A, discharge power 275 W).

5.4 Pulse-periodic discharge modeling using an alternative reaction mechanism

The results of modeling calculation discussed in Section 5.2 show that the model predictions are at variance with the experimental results, at the experimentally measured discharge power, 110W. In particular, the model predicts much less fuel oxidation in the

discharge and fails to predict ignition at the experimentally measured discharge power. Note that the low-temperature plasma chemical reaction model has been validated by comparison with O atom concentration measurement in a single-pulse discharge in air, methane-air, and ethylene-air (see Sections 5.1.1-5.1.3). On the other hand, GRI-Mech 3.0 reaction mechanism has been developed to reproduce experimental data in hydrocarbon flames, such as ignition delay times (see Section 5.1.4). This means that GRI-Mech 3.0 mechanism may not be applicable for modeling of chemical reaction in hydrocarbon-air mixtures at near room temperatures.

Although determining applicability of GRI-Mech 3.0 mechanism for low-temperature hydrocarbon-air kinetics is beyond the scope of the present work, one series of modeling calculations has been conducted to test its applicability. In this test, GRI-Mech 3.0 reaction mechanism has been replaced by an alternative reaction mechanism developed by A. Konnov [65, 66]. This reaction mechanism has been developed to reproduce experimental data in low-temperature (e.g. fuel lean) flames.

Figures 5.46 and 5.47 compare the thermalized pulse energy and stable product mole fractions in a single-pulse discharge produced by a CPT pulser in a stoichiometric ethylene-air mixture at a pressure of P=60 torr. It can be seen that GRI-Mech 3.0 mechanism predicts thermalized energy of 3.4 mJ, compared to 2.6 mJ predicted by the Konnov mechanism. In addition, the product species mole fractions predicted by the Konnov mechanism significantly differ from the GRI-Mech 3.0 kinetic mechanism predictions (see Fig. 5.47). In particular, mole fractions of CO, CO_2, CH_2O and H_2O predicted by the Konnov mechanism are significantly less than predicted by the GRI-Mech 3.0 mechanism.

Figures 5.48-5.50 compare the flow temperature and species concentrations in a repetitively pulsed discharge in a stoichiometric ethylene-air mixture at the conditions of Fig. 5.37 (P=70 torr, $\dot{m}$ =0.8 g/sec, ν=50 kHz, U=7.55 kV, discharge power 115 W), using these two reaction mechanisms. From Figs. 5.48 to 5.50, it can be seen that there is a significant difference between the two model predictions. In particular, the GRI-Mech mechanism predicts a 30^0 C higher flow temperature rise than Konnov mechanism (see Fig. 5.48). The predicted fuel oxidation fractions for the two mechanisms are very close (see Fig. 5.49). However, the Konnov mechanism predicts far less CO, CO_2 and H_2O generation and somewhat higher CH_2O generation by the plasma (see Fig. 5.50). These differences between the two mechanisms' predictions suggest that the low-temperature chemical reaction mechanism in hydrocarbon-air mixtures might be not completely understood and that neither of these two mechanisms may adequately describe plasma chemical reactions at near room temperature.

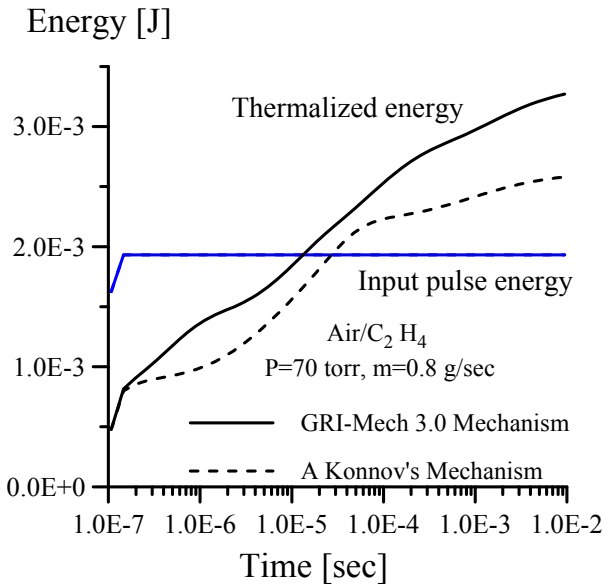

Fig 5.46: Comparison of thermalized pulse energies for the GRI-Mech 3.0 (solid line) mechanism and the Konnov mechanism (dashed lines) in a single-pulse discharge in a stoichiometric ethylene-air mixture (P=60 torr, CPT pulser, Φ=1, U=6.73 kV).

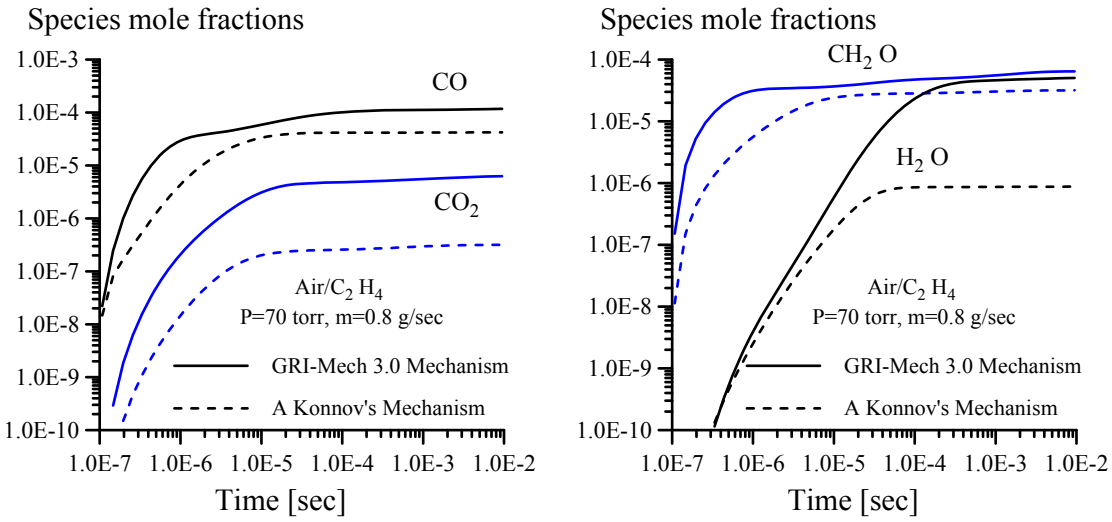

Fig 5.47: Comparison of species mole fractions for the GRI-Mech 3.0 (solid lines) mechanism and the Konnov mechanism (dashed lines) in a single-pulse discharge in a stoichiometric ethylene-air mixture (P=60 torr, CPT pulser, Φ=1, U=6.73 kV).

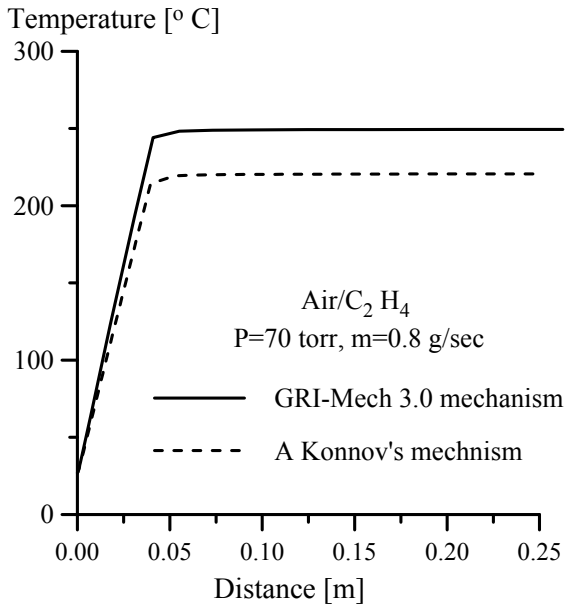

Fig 5.48. Comparison of flow temperature distributions for the GRI-Mech 3.0 mechanism (solid line) and the Konnov mechanism (dashed line) in a stoichiometric ethylene-air mixture, at the conditions of Fig. 5.37.

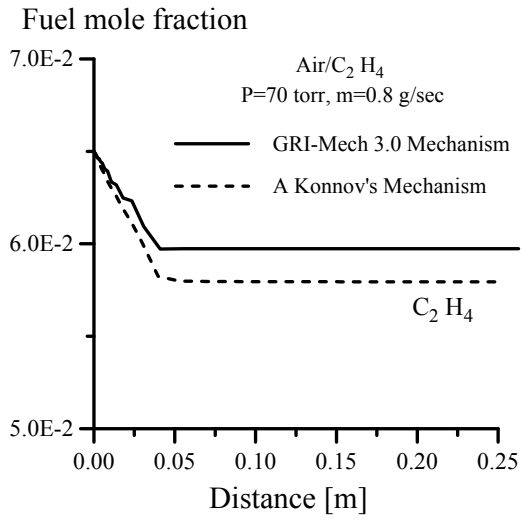

Fig 5.49: Comparison of fuel mole fraction distributions for for the GRI-Mech 3.0 mechanism (solid line) and the Konnov mechanism (dashed line) in a stoichiometric ethylene-air mixture, at the conditions of Fig. 5.37.

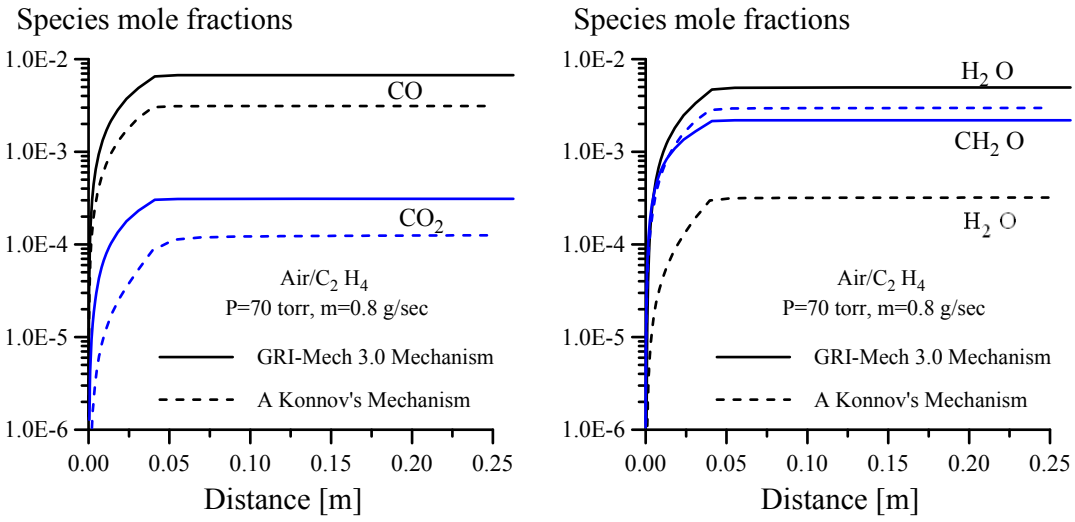

Fig 5.50: Comparison of stable product mole fractions distributions for for the GRI-Mech 3.0 mechanism (solid lines) and the Konnov mechanism (dashed lines) in a stoichiometric ethylene-air mixture, at the conditions of Fig. 5.37.

CHAPTER 6

CONCLUSIONS AND FUTURE WORK

The dissertation presents experimental and kinetic modeling studies of ignition of hydrocarbon-air flows by a high voltage, repetitively pulsed, nanosecond pulse duration plasma. This nonequilibrium plasma ignition method can be used at low pressures, high flow velocities, and in fuel lean mixtures, i.e. when common ignition approaches, such as spark and arc discharges, pilot flames, and hot surface igniters, are ineffective.

The repetitively pulsed, nanosecond pulse duration plasma offers two critical advantages compared with DC, AC, RF, and microwave discharge plasmas. First, short pulse duration, a few tens of nanosecond, greatly improves the plasma stability. The pulse duration is much shorter than characteristic time for ionization instability development, ~10^{-3}- 10^{-4} sec, and glow-to-arc transition. As a result, diffuse and volume-filling low-temperature plasmas can be operated at much higher pressures and power loadings. Second, the high reduced electric field, E/N, during the high-voltage pulses results in efficient ionization, electronic excitation, and dissociation of molecular species by electron impact, the rates of which have strong exponential dependence on E/N. This results in generation of large amounts of active radical species at a relatively low plasma power budget.

For the present experiments, a new nonequilibrium plasma combustion facility has been built at the Nonequilibrium Thermodynamics Laboratories at Ohio State University. In the present work, two different pulsed plasma generators, CPT and FID pulsers, have been used.

The CPT pulser generates high-voltage (16-18 kV), short pulse duration (20-30 nsec) pulses at high repetition rates (up to 50 kHz). Using this pulser to generate a plasma in premixed ethylene-air and methane-air flows resulted in flow ignition occurring at low air plasma temperatures, 200-300^0 C, inferred from nitrogen second positive band system spectra. The experiments showed that adding fuel to the air flow considerably increased the flow temperature in the plasma, up to 500-600^0 C. At these conditions, the reacted fuel fraction, measured by FTIR absorption spectroscopy, was up to 80%, and significant amounts of combustion products, CO, CO_2, and H_2O, were detected downstream of the discharge region. The experiments also showed significant methane and ethylene oxidation, with a resultant temperature rise, at conditions when there was no ignition and no flame detected in the test section. Adding ethylene to a nitrogen flow at the same conditions resulted in much less pronounced plasma temperature rise, only by $\Delta T=50^0$ C. Comparing this with the temperature rise in ethylene-air flows, $\Delta T=200\text{-}300^0$ C, this demonstrates that the temperature increase in the air-fuel plasma is due to plasma chemical fuel oxidation reactions, rather than due to excited species quenching. This suggests that low-temperature plasma chemical reactions can oxidize significant amounts of hydrocarbons and increase the temperature of air-fuel mixtures due to heat release in the exothermic fuel oxidation process. Ignition apparently occurs when the flow temperature becomes close to autoignition temperature, due to additional energy release

in plasma chemical reactions. Time-resolved and time-averaged visible emission spectroscopy demonstrated that repetitively pulsed nanosecond discharge generated radical species such as C_2, CH and CN in the plasma region and downstream of the plasma region, and produced self-sustained combustion downstream of the plasma region. Ignition experiments at different pulsed discharge durations showed that ignition was not due to a relatively slow process of flow heating by the electrodes. The present results also showed that plasma assisted ignition occurred at a low discharge power, ~1% of heat of combustion.

Experiments in hydrocarbon-air plasmas generated by the FID pulse generator (50 kV voltage, 5 nsec pulse duration, 100 kHz pulse repetition rate) did not result in ignition and produced very modest fuel oxidation (up to 10%). In these experiments, both air plasma temperature and temperature rise in air-fuel mixtures were significantly lower than for the CPT pulser at the same flow conditions, $T \approx 50^0$ C and $\Delta T \approx 50^0$ C, respectively. We conclude that a lower pulse energy coupled to the flow by the FID pulser resulted both in less flow heating and presumably in lower radical concentrations generated in the plasma, which resulted in a slower net rate of fuel oxidation.

Ignition experiments in liquid methanol-air and ethanol-air mixtures by a repetitively pulsed, nanosecond pulse duration plasma generated by the CPT pulser showed that preheating of the air flow up to $50\text{-}60^0$ C was critical for accelerating fuel evaporation and producing ignition. Ignition was achieved in both liquid fuels, and significant plasma temperature rise and fuel oxidation were detected. However, these results were not reproduced well, primarily due to poor liquid fuel injector nozzle performance.

A kinetic model was developed to simulate plasma assisted ignition of hydrocarbon-air mixtures by a repetitively pulsed, nanosecond pulse duration, low-temperature plasma. The model incorporated air plasma processes (electron impact ionization, dissociation, and electronic excitation of air species, reactions of electronically excited molecules and atoms, electron-ion recombination, ion-ion neutralization, electron attachment and detachment, and ion-molecule reactions), electron impact dissociation of fuel species, fuel dissociation by collisions with electronically excited nitrogen and GRI-Mech 3.0 mechanism of hydrocarbon oxidation. The model was validated by comparing with O atom concentration measurements by Two-Photon Absorption Laser-Induced Fluorescence (TALIF) in single-pulse discharges in air, methane-air, and ethylene-air, showing good agreement. Kinetic modeling of a repetitively pulsed discharges at the present experimental conditions did not predict significant fuel oxidation or ignition in ethylene-air and in methane-air flows, at the measured discharge powers. The model predicts that ignition would occur only if the repetitively pulsed discharge power is 2.5 times higher than measured in the experiments. Comparing the model predictions for two different hydrocarbon oxidation mechanisms gives different results for product species mole fractions at the same plasma and flow conditions. Note that both reaction mechanisms used in the present work have been developed and validated for high-temperature hydrocarbon flame conditions. The difference between their predictions suggests that neither of them might be applicable at the low-temperature conditions (starting at room temperature) of the present experiments.

To provide better insight in the low-temperature plasma assisted ignition mechanism, further experimental work should focus on flow temperature measurements

with some spatial resolution (such as spontaneous Raman spectroscopy or CARS), rather than emission spectroscopy, which is a line-of-sight measurement. This would allow detection of possible "hot spots" which may form in the discharge at some conditions. Also, quantitative measurements of fuel oxidation products, such as CO, CO_2, CH_2O and H_2O are desirable. Further studies of plasma assisted liquid fuel ignition would require the use of a low mass flow rate fuel injector nozzle.

To understand kinetics of plasma assisted fuel oxidation in a repetitively pulsed, nanosecond pulse duration discharge, a truly low-temperature fuel oxidation reaction mechanism (applicable at room temperature) needs to be developed and validated. Validation of this reaction mechanism would also require further experimental measurements of species concentrations in the pulsed discharge, such as H atoms, OH, and CH_3.

BIBLIOGRAPHY

1. Glassman, I., "Combustion", Academic, San Diego, 1996

2. Cumpsty, N. A., "Jet Propulsion: A Simple Guide to the Aerodynamics and Thermodynamic, Design and Performance of Jet Engines", Cambridge University Press, New York, 1997

3. Varatharajan, B., and Williams, F. A., "Ethylene Ignition and Detonation Chemistry, Part 2: Ignition Histories and Reduced Mechanisms", Journal of Propulsion and Power, Vol. 18, No. 2, pp. 352-362, 2002

4. Ben-Yakar, A., and Hanson, R., "Cavity Flameholders for Ignition and Flame Stabilization in Scramjets: Review and Experimental Study," AIAA Paper 98-3122, 34th AIAA/ASME/SAE/ASEE Joint Propulsion Conference and Exhibit, Cleveland, OH, 1998

5. Curran, E. T., and Burthy, S. N. B., "Scramjet Propulsion", American Institute of Aeronautics and Astronautics, 2000

6. Petersen, E.L., Kalitan, D. M., and Rickard, M.J.A., "Reflected-Shock Ignition of SiH4/H2/O2/Air and SiH4/CH4/O2/Air Mixtures", Journal of Propulsion and Power, Vol. 20, No. 4, pp. 665-674, 2004

7. Maly, R., "Fuel Energy in Road Vehicles Powered by Spark Ignition Engines", Plenum, New York, 1984

8. Ronney, P. D., "Laser Versus Conventional Ignition of Flames", Optical Engineering, Vol. 33, No. 2, pp. 510-521, 1994

9. Starikovskaia, S. M., "Plasma Assisted Ignition and Combustion", Journal of Physics D: Applied Physics, Vol. 39, pp. 265-299, 2006

10. Starikovskii, A. Y, "Plasma Supported Combustion", Proceedings of the Combustion Institute, Vol. 30, pp. 2405-2417, 2005

11. Bozhenkov, S. A., Starikovskaya, S. M., and Starikovskii, A. Y., "Nanosecond Gas Discharge Ignition of H_2- and CH_4-Containint Mixtures", Combustion and Flame, Vol. 133, pp. 133-146, 2003

12. Starikovskaya, S. M., Kukaev, E. N., Kuksin, A. Y., Nudnova, M. M., and Starikovskii, A. Y., "Analysis of the Spatial Uniformity of the Combustion of a Gaseous Mixture Initiated by a Nanosecond Discharge." Combustion and Flame, Vol. 139, pp. 177–187, 2004

13. Anikin, N. B., Mintoussov, E. I., Pancheshnyi, S. V., Roupassov, D. V., Sych, V. E., and Starikovskii, A. Y. "Nonequilibrium Plasmas and Its Applications for Combustion and Hypersonic Flow Control", AIAA Paper 2003-1053, 41st AIAA Aerospace Sciences Meeting and Exhibit, Reno, NV, 2003

14. Mintoussov, E. I., Pancheshnyi, S. V., and Starikovskii, A. Y., " Propane-Air Flame Control by Non-Equilibrium Low-Temperature Pulsed Nanosecond Barrier Discharge", AIAA Paper 2004-1013, 42nd AIAA Aerospace Sciences Meeting and Exhibit, Reno, NV, 2004

15. Anikin, N. B., Starikovskaia, S. M., and Starikovskii, A. Y., "Oxidation of Saturated Hydrocarbons under the Effect of Nanosecond Pulsed Space Discharge", Journal of Physics D: Applied Physics, Vol. 39, pp. 3244-3252, 2006

16. Anikin, N. B., Starikovskaia, S. M., and Starikovskii, A. Y., "Oxidation of C_1-C_{10} Hydrocarbons in Stoichiometric and Lean Mixtures with Air and Oxygen under the Action of Nanosecond Discharge. AIAA paper 2005-0601, 43rd AIAA Aerospace Sciences Meeting and Exhibit, Reno, Nevada, 2005

17. Pilla, G., Galley, D., Lacosted, D. A., Lacas, F., Veynante, D., and Laux, C., "Influence of the Repetition Rate of a Nanosecond Pulsed Discharge on the Stabilization of a Turbulent Lean Premixed Flame", AIAA Paper 2006-3243, 37th AIAA Plasmadynamics and Lasers Conference, San Francisco, CA, 2006

18. Pancheshnyi, S., Lacoste, D. A., Bourdon, A., and Laux, C., "Ignition of Propane-Air Mixtures by a Sequence of Nanosecond Pulses", AIAA Paper 2006-3769, 37th AIAA Plasmadynamics and Lasers Conference, San Francisco, CA, 2006

19. Kim, W., Do, H., Mungal, M. G., and Cappelli, M. A., "Flame Stabilization Enhancement and NOx Production Using Ultra Short Repetitively Pulsed Plasma Discharges", AIAA Paper 2006-560, 44th AIAA Aerospace Sciences Meeting and Exhibit, Reno, NV, 2006

20. Kim, W., Do, H., Mungal, M. G., and Cappelli, M. A., "Investigation of NO Production and Flame Structure in Plasma Enhanced Premixed Combustion", Proceedings of the Combustion Institute, Vol. 31, No. 2, pp. 3319-3326, 2007

21. Chintala, N., Meyer, R., Hicks, A., Bao, A., Rich, J. W., Lempert, W. R., and Adamovich, I. V., “Non-thermal Ignition of Premixed Hydrocarbon-Air Flows by Nonequilibrium RF Plasma”, Journal of Propulsion and Power, Vol. 21, No. 4, pp. 583-590, 2005

22. Chintala, N., Bao, A., Lou, G., and Adamovich, I. V., "Measurements of Combustion Efficiency in Nonequilibrium RF Plasma Ignited Flows", Combustion and Flame, Vol. 144, No. 4, pp. 744-756, 2006

23. Suga, M., “Studies on Explosive Reaction of Ethylene Mixed with Oxygen or Air: I. Explosion Limit at Low Pressure”, Journal of Chemical Society of Japan, Vol. 31, No. 5, pp. 515-521, 1958

24. Ombrello, T., Qin, X., Ju, Y., Gangoli, S., Gutsol, A., and Fridman, A., “Non-Equilibrium Plasma Discharge: Characterization and Effect on Ignition”, AIAA Paper 2006-1214, 44th AIAA Aerospace Sciences Meeting and Exhibit, Reno, NV, 2006

25. Ombrello, T., Ju, Y., Gangoli, S., Gutsol, A., and Fridman, A., “Ignition Enhancement Using Magnetic Gliding Arc”, AIAA Paper 2007-1025, 45th AIAA Aerospace Sciences Meeting and Exhibit, Reno, NV, 2007

26. Leonov, S. B., and Yarantsev, D. A., “Plasma-Induced Ignition and Plasma-Assisted Combustion in High-Speed Flow”, Plasma Sources Science and Technology, Vol. 16, pp. 132-138, 2007

27. Leonov, S. B., Yarantsev, D. A., Napartovich, A. P., and Kochetov, I. V., “Plasma-Assisted Combustion of Gaseous Fuel in Supersonic Duct”, IEEE Transactions on Plasma Science, Vol. 34, No. 6, pp. 2514-2525, 2006

28. Raizer, Y. P., “Gas Discharge Physics”, Springer, Berlin, 1991

29. Nishihara, M., Rich, J. W., Lempert, W. R., Adamovich, I. V., and Gogineni, S., “Low-Temperature M=3 Flow Deceleration by Lorentz Force”, Physics of Fluids, Vol. 18, No. 8, pp. 86-101, 2006

30. Hicks, A., Norberg, S., Shawcross, P., Lempert, W. R., Rich, J. W., and Adamovich, I. V., “Singlet Oxygen Generation in a High Pressure Non-Self-Sustained Electric Discharge”, Journal of Physics D: Applied Physics, Vol. 38, pp. 3812-3824, 2005

31. Anderson, J. D., “Modern Compressible Flows”, McGraw-Hill, New York, 2003

32. http://www.nist.gov/chemistry. Databases of National Institute of Standards and Technology

33. Anikin, N. B., "Experimental Study of Electrodynamics Characteristics of a High Speed Ionization Wave in Molecular Gases", Ph.D. Dissertation (in Russian), Moscow Institute of Physics and Technology, Moscow, Russia, 2000

34. Nishihara, M., "Low-Temperature Supersonic Flow Control Using Repetitively Pulsed MHD Force", Ph.D. Dissertation, The Ohio State University, 2006

35. Herzberg, G., "Molecular Spectra and Molecular Structure: I Spectra of Diatomic Molecules", Van Hostrand Reinhold Company, New York, 1950

36. Roux, F., Michaud, F., and Vervloet, M., "High Resolution Fourier Spectrometry of $^{14}N_2$ Violet Emission Spectrum: Extensive Analysis of the $C_3\Pi_u$-$B_3\Pi_g$ System", Journal of Molecular Spectroscopy, Vol. 158, pp. 270-277, 1993

37. Budo, A., "Intensitatsformeln fur die Triplettbanden", Zeitschrift fue Physik, Vol. 105, pp. 570-587, 1937

38. Belikov, A. E., Sharafutdinov, R. G., and Strekalov, M. L., "Temperature Dependence of Rotational Relaxation Time in Nitrogen", Chemical Physics Letters, Vol. 231, pp. 444-448, 1994

39. Bennett, W. R., and Flint, J., "$Ar(^3P_2)$ $-N_2(C^3\Pi_u)$ Excitation Transfer Cross Section and Radiative Lifetimes of the Nitrogen-Molecular-Laser Transitions", Physics Review A, Vol. 18, pp. 2527-2532, 1978

40. Barreta, L. G., da Rocha, C. J., Carinhana, D., Sbampato, M. E., de Oliveira, A. C., dos Santos, A. M., and dos Santos, L. R., "Emission Spectroscopy of CH Radical to Determine the Temperature of Ethanol Flame", Proceedings of XXVI Brazilian National Meeting in Condensed Matter Physics, Caxambu, Brazil, 2003

41. Carinhana, D., Barreta, L. G., da Rocha, C. J., dos Santos, A. M., and Bertran, C. A., "Determination of Gas Liquefied Petroleum Flame Temperatures Using Emission Spectroscopy", Proceedings of XXIX Brazilian National Meeting in Condensed Matter Physics, San Lorenzo, Brazil, 2006

42. Huber, K. P., and Herzberg, G., "Molecular Spectra and Molecular Structure IV: Constants of Diatomic Molecules", Van Nostrand, New York, 1979

43. Kovacs, I., "Rotational Structure in the Spectra of Diatomic Molecules", Elsevier, New York, 1969

44. Umemoto, H., "Production Yields of H(D) Atoms in the Reactions of $N_2(A^3\Sigma_u^+)$ with C_2H_2, C_2H_4, and Their Deuterated Variants", The Journal of Chemical Physics, Vol. 127, 014304, 2007

45. Fresnet, F., Baravian, G., Magne, L., Pasquiers, S., Postel, C., Puech, V., and Rousseau, A., "Kinetic of the NO Removal by Nonthermal Plasma in $N_2/NO/C_2H_4$ Mixtures", Applied Physics Letter, Vol. 77, No. 25, pp. 4118-4120, 2000

46. Thomas, J.M., Kaufman, F., and Golde, M., "Rate Constants for Electronic Quecheing of $N_2(A^3\Sigma_u^+, v=0\text{-}6)$ by O_2, NO, CO, N_2O, and C_2H_4", Journal of Chemistry Physics, Vol. 86, No. 12, pp. 6886-6892, 1987

47. Uddi, M., Jiang, N., Frederickson, K., Mintoussov, E., Adamovich, I. V., and Lempert, W. R., "Oxygen Atom Measurements in a Nanosecond Pulse Discharge by Two Photon Absorption Laser Induced Fluorescence", AIAA Paper 2007-4027, 38th AIAA Plasmadynamics and Lasers Conference, Miami, FL, 2007

48. Grekhov, I. V., Korotkov, S. CV., Stepaniants, A. L., Khristyuk, D. V., Koronkov, V. B., and Aristov, Y. V., "High-Power Semiconductor-Based Nano and Subnanosecond Pulse Generator with a Low Delay Time", IEEE Transactions on Plasma Science, Vol. 33, pp. 1240-1244, 2005

49. Macheret, S. O., Shneider, M. N., and Murray, R. C., "Ionization in Strong Electric Fields and Dynamics of Nanosecond Pulse Plasma", Physics of Plasmas, Vol. 13, 023502, 2006

50. Kee, R. J., Rupley, F. M., and Miller, J.A., "Chemkin-II: A FORTRAN Chemical Kinetics Package for the Analysis of Gas Phase Chemical Kinetic", Sandia Report, SAND89-8009B UC-706, 1994

51. Huxley, L. G. H., and Crompton R. W., "The Diffusion and Drift of Electrons in Gases", Wiley, New York, 1973

52. Itikawa, Y., Hayashi, M., Ichimura, A., Onda, K., Sakimoto, K., Takayanagi, K., Nakamura, M., Nishimura, M., and Takayanagi, T., "Cross Sections for Collisions of Electrons and Photons with Nitrogen Molecules", Journal of Physical and Chemical Reference Data, Vol. 15, No. 3, pp. 985-1010, 1986

53. Itikawa, Y., Ichimura, A., Onda, K., Sakimoto, K., Takayanagi, K., Hatano, Y., Hayashi, M., Nishimura, H., and Tsurubichi, S., "Cross Sections for Collisions of Electrons and Photons with Oxygen Molecules", Journal of Physical and Chemical Reference Data, Vol. 18, No. 1, pp. 23-42, 1989

54. Kossyi, I. A., Kostinsky, A. Y. Matveyev, A. A., and Silakov, V. P., "Kinetic Scheme of the Non-Equilibrium Discharge in Nitrogen-Oxygen Mixtures", Plasma sources Science and Technology, Vol. 1, pp. 207-220, 1992

55. http://www.me.berkeley.edu/gri_mech/version30/text30.html, GRI-Mech 3.0

56. Motlagh, S., and Moore, J., "Cross Sections for Radicals from Electron Impact on Methane and Fluoroalkanes", Journal of Chemical Physics, Vol. 109, No. 2, pp. 432-438, 1998

57. Janev, R. K., and Reiter, D., "Collision Processes of $C_{2,3}H_y$ and $C_{2,3}H_y^+$ Hydrocarbons with Electrons and Protons", Physics of Plasmas, Vol. 11, No. 2, pp. 781-829, 2004

58. Golde, M. F., Ho, G. H., Tao, W., and Thomas, J. M., "Collision Deactivation of $N_2(A^3\Sigma_u^+$. v=0-6) by CH_4, CF_4, H_2, H_2O, CF_3CL, and CF_2HCL", Journal of Physical Chemistry, Vol. 93, pp. 1112-1118, 1989

59. Piper, L., "Energy Transfer Studies on $N_2(X^1\Sigma_g^+$, v) and $N_2(B^3\Pi_g)$", Journal of Chemical Physics, Vol. 97, No. 1, pp. 270-275, 1992

60. Albugues, F., Birot, A., Blanc, D., Brunet, H., Galy, J., Millet, P., and Teyssier, J.L., "Destruction of the Levels $C^3\Pi_u$ (v′=0, v′=1) of Nitrogen by O_2, CO_2, CH_4, and H_2O", The Journal of Chemical Physics, Vol. 61, No. 7, pp. 2695-2699, 1974

61. Umemoto, H., Ozeki, R., Ueda, M., and Oku, M., "Reactions of $N_2(a'^1\Sigma_u^-)$ with H_2, CH_4, and Their Isotopic Variants: Rates Constants and the Production Yield of H(D) Atoms", Journal of Chemical Physics, Vol. 117, No. 12, pp. 5654-5659, 2002

62. Hindmarsh, A. C., "LSODE and LSODI, two new initial value ordinary differential equation solvers", ACM-Signum Newsletter, Vol.15, No.4, pp.10-11, 1980

63. Chase Jr., M. W., Davier, C. A., Davier, J. R., Eulrip, D. J., McDonald, R. A., and Syyerud, A. N., "JANAF Thermochemical Tables, 3rd Edition", Journal of Physical and Chemical Reference Data, 14, 1985

64. Uddi, M., Jiang, N., Frederickson, K., Stricker, J., Adamovich, I. V., and Lempert, W. R., "Spatially and Temporally Resolved Atomic Oxygen Measurements in Short Pulse Discharges by Two Photon Laser Induced Fluorescence", AIAA Paper 2007-1357, 45th AIAA Aerospace Sciences Meeting and Exhibit, Reno, NV, 2007

65. http://homepages.vub.ac.be/~akonnov/. Detailed Reaction Mechanism for Small Hydrocarbon Combustion

66. Konnov, A. A., "Development and Validation of a Detailed Reaction Mechanism for the Combustion of Small Hydrocarbons", 28th Symposium on Combustion, p.137, Edinburgh, 2000

APPENDIX A

Nitrogen second positive band synthetic spectra

These synthetic spectra, used for flow rotational temperature inference, were generated by using molecular constants of $N_2(C^3\Pi_u)$ and $N_2(B^3\Pi_g)$ excited electronic states listed in Table A.1.

	ω_e	$\omega_e x_e$	$\omega_e y_e$	$\omega_e z_e$	T_e	A_0	α
$N_2(C^3\Pi_u)$	2047.7928	28.9421	2.24537	-0.551196	89136.88	39.5	0.69
$N_2(B^3\Pi_g)$	1734.022	14.410	-0.0045	-0.00043	59619.3	42.256	0.045

	B_e	α_e	γ_e	D_e	β
$N_2(C^3\Pi_u)$	1.8268	0.024	0.0019	0.51e-5	0.22e-5
$N_2(B^3\Pi_g)$	1.63769	0.01786	-0.00014	0.588e-5	0.0013e-5

Table A.1 Spectroscopic constants of electronically excited N_2, in cm^{-1}.

The electronic-vibrational-rotational energy of a nitrogen molecule in an excited electronic state, on vibrational level v, and rotational level J can be calculated as follows,

$$E(v,J) = T_e + G_v + F_r. \tag{A.1}$$

Here T_e is the electronic energy (see Table A.1), G_v is the vibrational energy, and F_r is the rotational energy. The vibrational energy is expressed as follows [35],

$$G_v(v) = \omega_e(v+\frac{1}{2}) - \omega_e x_e(v+\frac{1}{2})^2 + \omega_e y_e(v+\frac{1}{2})^3 + \omega_e z_e(v+\frac{1}{2})^4, \tag{A.2}$$

where ω_e is the vibrational frequency, $\omega_e x_e$, $\omega_e y_e$, and $\omega_e z_e$ are anharmonicity parameters, and v is the vibrational quantum number.

The rotational energies of the three spin-splitting components of every rotational level J of the $^3\Pi$ electronic state are [35],

$$F_1(J) = B_v(J(J+1) - \sqrt{z} - 2z_a), \tag{A.3}$$

$$F_2(J) = B_v(J(J+1) + 4z_a), \tag{A.4}$$

$$F_3(J) = B_v(J(J+1) + \sqrt{z} - 2z_a), \tag{A.5}$$

where

$$B_v = B_e - \alpha_e(v+\frac{1}{2}) + \gamma_e(v+\frac{1}{2})^2 \tag{A.6}$$

is the rotational constant of a molecule on the vibrational level v,

$$z = \frac{A_v}{B_v}(\frac{A_v}{B_v} - 4) + \frac{4}{3} + 4J(J+1) - D_v(J(J+1)^2, \tag{A.7}$$

$$z_a = \frac{\left[\frac{A_v}{B_v}(\frac{A_v}{B_v} - 1) - \frac{4}{9} - 2J(J+1)\right]}{3z} - D_v(J(J+1)^2 \tag{A.8}$$

$$D_v = D_e + \beta(v+\frac{1}{2}), \tag{A.9}$$

and

$$A_v = A_0 - \alpha(v+\frac{1}{2}).., \tag{A.10}$$

In Eq. (A.10) A_v is the spin-orbit coupling parameter.

Based on the selection rule $\Delta\Sigma=0$, where Σ is the quantum number of the **S** component on the internuclear axis and **S** is the total spin angular momentum, there are three sub-bands for $N_2(C^3\Pi_u \rightarrow B^3\Pi_g)$ transitions, corresponding to electronic transitions between three rotational level components, each with a strong R, a strong P, and a weak

Q branch (see Fig. A. 1). For P branch, J′-J″=-1; for Q branch, J′-J″=0; and for R branch, J′-J″=1. Here, as usual, superscripts ′ and ″ refer to the upper and the lower electronic states $C^3\Pi_u$ and $B^3\Pi_g$, respectively. Transition energies are calculated as follows,

$$\Delta E = T_e' + G_v' + F_r' - T_e'' - G_v'' - F_r'' \quad . \tag{A.11}$$

For the band sequence used for the rotational temperature inference in the present work, v′-v″=-2.

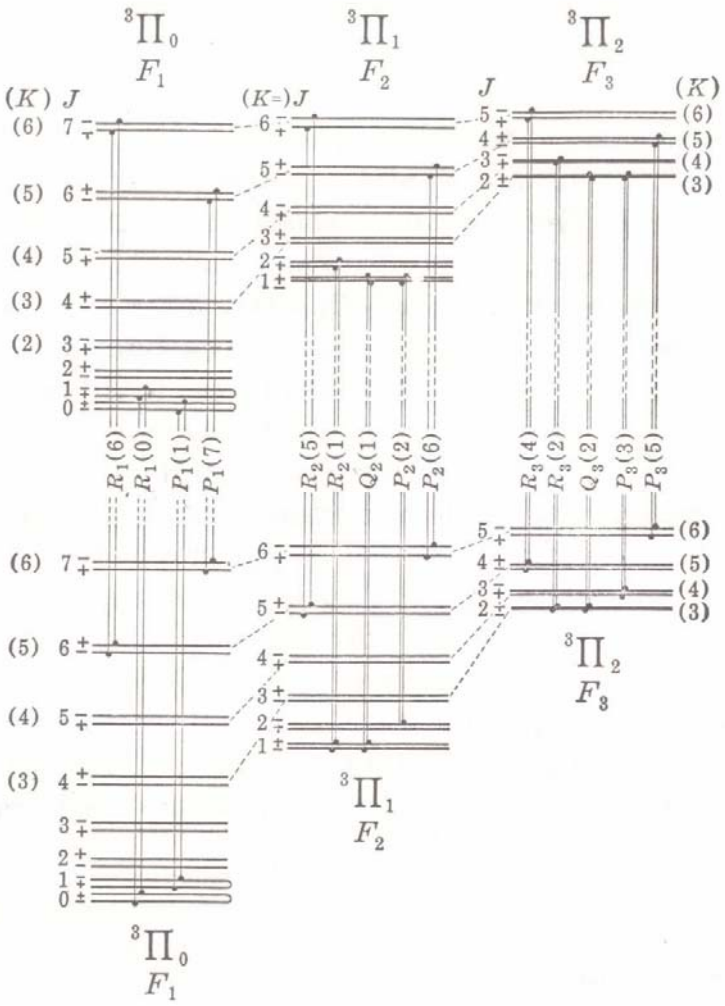

Figure A.1: Energy level diagram for $N_2(C^3\Pi_u \rightarrow B^3\Pi_g)$ transitions

Relative rotational line intensities for different branches are calculated based on Ref. [37]. For example, for a P branch transition, J′-J″=-1, the relative intensity can be expressed as

$$I = \frac{(J'+1)(J'+3)(2J'-1)}{(J'+2)(2J'+1)} \exp\left(-\frac{F_r'}{kT}\right) \cdot C_0 \cdot \left(\frac{hc}{T_e' + G_e' - T_e'' - G_e''}\right)^{-4} \quad \text{(A.12)}$$

where C_0 is a constant factor.

The synthetic spectrum modeling code adjusts the synthetic spectrum intensity to the experimental emission spectrum intensity by adjusting the vibrational population of the upper electronic state. The spectrometer slit function, which depends on the spectrometer entrance slit width, is needed to correctly reproduce vibrational-rotational line shapes generated by the code. The slit function is determined as a following curve fit to several atomic emission lineshapes of a Hg-Ar lamp,

$$I = I_{\max}\left[A_1 \exp\left(-\left(\frac{x-x_0}{\alpha}\right)^2\right) + A_2 \exp\left(-\left(\frac{x-x_0}{\beta}\right)^2\right) + A_3 \exp\left(-\frac{|x-x_0|}{\gamma}\right)\right], \quad \text{(A.13)}$$

where A_1, A_2, and A_3 are adjustable weight factors, $A_1+A_2+A_3=1$, and α, β, and γ are line shape parameters. Figure A.2 shows comparison of a typical experimental line shape and a curve fit slit function.

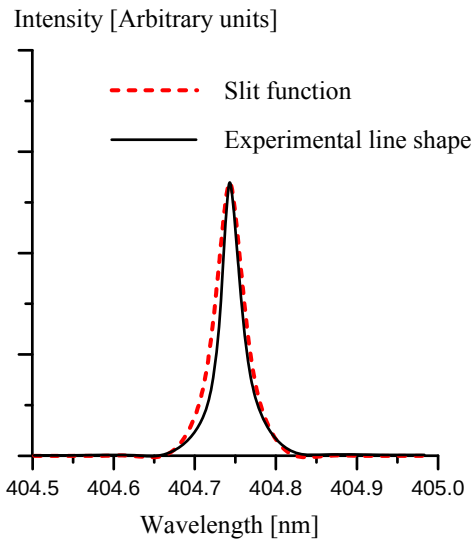

Figure A.2: Comparison of a typical experimental line shape and a curve fit slit function.

With all vibrational-rotational line positions, intensities, and line shapes calculated, the code adds them together and generates a synthetic spectrum, normalized on the experimental spectrum intensity. The only input parameter of the code which affects the shape of the synthetic spectrum is the rotational temperature, which is adjusted to minimize the least squares difference between the experimental and the synthetic spectra.

APPENDIX B

CH 4300 Å bands synthetic spectra

Synthetic spectra of CH ($A^2\Delta$, v′→$X^2\Pi$, v″) 4300 Å band system were generated by using molecular constants of CH($A^2\Delta$) and CH($X^2\Pi$) excited electronic states listed in Table B.1.

	ω_e	$\omega_e x_e$	$\omega_e y_e$	$\omega_e z_e$	T_e	A_0	α
CH($A^2\Delta$)	2930.7	96.65	0	0	23189.8	1.1	0
CH($X^2\Pi$)	2858.5	63.65	0	0	0	31.8	0

	B_e	α_e	γ_e	D_e	β
CH($A^2\Delta$)	14.919	0.697	0	0.00154	0
CH($X^2\Pi$)	14.456	0.534	0	0.00145	0

Table B.1 Spectroscopic constants of electronically excited CH, units in cm^{-1}.

The electronic-vibrational-rotational energy of a CH radical in an excited electronic state on vibrational level v and rotational level J can be calculated as follows,

$$E(v,J) = T_e + G_v + F_r. \tag{B.1}$$

Here T_e is the electronic energy (see Table B.1), G_v is the vibrational energy, and F_r is the rotational energy. The vibrational energy is expressed as follows [35]:

$$G_v(v) = \omega_e(v+\frac{1}{2}) - \omega_e x_e(v+\frac{1}{2})^2 + \omega_e y_e(v+\frac{1}{2})^3 + \omega_e z_e(v+\frac{1}{2})^4, \tag{B.2}$$

where ω_e is the vibrational frequency, $\omega_e x_e$, $\omega_e y_e$, and $\omega_e z_e$ are anharmonicity parameters, and v is the vibrational quantum number.

The rotational energies of the two spin-splitting components of every rotational level J of the $^2\Delta$ or $^2\Pi$ electronic state are [35],

$$F_a(J) = B_v((J+0.5)^2 - 0.5\sqrt{z} - 2z_a) - D_v((J+0.5)^2(((J+0.5)^2 - z_a), \quad \text{(B.3a)}$$

$$F_b(J) = B_v((J-0.5)^2 + 0.5\sqrt{z_b} - 2z_a) - D_v((J-0.5)^2(((J-0.5)^2 - z_a), \quad \text{(B.3b)}$$

where J=K+1/2, K is the total angular momentum quantum number without spin,

$$B_v = B_e - \alpha_e(v+\frac{1}{2}) + \gamma_e(v+\frac{1}{2})^2, \quad \text{(B.4)}$$

is the rotational constant on the vibrational level v,

$$z' = 4\frac{A'_v}{B'_v}(\frac{A'_v}{B'_v} - 4) + 4(J+0.5)^2, \quad \text{(B.5a)}$$

$$z'' = \frac{A''_v}{B''_v}(\frac{A''_v}{B''_v} - 4) + 4(J+0.5)^2, \quad \text{(B.5b)}$$

$$z_b' = 4\frac{A'_v}{B'_v}(\frac{A'_v}{B'_v} - 4) + 4(J-0.5)^2, \quad \text{(B.6a)}$$

$$z_b'' = \frac{A''_v}{B''_v}(\frac{A''_v}{B''_v} - 4) + 4(J-0.5)^2, \quad \text{(B.6b)}$$

$$z_a' = 4 \quad \text{(B.7a)}$$

$$z_a'' = 1 \quad \text{(B.7b)}$$

$$D_v = D_e + \beta(v+\frac{1}{2}), \quad \text{(B.8)}$$

and

$$A_v = A_0 - \alpha(v+\frac{1}{2}). \quad \text{(B.9)}$$

In Eq. (B.9), A_v is the spin-orbit coupling constant on the vibrational level v. Here, as usual, superscripts ′ and ″ refer to the upper and the lower electronic states, $A^2\Delta$ and $X^2\Pi$, respectively.

Based on the selection rule $\Delta\Sigma=0$, where Σ is the quantum number of the **S** component on the internuclear axis and **S** is the total spin angular momentum, there are two sub-bands for CH($A^2\Delta \rightarrow X^2\Pi$), corresponding to electronic transitions between two rotational level components, each one with R, P, and Q branches (see Fig. B.1). Transition energies are calculated as follows,

$$\Delta E = T_e' + G_v' + F_r' - T_e'' - G_v'' - F_r'' \ . \tag{B.10}$$

For the bands used for the rotational temperature inference in the present work, v′-v″=0.

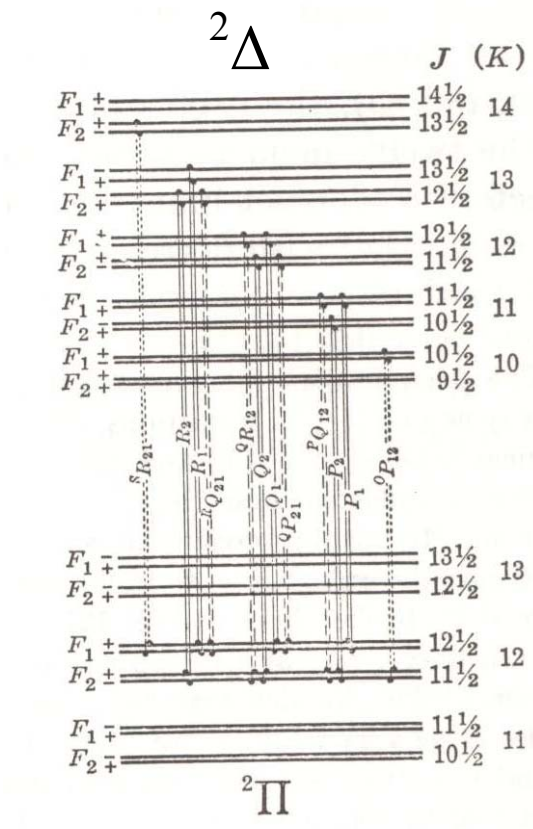

Figure B.1 Energy level diagram for CH ($A^2\Delta \rightarrow X^2\Pi$) transitions

Relative line intensities for different branches are calculated based on Ref. [37]. For example, for an R branch transition, J′-J″=1, the relative intensity can be expressed as

$$I = \Lambda \exp\left(-\frac{F_r'}{kT}\right) \cdot C_0 \cdot \left(\frac{hc}{T_e' + G_e' - T_e'' - G_e''}\right)^{-4}. \tag{B.11}$$

where C_0 is a constant factor, and

$$\Lambda_a = \frac{(J+3)(J+4)}{8(J+0.5)(J+1)(J-1)J(J-2)}((J-1)(J-2)+(J-2)(J+2))^2 \tag{B.12a}$$

$$\Lambda_b = \frac{(J+3)(J+4)}{8(J+0.5)(J+1)(J+3)J(J+2)}((J+3)(J+2)+(J-2)(J+2))^2 \tag{B.12b}$$

The spectrometer slit function is also needed for reproducing vibrational-rotational line shapes, as described in Appendix A. With all vibrational-rotational line positions, intensities, and line shapes calculated, the rotational temperature can be inferred from the code by adjusting the temperature to minimize the least squares difference between the experimental and synthetic spectra.

APPENDIX C

GRI-Mech 3.0 Reaction List*

Reaction	Rate coefficient (cm^3/s or cm^6/s)	n	Ea (cal/mole)
O + O + M = O2 + M	3.31E-31	-1	0
O + H + M = OH + M	1.38E-30	-1	0
O + H2 = H + OH	6.43E-20	2.7	6260
O + HO2 = OH + O2	3.32E-11	0	0
O + H2O2 = OH + HO2	1.60E-17	2	4000
O + CH = H + CO	9.46E-11	0	0
O + CH2 = H + HCO	1.33E-10	0	0
O + CH2(S) = H2 + CO	2.49E-11	0	0
O + CH2(S) = H + HCO	2.49E-11	0	0
O + CH3 = H + CH2O	8.40E-11	0	0
O + CH4 = OH + CH3	1.69E-15	1.5	8600
O + CO = CO2	2.99E-14	0	2385
O + CO + (M) = CO2 + (M)	1.66E-33	0	3000
O + HCO = OH + CO	4.98E-11	0	0
O + HCO = H + CO2	4.98E-11	0	0
O + CH2O = OH + HCO	6.48E-11	0	3540
O + CH2OH = OH + CH2O	1.66E-11	0	0
O + CH3O = OH + CH2O	1.66E-11	0	0
O + CH3OH = OH + CH2OH	6.44E-19	2.5	3100
O + CH3OH = OH + CH3O	2.16E-19	2.5	5000
O + C2H = CH + CO	8.30E-11	0	0

* For reactions containing a symbol (M), two line entries give rate coefficients in the low-pressure limit (k_0) and the high-pressure limit (k_∞), respectively.

O + C2H2 = H + HCCO	2.24E-17	2	1900
O + C2H2 = OH + C2H	7.64E-05	-1.41	28950
O + C2H2 = CO + CH2	1.15E-17	2	1900
O + C2H3 = H + CH2CO	4.98E-11	0	0
O + C2H4 = CH3 + HCO	2.08E-17	1.83	220
O + C2H5 = CH3 + CH2O	3.72E-11	0	0
O + C2H6 = OH + C2H5	1.49E-16	1.92	5690
O + HCCO = H + CO + CO	1.66E-10	0	0
O + CH2CO = OH + HCCO	1.66E-11	0	8000
O + CH2CO = CH2 + CO2	2.91E-12	0	1350
O2 + CO = O + CO2	4.15E-12	0	47800
O2 + CH2O = HO2 + HCO	1.66E-10	0	40000
H + O2 + M = HO2 + M	7.72E-30	-0.86	0
H + O2 + O2 = HO2 + O2	5.73E-29	-1.24	0
H + O2 + H2O = HO2 + H2O	3.11E-29	-0.76	0
H + O2 + N2 = HO2 + N2	7.17E-29	-1.24	0
H + O2 + AR = HO2 + AR	1.93E-30	-0.8	0
H + O2 = O + OH	4.40E-08	-0.67	17041
H + H + M = H2 + M	2.76E-30	-1	0
H + H + H2 = H2 + H2	2.48E-31	-0.6	0
H + H + H2O = H2 + H2O	1.65E-28	-1.25	0
H + H + CO2 = H2 + CO2	1.52E-27	-2	0
H + OH + M = H2O + M	6.06E-26	-2	0
H + HO2 = O + H2O	6.59E-12	0	671
H + HO2 = O2 + H2	7.44E-11	0	1068
H + HO2 = OH + OH	1.39E-10	0	635
H + H2O2 = HO2 + H2	2.01E-17	2	5200
H + H2O2 = OH + H2O	1.66E-11	0	3600
H + CH = C + H2	2.74E-10	0	0
H + CH2 = CH3	9.96E-10	0	0
H + CH2 + (M) = CH3 + (M)	2.87E-22	-2.76	1600
H + CH2(S) = CH + H2	4.98E-11	0	0
H + CH3 = CH4	2.31E-08	-0.53	536

H + CH3 + (M) = CH4 + (M)	7.22E-15	-4.76	2440
H + CH4 = CH3 + H2	1.10E-15	1.62	10840
H + HCO = CH2O	1.81E-12	0.48	-260
H + HCO + (M) = CH2O + (M)	6.81E-24	-2.57	425
H + HCO = H2 + CO	1.22E-10	0	0
H + CH2O = CH2OH	8.97E-13	0.45	3600
H + CH2O + (M) = CH2OH + (M)	3.50E-16	-4.82	6530
H + CH2O = CH3O	8.97E-13	0.45	2600
H + CH2O + (M) = CH3O + (M)	6.06E-18	-4.8	5560
H + CH2O = HCO + H2	9.53E-17	1.9	2742
H + CH2OH = CH3OH	1.75E-12	0.50	86
H + CH2OH + (M) = CH3OH + (M)	1.20E-16	-4.65	5080
H + CH2OH = H2 + CH2O	3.32E-11	0	0
H + CH2OH = OH + CH3	2.74E-13	0.65	-284
H + CH2OH = CH2(S) + H2O	5.45E-11	-0.09	610
H + CH3O = CH3OH	4.03E-12	0.51	50
H + CH3O + (M) = CH3OH + (M)	1.28E-06	-7.44	14080
H + CH3O = H + CH2OH	6.89E-17	1.63	1924
H + CH3O = H2 + CH2O	3.32E-11	0	0
H + CH3O = OH + CH3	2.49E-12	0.5	-110
H + CH3O = CH2(S) + H2O	4.35E-10	-0.23	1070
H + CH3OH = CH2OH + H2	2.82E-17	2.1	4870
H + CH3OH = CH3O + H2	6.97E-18	2.1	4870
H + C2H = C2H2	1.66E-07	-1.0	0
H + C2H + (M) = C2H2 + (M)	1.03E-14	-4.8	1900
H + C2H2 = C2H3	9.30E-12	0	2400
H + C2H2 + (M) = C2H3 + (M)	1.05E-07	-7.27	7220
H + C2H3 = C2H4	1.01E-11	0.27	280
H + C2H3 + (M) = C2H4 + (M)	3.86E-18	-3.86	3320
H + C2H3 = H2 + C2H2	4.98E-11	0	0
H + C2H4 = C2H5	8.93E-13	0.45	1820
H + C2H4 + (M) = C2H5 + (M)	1.65E-06	-7.62	6970
H + C2H4 = C2H3 + H2	2.21E-18	2.53	12240

H + C2H5 = C2H6	8.65E-07	-0.99	1580
H + C2H5 + (M) = C2H6 + (M)	5.49E-07	-7.08	6685
H + C2H5 = H2 + C2H4	3.32E-12	0	0
H + C2H6 = C2H5 + H2	1.91E-16	1.9	7530
H + HCCO = CH2(S) + CO	1.66E-10	0	0
H + CH2CO = HCCO + H2	8.30E-11	0	8000
H + CH2CO = CH3 + CO	1.88E-11	0	3428
H + HCCOH = H + CH2CO	1.66E-11	0	0
H2 + CO = CH2O	7.14E-17	1.50	79600
H2 + CO + (M) = CH2O + (M)	1.40E-20	-3.42	84350
OH + H2 = H + H2O	3.59E-16	1.51	3430
OH + OH = H2O2	1.23E-10	-0.37	0
OH + OH + (M) = H2O2 + (M)	6.34E-30	-0.9	-1700
OH + OH = O + H2O	5.93E-20	2.4	-2110
OH + HO2 = O2 + H2O	2.41E-11	0	-500
OH + H2O2 = HO2 + H2O	3.32E-12	0	427
OH + C = H + CO	8.30E-11	0	0
OH + CH = H + HCO	4.98E-11	0	0
OH + CH2 = H + CH2O	3.32E-11	0	0
OH + CH2 = CH + H2O	1.88E-17	2	3000
OH + CH2(S) = H + CH2O	4.98E-11	0	0
OH + CH3 = CH3OH	4.63E-06	-1.43	1330
OH + CH3 + (M) = CH3OH + (M)	1.10E-11	-5.92	3140
OH + CH3 = CH2 + H2O	9.30E-17	1.6	5420
OH + CH3 = CH2(S) + H2O	1.07E-06	-1.34	1417
OH + CH4 = CH3 + H2O	1.66E-16	1.6	3120
OH + CO = H + CO2	7.90E-17	1.23	70
OH + HCO = H2O + CO	8.30E-11	0	0
OH + CH2O = HCO + H2O	5.69E-15	1.18	-447
OH + CH2OH = H2O + CH2O	8.30E-12	0	0
OH + CH3O = H2O + CH2O	8.30E-12	0	0
OH + CH3OH = CH2OH + H2O	2.39E-18	2	-840
OH + CH3OH = CH3O + H2O	1.05E-17	2	1500

OH + C2H = H + HCCO	3.32E-11	0	0
OH + C2H2 = H + CH2CO	3.62E-28	4.5	-1000
OH + C2H2 = H + HCCOH	8.37E-19	2.3	13500
OH + C2H2 = C2H + H2O	5.60E-17	2	14000
OH + C2H2 = CH3 + CO	8.02E-28	4	-2000
OH + C2H3 = H2O + C2H2	8.30E-12	0	0
OH + C2H4 = C2H3 + H2O	5.98E-18	2	2500
OH + C2H6 = C2H5 + H2O	5.88E-18	2.12	870
OH + CH2CO = HCCO + H2O	1.25E-11	0	2000
HO2 + HO2 = O2 + H2O2	2.16E-13	0	-1630
HO2 + CH2 = OH + CH2O	3.32E-11	0	0
HO2 + CH3 = O2 + CH4	1.66E-12	0	0
HO2 + CH3 = OH + CH3O	6.28E-11	0	0
HO2 + CO = OH + CO2	2.49E-10	0	23600
HO2 + CH2O = HCO + H2O2	9.30E-18	2	12000
C + O2 = O + CO	9.63E-11	0	576
C + CH2 = H + C2H	8.30E-11	0	0
C + CH3 = H + C2H2	8.30E-11	0	0
CH + O2 = O + HCO	1.11E-10	0	0
CH + H2 = H + CH2	1.79E-10	0	3110
CH + H2O = H + CH2O	9.48E-12	0	-755
CH + CH2 = H + C2H2	6.64E-11	0	0
CH + CH3 = H + C2H3	4.98E-11	0	0
CH + CH4 = H + C2H4	9.96E-11	0	0
CH + CO2 = HCO + CO	3.15E-10	0	15792
CH + CO = HCCO	8.e0E-10	0	0
CH + CO + (M) = HCCO + (M)	7.42E-20	-3.74	1936
CH + CH2O = H + CH2CO	1.57E-10	0	-515
CH + HCCO = CO + C2H2	8.30E-11	0	0
CH2 + O2 = OH + H + CO	8.30E-12	0	1500
CH2 + H2 = H + CH3	8.30E-19	2	7230
CH2 + CH2 = H2 + C2H2	2.66E-09	0	11944
CH2 + CH3 = H + C2H4	6.64E-11	0	0

CH2 + CH4 = CH3 + CH3	4.08E-18	2	8270
CH2 + CO = CH2CO	1.34E-12	0.5	4510
CH2 + CO + (M) = CH2CO + (M)	7.42E-15	-5.11	7095
CH2 + HCCO = C2H3 + CO	4.98E-11	0	0
CH2(S) + N2 = CH2 + N2	2.49E-11	0	600
CH2(S) + AR = CH2 + AR	1.49E-11	0	600
CH2(S) + O2 = H + OH + CO	4.65E-11	0	0
CH2(S) + O2 = CO + H2O	1.99E-11	0	0
CH2(S) + H2 = CH3 + H	1.16E-10	0	0
CH2(S) + H2O = CH3OH	8.00E-07	-1.16	1145
CH2(S) + H2O + (M) = CH3OH + (M)	5.18E-10	-6.36	5040
CH2(S) + H2O = CH2 + H2O	4.98E-11	0	0
CH2(S) + CH3 = H + C2H4	1.99E-11	0	-570
CH2(S) + CH4 = CH3 + CH3	2.66E-11	0	-570
CH2(S) + CO = CH2 + CO	1.49E-11	0	0
CH2(S) + CO2 = CH2 + CO2	1.16E-11	0	0
CH2(S) + CO2 = CO + CH2O	2.32E-11	0	0
CH2(S) + C2H6 = CH3 + C2H5	6.64E-11	0	-550
CH3 + O2 = O + CH3O	5.91E-11	0	30480
CH3 + O2 = OH + CH2O	3.84E-12	0	20315
CH3 + H2O2 = HO2 + CH4	4.07E-20	2.47	5180
CH3 + CH3 = C2H6	1.12E-07	-1.18	654
CH3 + CH3 + (M) = C2H6 + (M)	9.37E-07	-7.03	2762
CH3 + CH3 = H + C2H5	1.14E-11	0.1	10600
CH3 + HCO = CH4 + CO	4.40E-11	0	0
CH3 + CH2O = HCO + CH4	5.51E-21	2.81	5860
CH3 + CH3OH = CH2OH + CH4	4.98E-17	1.5	9940
CH3 + CH3OH = CH3O + CH4	1.66E-17	1.5	9940
CH3 + C2H4 = C2H3 + CH4	3.77E-19	2	9200
CH3 + C2H6 = C2H5 + CH4	1.02E-17	1.74	10450
HCO + H2O = H + CO + H2O	2.49E-06	-1	17000
HCO + M = H + CO + M	3.10E-07	-1	17000
HCO + O2 = HO2 + CO	2.24E-11	0	400

CH2OH + O2 = HO2 + CH2O	2.99E-11	0	900
CH3O + O2 = HO2 + CH2O	7.11E-37	7.6	-3530
C2H + O2 = HCO + CO	1.66E-11	0	-755
C2H + H2 = H + C2H2	9.43E-14	0.9	1993
C2H3 + O2 = HCO + CH2O	7.60E-08	-1.39	1015
C2H4 = H2 + C2H2	8.00E+12	0.44	86770
C2H4 + (M) = H2 + C2H2 + (M)	2.62E+27	-9.3	97800
C2H5 + O2 = HO2 + C2H4	1.39E-12	0	3875
HCCO + O2 = OH + CO + CO	5.31E-12	0	854
HCCO + HCCO = CO + CO + C2H2	1.66E-11	0	0
N + NO = N2 + O	4.48E-11	0	355
N + O2 = NO + O	1.49E-14	1	6500
N + OH = NO + H	5.58E-11	0	385
N2O + O = N2 + O2	2.32E-12	0	10810
N2O + O = NO + NO	4.81E-11	0	23150
N2O + H = N2 + OH	6.43E-10	0	18880
N2O + OH = N2 + HO2	3.32E-12	0	21060
N2O = N2 + O	7.91E+12	0	56020
N2O + (M) = N2 + O + (M)	1.06E-09	0	56640
HO2 + NO = NO2 + OH	3.50E-12	0	-480
NO + O + M = NO2 + M	2.92E-28	-1.41	0
NO2 + O = NO + O2	6.48E-12	0	-240
NO2 + H = NO + OH	2.19E-10	0	360
NH + O = NO + H	6.64E-11	0	0
NH + H = N + H2	5.31E-11	0	330
NH + OH = HNO + H	3.32E-11	0	0
NH + OH = N + H2O	3.32E-15	1.2	0
NH + O2 = HNO + O	7.65E-19	2	6500
NH + O2 = NO + OH	2.13E-18	1.5	100
NH + N = N2 + H	2.49E-11	0	0
NH + H2O = HNO + H2	3.32E-11	0	13850
NH + NO = N2 + OH	3.59E-11	-0.23	0
NH + NO = N2O + H	6.06E-10	-0.45	0

NH2 + O = OH + NH	4.98E-12	0	0
NH2 + O = H + HNO	6.48E-11	0	0
NH2 + H = NH + H2	6.64E-11	0	3650
NH2 + OH = NH + H2O	1.49E-16	1.5	-460
NNH = N2 + H	3.30E+08	0	0
NNH + M = N2 + H + M	2.16E-10	-0.11	4980
NNH + O2 = HO2 + N2	8.30E-12	0	0
NNH + O = OH + N2	4.15E-11	0	0
NNH + O = NH + NO	1.16E-10	0	0
NNH + H = H2 + N2	8.30E-11	0	0
NNH + OH = H2O + N2	3.32E-11	0	0
NNH + CH3 = CH4 + N2	4.15E-11	0	0
H + NO + M = HNO + M	1.23E-28	-1.32	740
HNO + O = NO + OH	4.15E-11	0	0
HNO + H = H2 + NO	1.49E-12	0.72	660
HNO + OH = NO + H2O	2.16E-17	1.9	-950
HNO + O2 = HO2 + NO	1.66E-11	0	13000
CN + O = CO + N	1.28E-10	0	0
CN + OH = NCO + H	6.64E-11	0	0
CN + H2O = HCN + OH	1.33E-11	0	7460
CN + O2 = NCO + O	1.02E-11	0	-440
CN + H2 = HCN + H	4.90E-19	2.45	2240
NCO + O = NO + CO	3.90E-11	0	0
NCO + H = NH + CO	8.97E-11	0	0
NCO + OH = NO + H + CO	4.15E-12	0	0
NCO + N = N2 + CO	3.32E-11	0	0
NCO + O2 = NO + CO2	3.32E-12	0	20000
NCO + M = N + CO + M	5.15E-10	0	54050
NCO + NO = N2O + CO	3.15E-07	-1.52	740
NCO + NO = N2 + CO2	6.31E-06	-2	800
HCN + M = H + CN + M	1.73E+05	-3.3	126600
HCN + O = NCO + H	3.37E-20	2.64	4980
HCN + O = NH + CO	8.42E-21	2.64	4980

HCN + O = CN + OH	6.49E-15	1.58	26600
HCN + OH = HOCN + H	1.83E-18	2.03	13370
HCN + OH = HNCO + H	7.31E-21	2.26	6400
HCN + OH = NH2 + CO	2.66E-22	2.56	9000
H + HCN = H2CN	5.48E-11	0	0
H + HCN + (M) = H2CN + (M)	3.86E-22	-3.4	1900
H2CN + N = N2 + CH2	9.96E-11	0	400
C + N2 = CN + N	1.05E-10	0	46020
CH + N2 = HCN + N	5.18E-15	0.88	20130
CH + N2 = HCNN	5.15E-12	0.15	0
CH + N2 + (M) = HCNN + (M)	3.58E-23	-3.16	740
CH2 + N2 = HCN + NH	1.66E-11	0	74000
CH2(S) + N2 = NH + HCN	1.66E-13	0	65000
C + NO = CN + O	3.15E-11	0	0
C + NO = CO + N	4.81E-11	0	0
CH + NO = HCN + O	6.81E-11	0	0
CH + NO = H + NCO	2.69E-11	0	0
CH + NO = N + HCO	4.08E-11	0	0
CH2 + NO = H + HNCO	5.15E-07	-1.38	1270
CH2 + NO = OH + HCN	4.81E-10	-0.69	760
CH2 + NO = H + HCNO	6.31E-11	-0.36	580
CH2(S) + NO = H + HNCO	5.15E-07	-1.38	1270
CH2(S) + NO = OH + HCN	4.81E-10	-0.69	760
CH2(S) + NO = H + HCNO	6.31E-11	-0.36	580
CH3 + NO = HCN + H2O	1.59E-10	0	28800
CH3 + NO = H2CN + OH	1.66E-12	0	21750
HCNN + O = CO + H + N2	3.65E-11	0	0
HCNN + O = HCN + NO	3.32E-12	0	0
HCNN + O2 = O + HCO + N2	1.99E-11	0	0
HCNN + OH = H + HCO + N2	1.99E-11	0	0
HCNN + H = CH2 + N2	1.66E-10	0	0
HNCO + O = NH + CO2	1.63E-16	1.41	8500
HNCO + O = HNO + CO	2.49E-16	1.57	44000

HNCO + O = NCO + OH	3.65E-18	2.11	11400
HNCO + H = NH2 + CO	3.74E-17	1.7	3800
HNCO + H = H2 + NCO	1.74E-19	2.5	13300
HNCO + OH = NCO + H2O	5.48E-17	1.5	3600
HNCO + OH = NH2 + CO2	5.48E-18	1.5	3600
HNCO + M = NH + CO + M	1.96E-08	0	84720
HCNO + H = H + HNCO	3.49E-09	-0.69	2850
HCNO + H = OH + HCN	4.48E-13	0.18	2120
HCNO + H = NH2 + CO	2.82E-10	-0.75	2890
HOCN + H = H + HNCO	3.32E-17	2	2000
HCCO + NO = HCNO + CO	1.49E-11	0	0
CH3 + N = H2CN + H	1.01E-09	-0.31	290
CH3 + N = HCN + H2	6.14E-12	0.15	-90
NH3 + H = NH2 + H2	8.97E-19	2.4	9915
NH3 + OH = NH2 + H2O	8.30E-17	1.6	955
NH3 + O = NH2 + OH	1.56E-17	1.94	6460
NH + CO2 = HNO + CO	1.66E-11	0	14350
CN + NO2 = NCO + NO	1.02E-08	-0.75	345
NCO + NO2 = N2O + CO2	5.40E-12	0	-705
N + CO2 = NO + CO	4.98E-12	0	11300
O + CH3 = H + H2 + CO	5.60E-11	0	0
O + C2H4 = H + CH2CHO	1.11E-17	1.83	220
O + C2H5 = H + CH3CHO	1.83E-10	0	0
OH + CH3 = H2 + CH2O	1.33E-14	0.5	-1755
CH + H2 = CH3	3.27E-12	0.43	-370
CH + H2 + (M) = CH3 + (M)	1.33E-22	-2.8	590
CH2 + O2 = H + H + CO2	9.63E-12	0	1500
CH2 + O2 = O + CH2O	3.98E-12	0	1500
CH2 + CH2 = H + H + C2H2	3.32E-10	0	10989
CH2(S) + H2O = H2 + CH2O	1.13E-13	0.25	-935
C2H3 + O2 = O + CH2CHO	5.03E-13	0.29	11
C2H3 + O2 = HO2 + C2H2	2.22E-18	1.61	-384
O + CH3CHO = OH + CH2CHO	4.85E-12	0	1808

O + CH3CHO = OH + CH3 + CO	4.85E-12	0	1808
O2 + CH3CHO = HO2 + CH3 + CO	5.00E-11	0	39150
H + CH3CHO = CH2CHO + H2	3.40E-15	1.16	2405
H + CH3CHO = CH3 + H2 + CO	3.40E-15	1.16	2405
OH + CH3CHO = CH3 + H2O + CO	3.89E-14	0.73	-1113
HO2 + CH3CHO = CH3 + H2O2 + CO	5.00E-12	0	11923
CH3 + CH3CHO = CH3 + CH4 + CO	4.52E-18	1.77	5920
H + CH2CO = CH2CHO	8.08E-13	0.42	-1755
H + CH2CO + (M) = CH2CHO + (M)	2.79E-06	-7.63	3854
O + CH2CHO = H + CH2 + CO2	2.49E-10	0	0
O2 + CH2CHO = OH + CO + CH2O	3.01E-14	0	0
O2 + CH2CHO = OH + HCO + HCO	3.90E-14	0	0
H + CH2CHO = CH3 + HCO	3.65E-11	0	0
H + CH2CHO = CH2CO + H2	1.83E-11	0	0
OH + CH2CHO = H2O + CH2CO	1.99E-11	0	0
OH + CH2CHO = HCO + CH2OH	5.00E-11	0	0
CH3 + C2H5 = C3H8	1.57E-11	0	0
CH3 + C2H5 + (M) = C3H8 + (M)	7.47E+26	-16.8	13065
O + C3H8 = OH + C3H7	3.20E-19	2.68	3716
H + C3H8 = C3H7 + H2	2.19E-18	2.54	6756
OH + C3H8 = C3H7 + H2O	5.25E-17	1.8	934
C3H7 + H2O2 = HO2 + C3H8	6.28E-22	2.72	1500
CH3 + C3H8 = C3H7 + CH4	1.50E-24	3.65	7154
CH3 + C2H4 = C3H7	4.23E-18	1.6	5700
CH3 + C2H4 + (M) = C3H7 + (M)	8.27E+15	-14.6	18170
O + C3H7 = C2H5 + CH2O	1.60E-10	0	0
H + C3H7 = C3H8	6.00E-11	0	0
H + C3H7 + (M) = C3H8 + (M)	1.22E+14	-13.5	11357
H + C3H7 = CH3 + C2H5	6.74E-18	2.19	890
OH + C3H7 = C2H5 + CH2OH	4.00E-11	0	0
HO2 + C3H7 = O2 + C3H8	4.23E-14	0.26	-943
HO2 + C3H7 = OH + C2H5 + CH2O	4.00E-11	0	0
CH3 + C3H7 = C2H5 + C2H5	3.20E-11	-0.32	0